Elaboration of Spatial Current and Temperature Variations in Microtubular Solid Oxide Fuel Cells by Experimental and Numerical Techniques

a dissertation presented

by

Özgür AYDIN

in fulfillment for the degree of

Doctor of Engineering

in

Hydrogen Energy Systems

九州大学
KYUSHU UNIVERSITY

Fukuoka, JAPAN

January, 2017

Abstract

Stemming mainly from the concentration variations of the reactants and products along the respective flow channels, the longitudinal current variations are crucial in SOFCs (solid oxide fuel cells), as they result in the performance and structure degradations (e.g. RedOx cycling). Being related to the current variations, the longitudinal temperature variations are important, because they give rise to the thermal stresses. It is hence required to identify the longitudinal variations in the characteristic properties, for which in-situ spatial characterization techniques are available (e.g. segmentation, etc.). However, it is impractical to apply the existing techniques on various forms of SOFC. Although numerical tools are feasible, they are required to be verified with experimental data. For improving the reliability of the numerical SOFC tools, in this Ph.D. study, the longitudinal current and temperature variations are elaborated via applying the segmentation method along with a finite element model on mt-SOFCs (microtubular-SOFCs) utilizing hydrogen and syngas (a mixture of hydrocarbons).

In-situ measured current variations along mt-SOFCs are presented under various fuel (hydrogen) flow conditions; a remarkable performance degradation is disclosed. Additionally, a high risk of RedOx cycling is diagnosed at low fuel flow conditions. Substantial temperature variations along mt-SOFCs in both co- and counter-flow configurations are identified. Based on longitudinal impedance measurements, a strong impact of the large temperature gradients on both electrolyte conductivity and reaction kinetics is shown, influencing the longitudinal current and concentration variations. It is found that longitudinal current (concentration) and temperature variations couple in the counter-flow configuration, exhibiting larger variations in comparison with the co-flow configuration. Analysis of the longitudinal temperature and current variations together under various operation conditions discloses the contributions by current variations, and convective heat transfer between air and the cathode surface to the longitudinal temperature variations. It is shown that the large temperature variations stem mainly from the excess air supplied as a common practice to sweep the waste heat produced in SOFCs. In this regard, the excess air supply should be avoided to minimize temperature variations in the co-flow configuration, which would also reduce the power consumption by the air blower.

For evaluating reliability of numerical tools developed to compute spatial variations, a fully-coupled two dimensional finite element model is presented for a mt-SOFC. The model is validated by correlating the conventional current/voltage curve of the cell to the in-situ measured one. This conventional validation process exhibits remarkable deviations among numerical and experimental values (current and temperature). Exclusion of radiant heat transfer makes the deviation among the experimental and numerical temperature values significantly larger, revealing the notable impact of the radiant heat transfer on the longitudinal temperature variations. Due to the poor accuracy of temperature computation and substantial impact of temperature on the other processes in such a fully-coupled model, the model is modified to capture the in-situ measured temperature variations. This validation shows a positive impact on estimation of the longitudinal current variations, i.e., on reliability of numerical model.

Spatial variations in characteristic properties of SOFCs are anticipated to be more remarkable while direct internal reforming of hydrocarbons. Spatial characterization is hence more demanded in direct internal reforming SOFCs. For improving reliability of numerical tools developed for direct internal reforming SOFCs, the impact of the endothermic internal reforming on the longitudinal temperature variations and corresponding rate of the reforming reaction is analyzed while utilizing syngas. It is found that the extent of endothermic cooling changes along the cell, which is attributed to the changing reaction rate related to the concentration variations. It is found that syngas utilization yields remarkable current fluctuations in parallel to the rate of the internal reforming. The fluctuations are ascribed to the competition among the reforming reaction and the hydrogen oxidation reaction, as they both proceed on the same catalysts.

It is concluded that the heat and mass transfer processes should be carefully considered in numerical tools for precisely computing spatial variations. Besides, the rate of the reforming reaction should be accurately defined to employ numerical tools for internal reforming SOFCs.

Acknowledgments

I have conducted this study in Fuel Cell Systems Laboratory of Kyushu University under supervision of Assoc. Prof. Dr. Tatsumi KITAHARA and Assist. Prof. Dr. Hironori NAKAJIMA. I would like to thank my supervisors for providing me this Ph.D. position, and supplying me with precious recommendations throughout my study. I am in particular grateful for their invaluable encouragement to attend major conferences in the research field, and to exploit all opportunities available around. I will be particularly indebted to Prof. NAKAJIMA for instructing me principles of the scientific publication.

I would like to also thank the members of the evaluation committee Prof. Dr. Kohei ITO and Prof. Dr. Koji TAKASAKI for assessing my study and providing useful suggestions. I consider it an honor to work with Prof. Dr. ITO throughout this study. His extremely kind efforts to explain technical and social things going around are priceless; I will be always grateful for them.

I would like to thank all my colleagues who have already graduated and who are still studying in the laboratory for keeping me highly motivated with their endless helpful and friendly approaches, which allow me to state that the atmosphere in this laboratory has been indisputably the best in my experience where a foreigner does not notice whether s/he is living in abroad. I feel obliged to express my gratitude for technical and social support granted by my friend Takahiro KOSHIYAMA. I feel also obliged to acknowledge Mrs. Junko KIMURA and Ms. Akiko INADA for their continuous support in dealing with my social matters. Without them, I would not be able to manage a smooth life in Japan.

I am honored to acknowledge the successive financial supports by International Research Center for Hydrogen Energy at Kyushu University and Super Global Scholarship by MEXT-Japan throughout my study. I appreciate very much their supports as they released me from my financial worries, and let me to focus on my research intensively.

Although most people think that the price of studying in abroad is to miss all the moments spent apart from family, for me not being able to fulfill my responsibilities toward my family has been the highest price. Being aware of this fact, I would like to thank to all my family members for their patience and understanding.

Table of Contents

List of Tables

List of Figures

Nomenclature

A	Surface area (m^2)	J	Molar mass flux ($mol/m^2\ s$)
A_0	Pre-exponential factor	k	Thermal conductivity ($W/m^2\ K$)
c	Molar concentration (mol/m^3)	K	Pre-exponential factor
C	Capacity (F)	L	Length (m)
C_p	Specific heat ($J/kg\ K$)	M	Molar mass (kg)
D	Diffusivity (m^2/s)	n	Number of electrons
D_h	Hydraulic diameter (m)	p	Pressure (Pa)
e^-	Electron	$\dot{q}$	Heat flux (W/m^2)
E	Energy (J)	Q	Electrical charge (C)
E_0	Activation energy (J/mol)	re	Real part of impedance
f	Frequency ($1/s$)	R	Electrical resistance (Ω)
f_1	Decay rate of reactants to products	S	Entropy (J/mol)
F	Force (N)	t	Time (s)
G	Gibbs free energy (J/mol)	T	Temperature (K)
h	Heat transfer coefficient ($W/m^2\ K$)	u	Velocity (m/s)
H	Enthalpy (J/mol)	U	Electrical voltage (V)
i	Current density (A/m^2)	U_0	Electrical voltage amplitude (V)
i_0	Exchange current density (A/m^2)	v	Stoichiometric coefficient
i_v	Volumetric current density (A/m^3)	V	Volume (m^3)
I	Electrical current (A)	w	Mass fraction
I_0	Electrical current amplitude (A)	W	Electrical work (J)
img	Imaginary part of impedance	x	Molar fraction
j	Imaginary unit	X	Source term

y	Unit vector
Z	Impedance (Ω)

Greek Letters

α	Absorptivity
α_v	Thermal expansion coefficient ($1/K$)
β	Symmetry factor
γ	Reaction coefficient
δ	Thickness (m)
ϵ	Emissivity
ε	Porosity
ζ	Specific surface area (m^2/m^3)
η	Overpotential (V)
κ	Permeability (m^2)
λ	Stoichiometry
Λ	Specific atom diffusion volume (m^3/mol)
μ	Viscosity ($Pa\ s$)
ν	Chemical reaction rate (mol/s)
ρ	Density (kg/m^3)
σ	Electronic/ionic conductivity (S/m)
τ	Tortuosity
$\dot{v}$	Volumetric flow rate (m^3/s)
Υ	Diffusion driving force
Υ	Diffusion mass flux vector
ϕ	Potential (V)
Φ	Electrical phase ($^\circ$)
ψ	Froscheimer drag
ω	Angular frequency (ω)
ξ	Electrical efficiency

Subscripts

a	Anode
A	Atmospheric
abs	Absorbed
AC	Alternating current
act	Activation
c	Cathode
cap	Capacity
$cell$	Cell
$conc$	Concentration
$cond$	Conductive
$conv$	Convective
dl	Double layer
e	Electrode
ec	Electrical contact
eff	Effective
el	Electrolyte
$emit$	Emitted
eq	Equilibrium
f	Fluid mixture
fur	Furnace
h	Hydraulic

$heat$	Heat
HOR	Hydrogen oxidation reaction
i	Species
img	Imaginary
in	Inlet
inc	incident
$irev$	irreversible
$leak$	Leakage
loc	Local
m	Electrodes and electrolyte
MSR	Methane steam reforming
ohm	Ohmic
out	Outlet
OCV	Open circuit voltage
P	Product
R	Reactant
rad	Radiative
re	Real
ref	Reference
rev	Reversible
s	Surface
seg	Segment
tot	Total

Superscripts

$*$	Triple phase boundary
0	Standard
b	Bulk
$diff$	Diffusion
in	Inlet
T	Thermal

Constants

F	Faraday constant
I	Identity matrix
k_B	Boltzman constant
R	Ideal gas constant
σ_{SB}	Stefan-Boltzman constant

Units

C	Coulomb
F	Farad
r	Radian
S	Siemens

Abbreviations

AC	Alternating Current
CSR	Catalytic Steam Reformer
CTE	Coefficient of Thermal Expansion
DC	Direct Current
DIR	Direct Internal Reforming
EASA	Electrochemical Active Surface Area
EIS	Electrochemical Impedance Spectroscopy
FEM	Finite Element Method
FRA	Frequency Response Analyser
GDC	Gadolium-Doped CeO_2
HFI	High Frequency Impedance
HOR	Hydrogen Oxidation Reaction
LFI	Low Frequency Impedance
LSCF	$La_{1-x}Sr_xCo_{1-y}Fe_yO_3$
LSM	Strontium-Doped $LaMnO_3$
LSMG	$(La,Sr)(Mg,Ga)O_3$
mt-SOFC	Microtubular Solid Oxide Fuel Cell
MFI	Medium Frequency Impedance
MSR	Methane Steam Reforming
OCV	Open Circuit Voltage
ORR	Oxygen Reduction Reaction
PEMFC	Polymer Electrolyte Membrane Fuel Cell
RedOx	Reduction-Oxidation

S/C	Steam/Carbon Ratio
SEM	Scanning Electron Microscopy
SOFC	Solid Oxide Fuel Cell
SSZ	Scandia-Stabilized Zirconia
SYN	Syngas
TEM	Transmission Electron Microscopy
TPB	Triple Phase Boundary
YSZ	Yittria-Stabilized Zirconia

Chapter 1

Fundamentals

1.1 Introduction

The growing population of the world accompanied with the rising living-standards are raising the energy demand continuously. On the other hand, the depletion of the fossil fuel reserves associated with the global warming, the dominance of the energy security on the international relationships, and particularly the nuclear disasters have finally forced humans to harvest the renewable energy sources for utilizing in the environment-friendly energy conversion and storage systems. Owing to the severity of these evidences, and the occurrence probability of severer ones in the future, serious actions have being quickly taken at least in the industrialized countries. For instance, Japan has halted almost all nuclear power plants, and has been pushing for the "Green Society". Similarly, Germany has been reducing the dependence on nuclear power and increasing the renewable energy utilization.

Efficient use of energy has being globally more promoted, so that the conventional energy conversion technologies have been rather advanced. Similarly, the modern energy conversion technologies have being developed to harvest the renewable sources more efficiently. The developments have been as remarkable as that large scale solar and wind farms are being established all over the world. Fortunately, the environment-friendly energy conversion and storage technologies have been gaining the attention which has been overlooked

throughout the decades. Excitingly, various types of batteries have being developed and employed in a number of applications. For instance, electric vehicles have been produced usually for short range driving. Analogously, fuel cells, as zero-emission electrochemical energy conversion systems, have being developed and slowly commercialized for diverse applications. In 2014, the first commercial car (Toyota Mirai) has been released, which has overcome the driving range and the recharging issues of the electric vehicles. Simultaneously, fuel cells are developed for other applications, such as the residential and the regional power supply [6]. Attracting the second most attention after PEMFCs (polymer electrolyte membrane fuel cells), SOFCs (solid oxide fuel cells) have been often regarded as the strongest candidate for particularly large power demands. In this context, advancement of SOFCs has been quite promising for moving toward the 'Green Society'". This PhD study is thus devoted to improvement of SOFCs.

1.2 Basics of SOFC

1.2.1 The Technology

Essentially, all fuel cells lean upon the same principle (Fig. 1.1) that an exothermic reaction proceeding between a fuel and oxygen is rigorously controlled by directing the electrons exchanged for the exothermic reaction through a separated pathway to exploit for the power generation. Despite the same principle, fuel cells are classified with respect mainly to the employed electrolyte, as it dominates in selecting the operation conditions and complementary cell components. In this context, the core component of an SOFC is the ceramic-based electrolyte that requires relatively high operation temperature from 500 to 1000 $°C$ for a satisfactory ion/proton conduction. This high operation temperature has been the identity of SOFCs with the advantages and disadvantages listed in the following:

Advantages

- Employing non-precious catalysts in the electrodes, thus lower cost,
- High energy conversion efficiency,
- Relatively high power density [7],

- Releasing heat at high quality that can be utilized for cogeneration processes,
- Utilizing various fuels including hydrocarbons,
- Solid electrolyte [7].

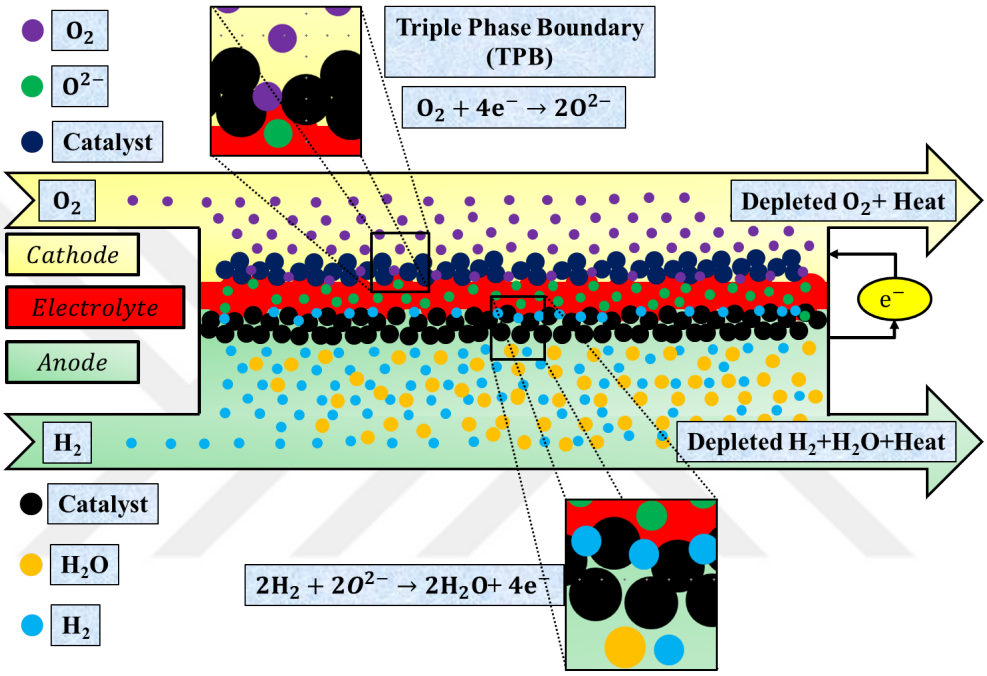

Figure 1.1: *The operation principle of SOFCs presented through the half cell reactions proceeding in the TPBs formed among the electrolyte and electrodes: anode and cathode, separately.*

Disadvantages

- Limited materials for sealing, current collection, etc.,
- Thermal stresses among the components,
- Structure degradations,
- Relatively expensive components/fabrication [7],
- Long start-up process.

1.2.2 Components

As for the other fuel cells, an SOFC fundamentally consists of three main components. The components are an electrolyte; and two electrodes: an anode and a cathode. Regarding the operation of an SOFC with hydrogen (fuel) and oxygen (oxidant), Fig. 1.1 illustrates the electrolyte and the electrodes with the respective physical/electrochemical processes. Essentially, the electrolyte is supposed to conduct the ions between the electrodes that are responsible to trigger the concerning half cell reactions with their specific (reducing/oxidizing) attributes, so that to direct the electrons through the external pathway.

Anode

The anode of an SOFC acts a reducing environment wherein the elementary HOR (hydrogen oxidation reaction)

$$2H_2 + 2O^{2-} \rightleftharpoons 2H_2O + 4e^- \tag{1.1}$$

is triggered, and water vapor is produced within the TPB (triple phase boundary). Eventually, the electrons are liberated to migrate toward the cathode for generating power.

As seen in Fig. 1.1, the TPB is the junction wherein the oxygen ions coming through the electrolyte and the hydrogen molecules transported by the anode react to produce water vapor for liberating the electrons. Namely, the anode must

- deliver the hydrogen molecules,
- catalyze the HOR,
- transport the liberated electrons toward the cathodes,
- sustain the chemical and thermal stability,
- and possess a CTE (coefficient of thermal expansion) matching to that of the other components.

These are achieved by the porous microstructure (Fig. 1.1). To ensure these properties, the anode is conventionally made of (non-precious) nickel. Although earlier anode materials

did not provide the ionic conduction, i.e., the TPB was only formed in the interface between the anode and electrolyte, the anode in the state-of-the-art SOFCs provides also the ionic conduction for expanding the TPB length [8]. The expansion of the TPB length into the anode is assured by adding an ionic conductor material, such as YSZ (yittria-stabilized zirconia) [9]. In addition to the ionic conductivity, YSZ suppresses the coarsening of nickel; and it reduces the mismatch among the coefficients of thermal expansion of the anode and electrolyte. Alternatively, ceria or ceria/strontium titanate mixtures as well as ceramic anodes, such as $(La, Sr)TiO_3$, $(La, Sr)CrO_3$ with addition of CeO_2 have being investigated [4, 7].

Cathode

The cathode of an SOFC is an oxidizing medium where the ORR (oxygen reduction reaction)

$$O_2 + 4e^- \rightleftharpoons 2O^{2-} \tag{1.2}$$

takes place in the TPB as shown in Fig. 1.1. For proceeding the ORR, the cathode must

- deliver the electrons liberated in the anode,
- transport the oxygen molecules,
- catalyze the ORR,
- maintain the chemical and thermal stability,
- and have a CTE matching to that of the other components.

As for the anode, these requirements are achieved by the porous microstructure as well. Because metals are not stable in oxidizing mediums at high temperature, the cathodes are usually made of ceramics; thus, the cathode shows lower electronic conductivity than the anode. One of the conventional cathode materials has been LSM (strontium-doped $LaMnO_3$). The TPB length is commonly extended by adding ionic conducting materials, such as YSZ [7, 9]. Alternatively, LSCF ($La_{1-x}Sr_xCo_{1-y}Fe_yO_3$) has been a potential cathode material for the moderate temperature operation. Another cathode material $Sm_{0.5}Sr_{0.5}CoO_3$ is currently under development. [7].

Electrolyte

Being the core component in SOFCs, the electrolyte must fulfill various demands. It must

- conduct the oxygen ions produced in the cathode as an ionic conductor,
- prevent the fuel cross-over between the anode and cathode as a sealant,
- inhibit the electronic conduction between the anode and cathode as an electronic insulator,
- be chemically and thermally durable,
- and posses a CTE matching to that of the other components.

The conventional electrolyte material has been YSZ that exhibits unsatisfactory ionic conductivity below 750 $°C$. Thereby, various novel electrolyte materials have being developed to obtain higher ionic conductivity at the moderate temperature level between 500-800 $°C$. SSZ (scandia-stabilized zirconia) shows higher conductivity; however, high cost of scandia accompanied with the degradations make this material less attractive. GDC (gadolinium- or samarium-doped CeO_2) yield high ionic conductivity below 600 $°C$, although they give high electronic conductivity and dimensional change in reducing environments at high temperatures. In addition to these fluorite structure oxides, perovskite structure materials, such as LSMG ($(La, Sr)(Mg, Ga)O_3$) have being developed as oxygen ion/proton conducting electrolytes despite the uncertainty in their chemical and mechanical instability [4, 7].

1.2.3 Energy Conversion Efficiency

Though SOFCs can generate power from various fuels, hydrogen is considered as the most promising energy carrier owing to its green product water vapor. Despite the proton conducting electrolytes are developed [10], SOFCs are identified with the ion conducting electrolytes. Besides, this PhD study was conducted on an SOFC comprising an ion conducting electrolyte. Therefore, hydrogen and the ion conducting electrolyte will be regarded throughout the analysis of the energy conversion efficiency.

As previously expressed, SOFCs generate power via the HOR (Eq. 1.1)

At 800 $°C$, the total enthalpy change of the HOR [7]

$$\Delta H^0 = -248.9\ kJmol^{-1} \tag{1.3}$$

Due to the entropy change ΔS^0, at 800 $°C$ the Gibbs free energy change of the HOR [7]

$$\Delta G^0 = \Delta H^0 - T\Delta S^0 = -191.3\ kJmol^{-1} \tag{1.4}$$

The electrical efficiency (ξ) of fuel cells is defined as the percentage of the extractable energy (ΔG^0) from the total energy (ΔH^0)

$$\xi = \frac{\Delta G^0}{\Delta H^0}\ 100 = 77.1\% \tag{1.5}$$

In principle, the thermodynamic potential (ΔG^0) is equal to electrical work W (J) that is a function of the electrical charge Q (C) and the electrical potential U^0 (V)

$$\Delta G^0 = -W = -QU^0 \tag{1.6}$$

The Faraday's law states that

$$Q = nF \tag{1.7}$$

where n is the number of moles of electrons exchanged per molecule of the reactant and F the Faraday's constant (96485 C/mol). When Q in Eq. 1.6 is substituted with Eq. 1.7, the thermodynamic potential can be rewritten as

$$\Delta G^0 = -nFU^0 \tag{1.8}$$

This equation allows for calculating the standard cell voltage as the difference between the standard potentials of the anode and cathode at 800 $°C$

$$\Delta G^0 = -nFU^0 \Rightarrow U^0 = 0.991\ V \tag{1.9}$$

However, the cell voltage U_{OCV} (V) can only approach the standard cell voltage due to the effects of temperature T (K) and the chemical activity (pressure/concentration) p_i (Pa) of the involving species i

$$U_{OCV} = U^0 - \frac{RT}{nF} \ln\left(\frac{p_{H_2O}}{p_{H_2} p_{O_2}^{0.5}}\right) \tag{1.10}$$

where R $(J/Kmol)$ is the ideal gas constant.

To achieve the theoretical cell voltage, which is practically referred to as "open circuit voltage (OCV)", a fuel cell must be under the thermodynamic equilibrium; namely, the HOR in the anode (Eq. 1.1) and the ORR in the cathode (Eq. 1.2) must proceed in the both directions at the same rate. To generate power, the system must move away from the equilibrium state through the irreversible polarizations discussed in the following.

Polarizations

For the power generation, the directions of the HOR and the ORR must be enforced to the right (Eqs. 1.1 and 1.2). This enforcement pushes the system from the thermodynamic equilibrium to the non-equilibrium state. As a result, the liberated electrons in the anode are enabled to move toward the cathode through the external pathway. The enforcement is achieved by the irreversible polarization (overpotential) η_{irev} (V) that reduces the cell voltage

$$\eta_{irev} = U_{OCV} - U_{cell} \tag{1.11}$$

The external electron flow rate (current) can be controlled by adjusting the cell voltage through a potentiostat/galvanostat. A rising current decreases the cell voltage; thus increases the polarization as the I-V curve in Fig. 1.2 illustrates. The relationship among the polarization and current may not be linear due to the fact that the polarization is the summation of the various components, which basically represent main processes manipulating the system performance; namely, activation η_{act} (V), ohmic η_{ohm} (V), and concentration polarizations η_{conc} (V).

$$\eta_{irev} = \eta_{act} + \eta_{ohm} + \eta_{conc} \tag{1.12}$$

Activation Polarization

The activation polarization is related to the rates of the HOR and the ORR. For each of these reactions, this relationship is well captured by the Butler-Volmer equation under the non-equilibrium state

$$i = i_0 \left\{ \exp\left(\frac{\beta n F \eta_{act}}{RT}\right) - \exp\left(\frac{-(1-\beta) n F \eta_{act}}{RT}\right) \right\} \tag{1.13}$$

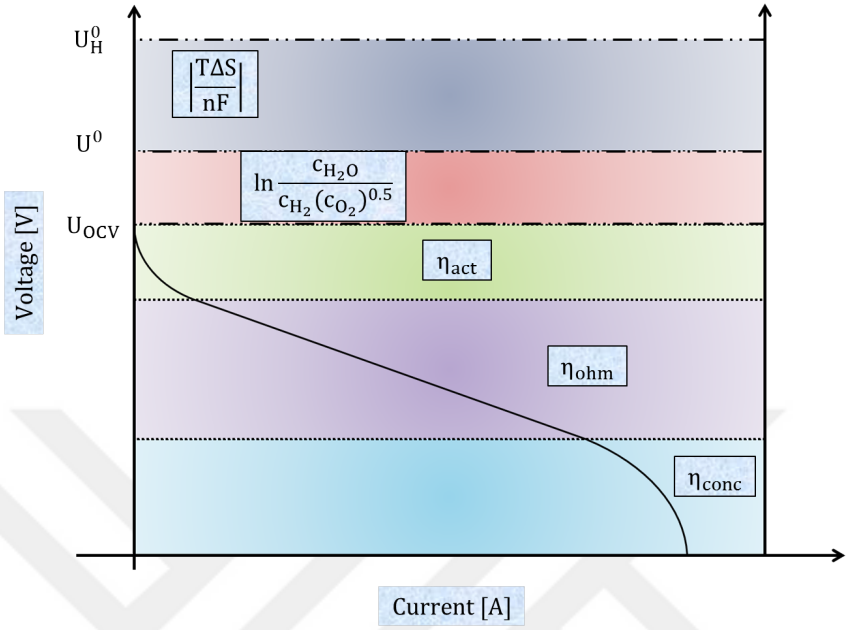

Figure 1.2: *Typical I-V curve of a fuel cell illustrating the polarizations sacrificed to generate power.*

where i (A/cm^2) is the current density, i_0 (A/cm^2) the exchange current density, and β the symmetry factor. In the high current region ($i \gg i_0$), as the HOR and ORR are forced to proceed to the right (Eqs. 1.1 and 1.2), Eq. 1.13 becomes

$$i = i_0 \exp\left(\frac{\beta n F \eta_{act}}{RT}\right) \Rightarrow \eta_{act} = \frac{RT}{\beta n F} \ln \frac{i}{i_0} \tag{1.14}$$

The HOR and the ORR diverge in terms of the kinetics, as the ORR requires a series of elementary reactions [4]. The respective activation polarizations differ in magnitude as well. At small current densities, the (total) activation polarization outweighs the other polarizations, and thus it yields an exponential voltage drop in the I-V curve depicted in Fig. 1.2. On the other hand, as Eq. 1.13 displays, temperature reduces the activation polarization, i.e., it increases the rate of the HOR and the ORR. Thanks to the high operation temperature of SOFCs, the activation polarizations tend to decrease, and that allows for employing non-precious metals as catalysts e.g., nickel, doped-ceria, etc. Consequently, the exponential voltage drop in the I-V curve might disappear.

Ohmic Polarization

As named after, the ohmic polarization η_{ohm} (V) obeys the Ohm's law defined as

$$\eta_{ohm} = iR_{ohm} \tag{1.15}$$

Since current and the ohmic polarization is linearly proportional, this polarization appears as a linear curve in the I-V curve (Fig. 1.2). The linear I-V curves often measured in SOFCs disclose then the fact that the ohmic polarization outweighs the other polarizations. Essentially, the ohmic polarization is built up due to the electrical resistances of the anode R_a (Ω) and cathode R_c (Ω); the electrolyte resistance against the ionic conduction R_{el} (Ω); and the contact resistance between the components R_{ec} (Ω)

$$R_{ohm} = R_a + R_c + R_{el} + R_{ec} \tag{1.16}$$

In fuel cells, the resistance is more specifically defined as the area specific resistance

$$RA = \frac{1}{\sigma_e}\delta \tag{1.17}$$

where δ (m), A (m^2), and σ_e (S/m) denote the thickness, the area, and the electronic/ionic conductivity of the component, respectively. Because the resistance of a component is directly proportional to its thickness, the thinner the component, the smaller the resistance.

The ionic conductivity of the electrolyte σ_{el} (S/m) is commonly described as

$$\sigma_{el} = \frac{A_0}{T}\exp\left(-\frac{E_{act}}{k_B T}\right) \tag{1.18}$$

where A_0 is the pre-exponential factor, k_B (J/K) the Boltzman constant, and E_{act} $(J/atom)$ the activation energy. In fact, the ohmic polarization in SOFCs is dominated by the high resistance of the ceramic-based electrolytes [6, 11, 12]. To reduce this resistance to a reasonable level, SOFCs are traditionally operated at high temperatures (Eq. 1.18). Because of the disadvantages arising from the high temperature listed in section 1.2, a remarkable effort is being recently invested in developing novel electrolyte materials with higher ionic conductivity at the moderate temperature level (500-800 $°C$) [4, 7, 13].

Concentration Polarization

While an SOFC is operating, the reactant flux J_R^* $(mol/m^2 s)$

$$J_R^* = \frac{i}{nF} \tag{1.19}$$

is consumed while the water vapor flux J_P^*

$$J_P^* = \frac{i}{nF} \tag{1.20}$$

is produced. Due to the resistance against the diffusion of the reactants to the TPB as well

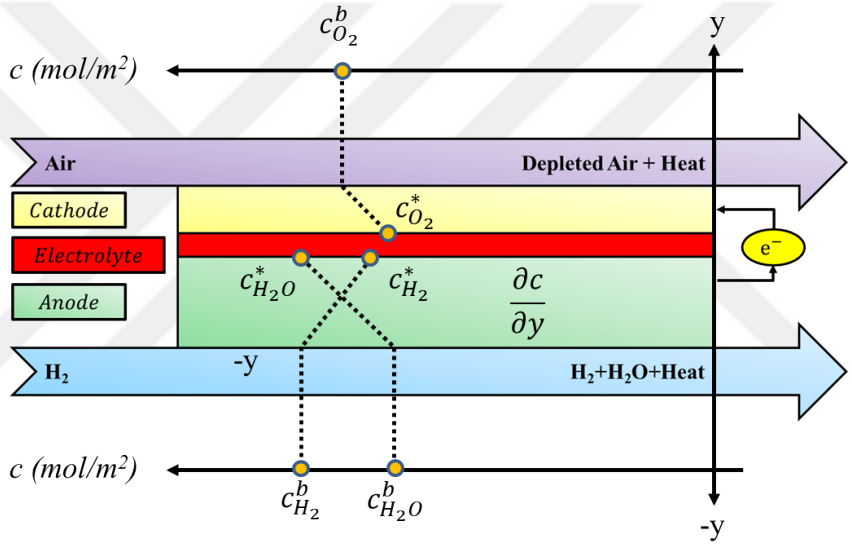

Figure 1.3: *The concentration gradients developing across the porous electrodes.*

as the removal of the product from the TPB within the porous electrodes, $c_R^b > c_R^*$, whereas $c_P^b < c_P^*$, as shown in Fig. 1.3. Owing to these concentration-gradients, the diffusion fluxes for the reactants J_R^{diff} and product J_P^{diff}

$$J_R^{diff} = J_R^* = -D_R \frac{\partial c_R}{\partial y} = -D_R \frac{c_R^* - c_R^b}{\delta} \tag{1.21}$$

$$J_P^{diff} = J_P^* = -D_P \frac{\partial c_P}{\partial y} = -D_P \frac{c_P^b - c_P^*}{\delta} \tag{1.22}$$

where D (m^2/s) and c_i (mol/m^3) stand for the diffusivity and the concentration of the species i, respectively. The relationship among current and the total polarization in the

anode comprising both the activation and the concentration polarization can be defined as

$$i = i_0 \left\{ \frac{c^*_{H_2}}{c^b_{H_2}} \exp\left(\frac{\beta n F \eta_a}{RT}\right) - \frac{c^*_{H_2O}}{c^b_{H_2O}} \exp\left(\frac{-(1-\beta) n F \eta_a}{RT}\right) \right\} \tag{1.23}$$

by explicitly stating the concentration dependence of the exchange current density

$$i_0 = n F c^*_{H_2} f_1 \exp\left(-\frac{E_{act}}{RT}\right) \tag{1.24}$$

in the Butler-Volmer equation (Eq. 1.13). Here, f_1 and E_{act} (kJ/mol) denote the decay rate of reactants to products and the activation energy, respectively.

With the increasing current, J^*_R and J^*_P grow proportionally. Thereby, the concentration gradients across the electrodes become larger, so that the concentration polarization rises. At very high current densities ($i \gg i_0$),

$$\exp\left(\frac{\beta n F \eta_a}{RT}\right) \gg \exp\left(\frac{-(1-\beta) n F \eta_a}{RT}\right) \tag{1.25}$$

As a result, Eq. 1.23 becomes

$$i = i_0 \frac{c^*_{H_2}}{c^b_{H_2}} \exp\left(\frac{\beta n F \eta_a}{RT}\right) \tag{1.26}$$

In this case,

$$\eta_a = \frac{RT}{\beta n F} \ln\left(\frac{i\ c^b_{H_2}}{i_0\ c^*_{H_2}}\right) \tag{1.27}$$

which can be written as

$$\eta_a = \frac{RT}{\beta n F} \ln\left(\frac{i}{i_0}\right) + \frac{RT}{\beta n F} \ln\left(\frac{c^b_{H_2}}{c^*_{H_2}}\right) \tag{1.28}$$

Since $\eta_a = \eta_{act,a} + \eta_{conc,a}$

$$\eta_{conc,a} = \frac{RT}{\beta n F} \ln\left(\frac{c^b_{H_2}}{c^*_{H_2}}\right) \tag{1.29}$$

On the other hand, when $i_0 \gg i$, the electrochemical reaction is limited by the diffusion process. Assuming $i/i_0 = 0$ at the thermodynamic equilibrium state

$$0 = \left\{ \frac{c^*_{H_2}}{c^b_{H_2}} \exp\left(\frac{\beta n F \eta_a}{RT}\right) - \frac{c^*_{H_2O}}{c^b_{H_2O}} \exp\left(\frac{-(1-\beta) n F \eta_a}{RT}\right) \right\} \tag{1.30}$$

Since $\eta_{act,a} \to 0$,

$$\eta_a = \eta_{conc,a} = \frac{RT}{nF} \ln \left(\frac{c^*_{H_2O} c^b_{H_2}}{c^*_{H_2} c^b_{H_2O}} \right) \tag{1.31}$$

The concentration polarization can be derived for the cathode in a similar way.

In fact, the effective diffusivity through the porous structures is related to the characteristic properties of the porous medium, for instance, porosity, pore diameter, and tortuosity. In this context, optimization of these properties can reduce the concentration polarization. As long as the inlet hydrogen flux $J^{in}_{H_2}$ is sufficiently high, the concentration polarization decreases. However, high hydrogen flux reduces the fuel stoichiometry

$$\lambda_{H_2} = \frac{J^*_{H_2}}{J^{in}_{H_2}} 100 \tag{1.32}$$

and thus decreases the energy conversion efficiency, provided the exhaust gas flow from the anode is not utilized for a secondary purpose, such as anode-off-gas recycling, and post-combustion, etc. However, under normal supply conditions, the concentration polarization becomes as severe as to limit the power density as depicted in Fig. 1.2.

Basically a similar situation exists in the cathode as air containing only 21% oxygen is supplied as oxidant. Thanks to the abundance of air, it is easy to supply at excess rates to suppress the concentration polarization.

1.2.4 Forms of SOFC

On the one hand, the high operation temperature of SOFCs provides various advantages listed in subsection 1.2.1. On the other hand, it causes thermal stresses among the components, threatening the mechanical stability of the cell, as broadly discussed in subsection 1.3.3. In order to cope with the thermal stresses, SOFCs are designed in various forms. From the main planar and tubular forms illustrated in Fig. 1.4, several forms, e.g., flat-tubular, honeycomb, and microcone, etc. have been derived.

The planar-SOFCs are recognized with high (volumetric) power density, high modularity, and low cost; however, they are vulnerable to the thermal stresses. In contrast, the tubular-SOFCs exhibit moderate power density, low modularity, and high cost; but they are robust

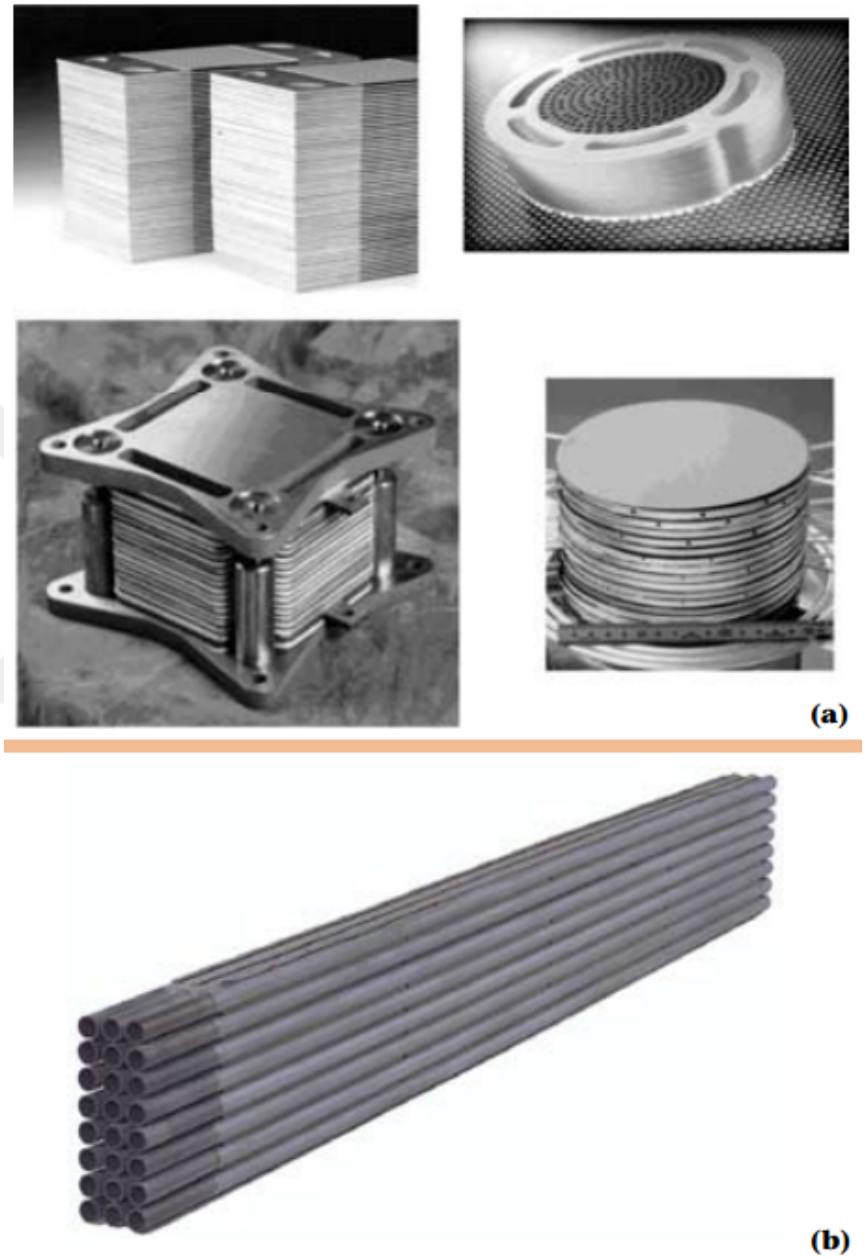

Figure 1.4: *Basic forms of SOFCs: a) Planar-SOFCs designed in various shapes and b) tubular-SOFCs [4].*

against the stresses [6, 13–16]. The flat-tubular-SOFCs blend the advantages of both the planar and the tubular forms; namely, they show high power density [17] as well as high strength [18]. The honeycomb-SOFCs are identified with high volumetric power density [19, 20]; however, it is expensive to fabricate such a structure. The microcone-SOFCs are developed for improving the volumetric power density of the tubular form [21–23].

As summarized, all the SOFC forms have advantages and disadvantages. Therefore, they are all being developed according to the application. For instance, tubular-SOFCs are developed for stationary power generation, where the strength outweighs the other parameters. Planar-SOFCs are developed for transportation, wherein the volumetric power density matters [6].

In addition to the form, dimension is an effective parameter on the performance and durability of SOFCs. Particularly, miniaturization of tubular-SOFCs yields promising (volumetric) power density and higher modularity while sustaining the strength against the thermal stresses. Tubular-SOFCs with diameters as small as a few micrometer are being developed and referred to as mt-SOFC (microtubular-SOFC) [11, 14, 24]. Referring to the challenging start-up process in SOFCs, mt-SOFCs can be started in relatively shorter time. These features render mt-SOFCs rather promising for various future applications [11, 14]. Nonetheless, the concentration polarization and its impacts on mt-SOFCs deserve further investigations to improve their performance and durability.

1.2.5 Types of SOFC

In order to reduce the irreversible polarizations, the SOFC components are designed rather thin; in the micrometer range. Though it is desired to design all the components very thin, this desire cannot be realized; because a sustainable mechanical strength is required. The mechanical strength is ensured by providing larger thickness in one of the components as the supporter. Therefore, there are three types of SOFCs: electrode (anode/cathode)-supported, and electrolyte-supported [7] .

From a microstructure point of view, the anode and cathode are porous, whereas the electrolyte is relatively dense. The electrolyte-supported type thus exhibits the highest

mechanical strength; however, it gives rise to quite high ohmic polarizations at a sustainable thickness (Eq. 1.16). Though the anode- and cathode-supported types reduce the ohmic polarizations, allowing for operation at lower temperatures, they raise the activation and concentration polarizations [11,12,25]. Nonetheless, particularly, the anode-supported type yields high power density as well as sufficient strength at a particular thickness; and thus it has been superior to the cathode and electrolyte-supported types [6, 26, 27]. In this respect, the planar-SOFCs are usually designed as the electrolyte-supported, whereas the tubular-SOFCs are designed as the anode-supported for ensuring the durability of the systems.

1.3 Background of Dissertation

1.3.1 Current Variations

The power generation in SOFCs via oxidizing hydrogen with oxygen flowing in the respective flow channels is illustrated in Fig. 1.5. For an infinitesimal current density ∂i

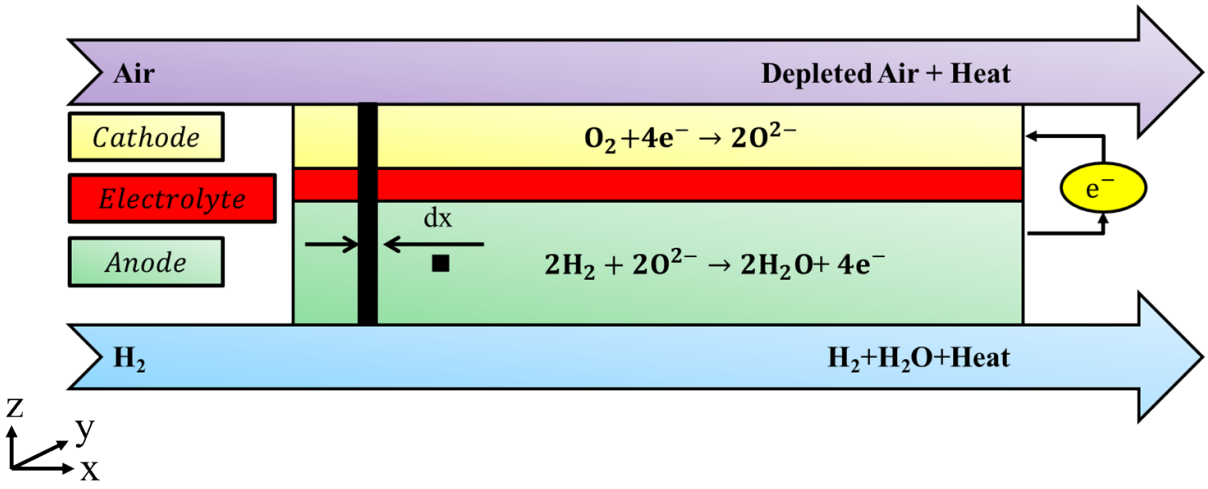

Figure 1.5: *The power generation principle of SOFCs by using hydrogen and oxygen flowing in the regarding flow channels.*

generated within an area of ∂x (for the unit width) depicted in Fig. 1.5, the consumed

reactant fluxes can be written as

$$\partial J^*_{H_2} = \frac{\partial i}{n_{H_2} F} \qquad \partial J^*_{O_2} = \frac{\partial i}{n_{O_2} F} \tag{1.33}$$

according to the Faraday's law in the anode and cathode, respectively. Here,

$$\partial i = \frac{\partial I}{\partial x} \tag{1.34}$$

Since the consumed reactants are converted to the water-vapor

$$-\frac{\partial J^*_{H_2}}{\partial t} = \frac{\partial J^*_{H_2O}}{\partial t} = -\frac{1}{2}\frac{\partial J^*_{O_2}}{\partial t} \tag{1.35}$$

the concentrations of the reactants and product vary as

$$-\frac{\partial c^*_{H_2}}{\partial t} = \frac{\partial c^*_{H_2O}}{\partial t} = -\frac{1}{2}\frac{\partial c^*_{O_2}}{\partial t} \tag{1.36}$$

Regarding the continuous flow of the reactants and product along the respective flow channels within the electrodes, the longitudinal concentration variation can be expressed as

$$-\frac{\partial c^*_{H_2}}{\partial x} = \frac{\partial c^*_{H_2O}}{\partial x} = -\frac{1}{2}\frac{\partial c^*_{O_2}}{\partial x} \tag{1.37}$$

As stated by Eq. 1.23, for a constant η_a comprising the concentration and the activation polarizations in the anode, current is a function of the reactant and product concentrations. Because the concentrations vary along the channel, Eq. 1.23 becomes

$$i(x) = i_0 \left\{ \frac{c^*_{H_2}(x)}{c^b_{H_2}(x)} \exp\left(\frac{\beta n F \eta_a}{RT}\right) - \frac{c^*_{H_2O}(x)}{c^b_{H_2O}(x)} \exp\left(\frac{-(1-\beta) n F \eta_a}{RT}\right) \right\} \tag{1.38}$$

Since the drops in the reactant concentrations give rise to the product concentration,

$$i(x) = i_0 \left\{ \frac{c^*_{H_2}(x) - \frac{\partial c^*_{H_2}}{\partial x}}{c^b_{H_2}(x) - \frac{\partial c^*_{H_2}}{\partial x}} \exp\left(\frac{\beta n F \eta_a}{RT}\right) - \frac{c^*_{H_2O}(x) + \frac{\partial c^*_{H_2O}}{\partial x}}{c^b_{H_2O}(x) + \frac{\partial c^*_{H_2O}}{\partial x}} \exp\left(\frac{-(1-\beta) n F \eta_a}{RT}\right) \right\} \tag{1.39}$$

current decreases along the channel. This longitudinal decrease in the current is equivalent to the reversible voltage-loss referred to as "Nernst-loss" [28, 29].

1.3.2 Temperature Variations

While converting the chemical energy of hydrogen into power through the HOR at current density i, heat $\dot{q}_{tot}$ (W/m^2) is unfavorably released due to the entropy change Δs $(J/mol\ K)$ and Nernst-loss, together categorized as the reversible polarization η_{rev}; and due to the activation, ohmic, and concentration polarizations, categorized as the irreversible polarization η_{irev}, as given in the following equation

$$\dot{q}_{tot} = i\,(\eta_{rev} + \eta_{irev}) \tag{1.40}$$

At a given polarization η_{tot}, which includes both the reversible and irreversible contributions, current varies along the channel owing to the concentration variations, assuming that the variations in the other directions are negligible. As a result, the heat production rate becomes a function of the position

$$\dot{q}_{tot}(x) = i(x)\ \eta_{tot} \tag{1.41}$$

implying that temperature is also a function of position along the channel.

On the other hand, the released heat is removed through the conductive, radiative, and convective heat transfer processes to maintain the cell temperature at a desired level. The conductive heat transfer along the x axis can be defined according to the Fourier's law as

$$\dot{q}_{cond}(x) = -k\frac{\partial T_s}{\partial x} \tag{1.42}$$

Due to the large temperature difference between the cell and ambient temperature, radiant heat transfer plays an important role. According to the Stefan-Boltzman law, the maximum rate of radiation emitted from a black body at the position of x

$$\dot{q}_{emit,max}(x) = \sigma_{SB} T_s^4(x) \tag{1.43}$$

where σ_{SB} is the Stefan-Boltzman constant. In fact, the emissivity of a real object ϵ diverges from the unity $(0 \leq \epsilon \leq 1)$ that adopted for the black body. This divergence modifies Eq. 1.43 as

$$\dot{q}_{emit}(x) = \epsilon\sigma_{SB} T_s^4(x) \tag{1.44}$$

Additionally, the absorptivity of a real object α departs from that of the black body ($0 \leq \alpha \leq 1$). As a result, the absorbed heat from the surrounding is defined as

$$\dot{q}_{abs}(x) = \alpha \ \dot{q}_{inc}(x) \tag{1.45}$$

where $\dot{q}_{inc}$ (W/m^2) denotes the incident radiation.

In this case, the net radiant heat transfer at the position of x can be expressed as follows

$$\dot{q}_{rad}(x) = \dot{q}_{abs}(x) - \dot{q}_{emit}(x) \tag{1.46}$$

Owing to the continuous flow of the reactant and product gases, the convective heat transfer is also effective for removing the heat from cell. Depending on the heat transfer coefficient h (W/m^2K) and the inlet gas temperature T_∞, the convective heat transfer at the position of x can be written according to the Newton's law as

$$\dot{q}_{conv}(x) = h(T_s(x) - T_\infty) \tag{1.47}$$

Depending on the balance between the heat production rate and the total heat transfer rate, consisting of the conductive, convective, and radiant heat transfer rates, the surface temperature differentiates along the channel

$$T_s = f(x) \tag{1.48}$$

Herein the surface temperature refers to either of the anode or cathode. Thanks to the rather small thickness and high thermal conductivity (k (W/m^2K)) of the components (subsection 1.2.2), the temperature difference among the components in the through-plane direction (y-direction in Fig. 1.5) is numerically estimated to be trivial.

Endothermic cooling

Despite hydrogen is considered in the previous analyses, the tolerance of SOFCs to the hydrocarbon fuels is one of their advantages. As depicted in Fig. 1.6, there are two driving forces for sticking on the hydrocarbon fuels. Firstly, the infrastructure for storing and distributing hydrogen is yet insufficient, whereas the storage and distribution of hydrocarbons is relatively easy. In fact, methane (in the city gas) is effectively distributed all over

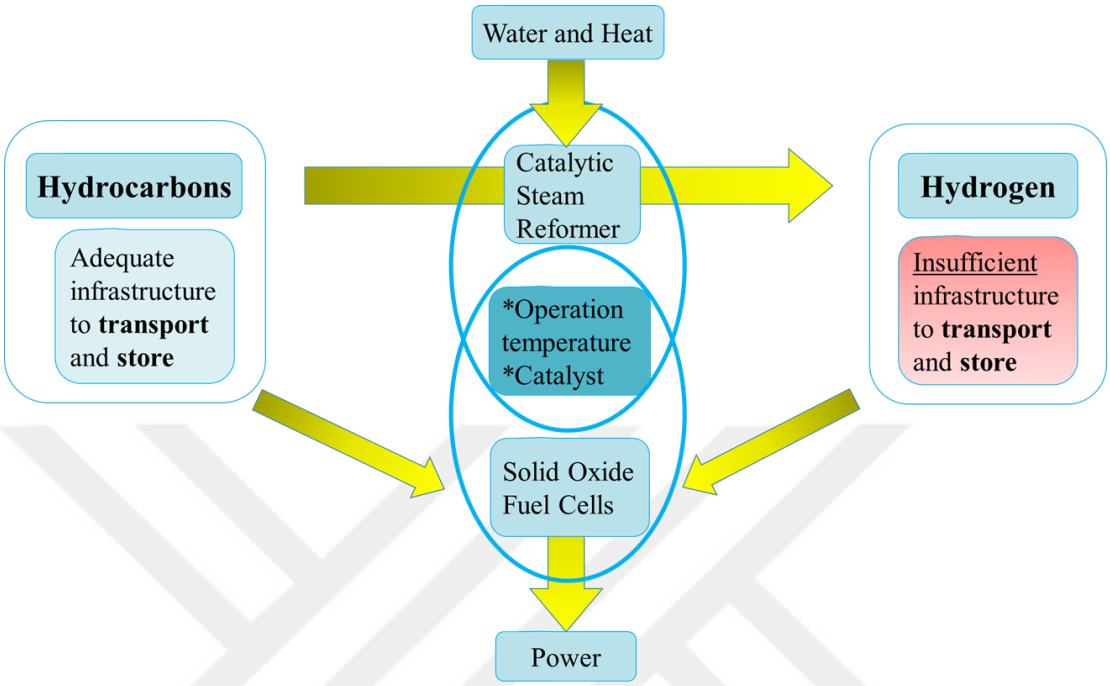

Figure 1.6: *The concept of direct internal reforming in SOFCs.*

the globe. Secondly, at the moment, the most of hydrogen (ca. 96%) is produced from hydrocarbons via various processes [30]; thus, the direct use of hydrocarbons theoretically is more efficient owing to the reduced entropy loses [31]. Thanks to these convincing facts, various hydrocarbon fuels, such as methane, ethane, and butane, etc. are under investigation to utilize for power generation in SOFCs. Among them, methane has been regarded as the most promising fuel.

Nickel being the most commonly used catalyst of SOFCs is very active for methane cracking reaction

$$CH_4 \rightleftharpoons C + 2H_2 \tag{1.49}$$

which leads to "carbon deposition", resulting in irreversible degradations, as discussed in subsection 1.3.3. Therefore, the electrochemical oxidation of methane has been achieved for only short-term. Similarly, the "dry methane reforming" often terminates the cell operation with the carbon deposition. Fortunately, methane has being successfully reformed via the

endothermic MSR (methane steam reforming) reaction

$$CH_4 + 2H_2O \rightleftharpoons CO_2 + 4H_2 \qquad \Delta H = -195.8\ (kJ/mol) \tag{1.50}$$

As shown in Fig. 1.6, hydrogen is usually produced through the MSR in the catalytic steam reformers, where nickel is employed as the catalyst as well. The operation temperature of the catalytic reactors approaches to the typical operation temperature of SOFCs. These analogies have been inspiring for the unification of the MSR and the HOR in SOFCs and referred to as "direct internal reforming". Although, the original idea is to exploit the water-vapor and heat produced by the exothermic HOR for the endothermic MSR, unfortunately this idea can only partially be realized due to the carbon deposition. Thereby, methane is fed along with steam at a particular S/C (steam/carbon) ratio to prevent the carbon deposition.

Depending on the concentration of the species, the rates of the HOR and the MSR reaction change along the channel. It is often reported that the MSR reaction rate is rather high in the fuel inlet vicinity and decreases longitudinally. Depending on the rate of the MSR reaction, the SOFC is cooled down at longitudinally varying degrees via the "endothermic cooling". This type of cooling is expected to be rather effective according to the numerical calculations.

1.3.3 Consequences of Longitudinal Variations

In the previous subsections (1.3.1 and 1.3.2), the longitudinal concentration, current, and temperature variations were theoretically derived and explained. The variations are likely to result in performance and structure degradations in SOFCs. The relationships among the degradations and the variations are depicted in Fig. 1.7; and discussed in the following.

Performance Degradation

Arising mainly from the longitudinally growing concentration polarization including the Nernst-loss toward the fuel outlet under the assumption of negligible concentration polarization in the cathode, the current variation results in power-loss that is referred to

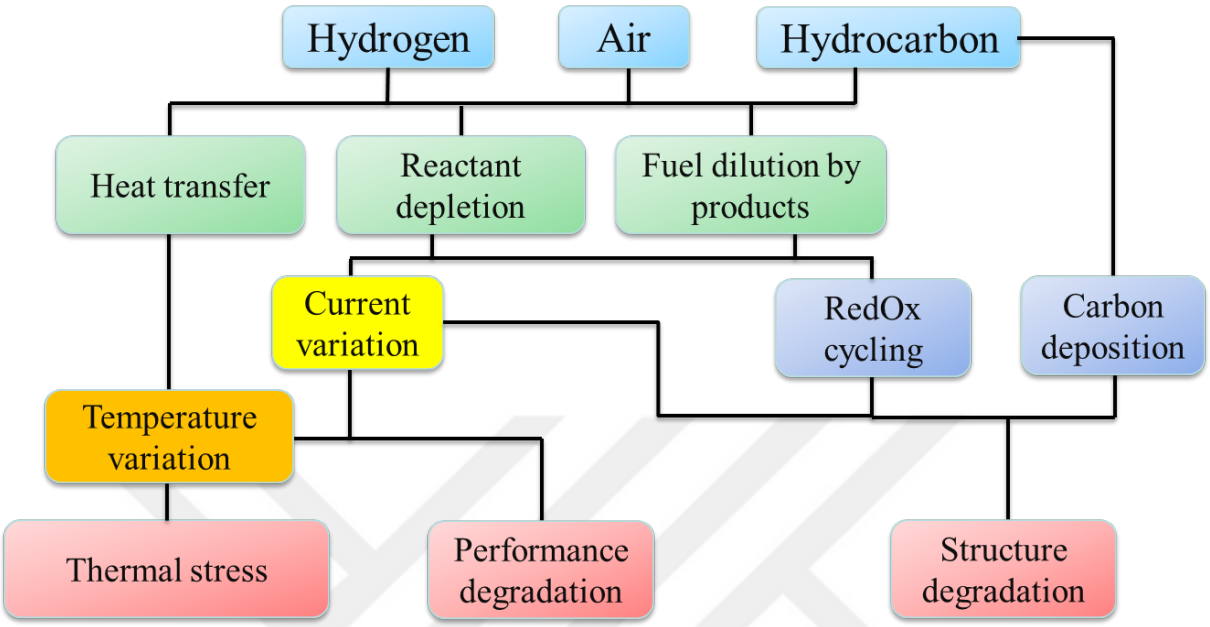

Figure 1.7: *Concentration, current, and temperature variations and consequential performance and structure degradations while utilizing hydrogen as well as hydrocarbon.*

as "performance degradation". This sort of degradation implies that the electrochemical capacity of the active area within the cell cannot be effectively exploited as explained in the following.

Since current is a function of the distance from the fuel inlet, the total current produced along the channel (Fig. 1.5) for the unit width can be defined as

$$I_{tot} = \int_0^x i(x)dx \tag{1.51}$$

Assuming that the electrochemical capacity of the cell is maximum in the fuel inlet, wherein the concentration polarization tends to minimize, the total electrochemical capacity of the cell can be expressed as

$$I_{cap} = \int_0^x i(0)dx = i(0)\int_0^x dx \tag{1.52}$$

In this case, the performance degradation can be written as

$$I_{cap} - I_{tot} = i(0)\int_0^x dx - \int_0^x i(x)dx = \int_0^x (i(0) - i(x))dx \tag{1.53}$$

Note that the smaller the activation polarization in the cell, the larger the maximum current in the fuel inlet; however, the bigger the current drop toward the fuel outlet. As explained in subsection 1.2.3, the high operation temperature of SOFCs favors the HOR and ORR. As a result, the respective activation polarizations become small while the performance degradation large. From this point of view, the diagnosis and mitigation of the performance degradation is of great importance. For the diagnosis, the in-situ longitudinal characterization of the active area would provide sufficient knowledge to estimate the extent of the degradation. In this way, the cell geometry, referring to the dimension and form, and the microstructure of the cell components could be modified to mitigate the current variations.

Thermal stresses

The mechanical failure of SOFCs is mainly ascribed to the thermal stresses emerging among the cell components [1, 32, 33]. Essentially, thermal stresses are related to the volumetric thermal expansion of a component that is a function of temperature and the volumetric CTE (coefficient of thermal expansion)

$$\alpha_v = \frac{1}{V}\frac{\partial V}{\partial T} \tag{1.54}$$

where V (m^3) stands for volume of the component.

As explained in subsection 1.2.2, SOFCs are composed of the ceramic-based components. Thereby, the CTE differs among the components, and the differences give rise to the thermal stresses in conjunction with temperature.

To achieve the desired functionality from the ceramic-based components, they are exposed to heat treatment processes at high temperature (1000-1450 $°C$). Conventionally, the heat treatment processes are carried out at distinct temperatures in the given range for each component, consecutively. Due to this consecutive thermal cycles, the induction of the residual stresses is indispensable. As a result, operating SOFCs inherently accommodate (residual) stresses. Similarly, additional residual stresses are induced during thermal cycles for the occasional shut-down processes [34]. On the other side, temperature varies along the channel in relation with the current variations and the heat transfer processes,

as clarified in the subsection 1.3.2. In this circumstance, the residual stresses are presumably accompanied with the thermal stresses emerging from the longitudinal temperature variations [1, 32, 35–37].

In order to reduce the residual stresses, there have been various attempts, such as conducting the heat treatment for all the cell components at once, and controlling the temperature ramp, etc. However, the severity of the stresses stemming from the longitudinal temperature variations has not yet been clarified. Although there have been some numerical studies leaning either upon particular assumptions for the longitudinal temperature variations [1] or upon the thermo-electrochemical models predicting the variations [32,35,36,38], the temperature variations have not yet been in-situ characterized. Thereby, the in-situ characterization of the variations with feasible methods for mitigating/eliminating them is substantial.

Structure Degradations

Although nickel has being regarded as the most appropriate element for the anode in an SOFC, its instability under electrochemically harsh conditions poses serious degradation issues. Depending on the operation conditions, the degradations can be as harmful as to terminate the power generation as explained in the following.

RedOx Cycling

It is stated in subsection 1.2.2 that the nickel-coarsening (happening at high temperature) is suppressed by the addition of more stable YSZ. Namely, the anode is usually made of Ni/YSZ cermet. In fact, at high temperatures nickel oxidizes easily through

$$2Ni + O_2 \rightleftharpoons 2NiO \tag{1.55}$$

This implies that the cermet anode is originally made of NiO/YSZ, since the anode is fabricated through the sequential heat treatment processes at high temperature (subsection 1.3.3). At this state, the anode is not porous indeed. Thanks to the fact that the molar volume of nickel oxide is 1.66 times of that of nickel, the porous cermet anode (Ni/YSZ) is obtained through [39, 40]

$$NiO + H_2 \rightleftharpoons Ni + H_2O \tag{1.56}$$

In other words, upon subjecting the anode to hydrogen, the YSZ phase remains stable, whereas the nickel oxide particles are converted to the smaller nickel particles, forming the pores as sketched in Fig. 1.8. However, this porous structure is not stable at all; the nickel particles keep coarsening with time, despite the stable YSZ. Besides, if the cermet anode is somehow exposed to an oxygen containing environment at high temperatures (above 600 $°C$), the nickel particles can readily re-oxidize, and thus convert back to the larger nickel oxide particles. Such a reduction/oxidation cycle is known as "RedOx cycling", which can result in the following irreversible structure degradations: i) the catalyst loading of the anode reduces, so that TPB length becomes smaller, deteriorating the electrochemical performance, ii) if the RedOx cycles take place consecutively, the destructive micro-crack formation in the anode as well as the adjacent electrolyte can occur. In order to avoid the

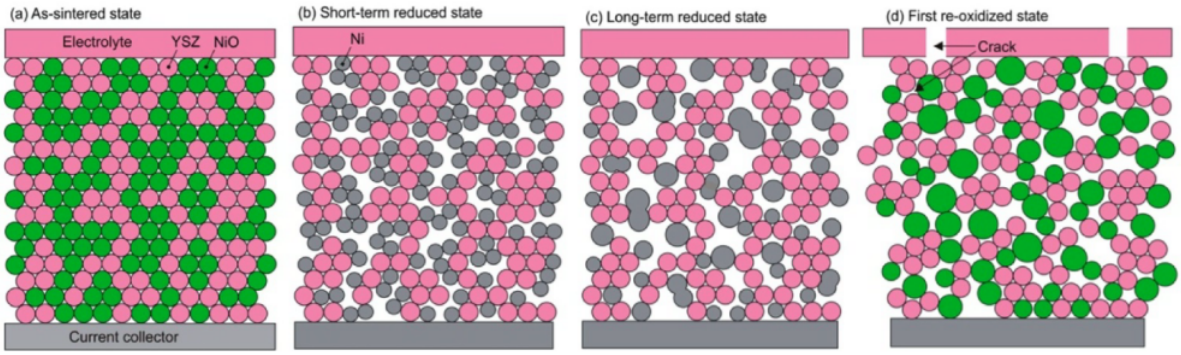

Figure 1.8: *Modification of the Ni/YSZ anode's microstructure at various states including the RedOx cycling [5]. In this figure, YSZ, NiO, and Ni are illustrated by pink, green, and dark-blue, respectively.*

RedOx cycling, the cermet anode must be isolated from the oxygen containing environments via robust sealing and supplying an inert gas during standby modes. Nonetheless, at high fuel stoichiometry, the Nernst-loss rises toward the fuel outlet. As a result, the oxygen partial pressure can locally increase up to a critical value, and that intuitively increases the risk of the RedOx cycling. In terms of diagnosing the risk of RedOx cycling due to the Nernst-loss, the longitudinal characterization of SOFCs is of great importance.

Carbon Deposition

Nickel is a very good catalyst for the HOR as well as the methane cracking reaction. Therefore, when the hydrocarbon fuels are in use via the electrochemical oxidation and the dry reforming, carbon can deposit on the nickel catalysts (particles). The deposition is classified under three different groups: pyrolytic, encapsulating (gum), and whisker carbon deposition [41]. Though the pyrolytic and the encapsulating carbon depositions block the pores within anode and degrade the catalytic activity, the whisker carbon deposition can destroy the catalyst's structure.

Even though it is less pronounced with the direct internal reforming process (Eq. 1.50), the carbon deposition takes place at low S/C ratios. When the deposition is intended to be inhibited by keeping the S/C ratio sufficiently high, the Nernst-loss becomes effective on the energy conversion process. During the internal reforming, both the HOR and MSR proceed simultaneously, so that the degree of the carbon deposition depends on the rates of these reactions. In this respect, the deposition is related to the local conditions, such as current, temperature, concentration of the involving species, as they influence the reaction rate of the internal reforming reactions. In order to understand the relationship among the carbon deposition and the local operating properties, the longitudinal characterization of SOFCs is also crucial. Such an understanding is believed to allow for modifying the cell microstructure for mitigating/eliminating these degradations.

1.3.4 Scope of Dissertation

As described in the previous subsections, the longitudinally varying concentration, current, and temperature cause the performance and structure degradations in SOFCs. Spatial investigations of the degradations through the varying electrochemical (current, voltage) and the physical (temperature, microstructure) properties are of great importance for improving the performance and durability of SOFCs. Such investigations are promising for gathering fundamental understanding to mitigate/eliminate the degradations, and for developing the SOFC geometries and materials further.

In the last decades, there have been valuable attempts to longitudinally characterize the current variations with appropriate experimental methods [42–49]. Even though these methods were applied in varying means, they are generally referred to as "segmentation".

The segmentation method rests on the division of the electrochemical active area into small compartments called "segments", which are electronically isolated from each other. The segments' dimensions and amounts are determined according to the gas flow fields; so that the desired resolution is achieved. The segments are individually characterized by various electric loads and impedance spectroscopies. Eventually, longitudinally resolved electrochemical properties are analyzed, and representing conclusions are deduced.

The segmentation method can be applied on SOFCs to characterize the longitudinal current and temperature variations in SOFCs and the relationship among the variations. To prevent the degradations stemming from the variations, specific countermeasures can be taken. Metzger et al. applied the segmentation method on a planar-SOFC, where they segmented all the components (gas distribution plates, anode, and cathode) of an SOFC except the electrolyte [50,51]. The realization of such a segmented planar-SOFC for the spatial characterization requires specific design, manufacture, and assembly processes, which demand significant amount of investment. Shimizu et al. implemented the segmentation method on a mt-SOFC (microtubular-SOFC) [52], where they segmented only the cathode of the mt-SOFC. In comparison with the planar-SOFC, the realization of the segmented mt-SOFC seems much simpler.

Bearing in mind that SOFCs are being developed in the various forms, development of a universal characterization method that is easily applicable onto tubular, planar and other forms of SOFCs is highly desired. In this regard, numerical models are quite practical, providing high resolution, reducing investigation time and expenses, and avoiding the experimental difficulties stemming from the high operation temperature. Nonetheless, the numerical models are required to be validated with reliable experimental results.

This PhD study is thus devoted to elaborating the current and temperature variations along mt-SOFCs utilizing hydrogen and hydrocarbon (syngas) by applying the segmentation method along with a finite element model to improve the reliability of the numerical SOFC tools for computing the spatial variations in the characteristic properties. Since the segmentation method can easily be realized on mt-SOFCs [52], the study was carried out in mt-SOFCs.

Chapter 2

Longitudinal Measurement of Characteristic Properties in Microtubular-SOFCs

2.1 Segmentation

In order to experimentally analyze the processes associated with spatially varying properties in SOFCs, such as concentration of species, current, and temperature, appropriate spatial characterization methods have been developed. Although the sophisticated "Vibrational Raman Scattering" and "Infra-red Temperature Measurements" are available for identifying spatial concentration and temperature variations [53–55], respectively, they require particular modifications on the cell design, e.g., transparent windows, etc. On the other hand, "segmentation" method appears to be more advantageous mainly from the points of simplicity and cost. The segmentation refers to the division of the EASA (electrochemical active surface area) of a cell into small partitions (Fig. 2.1), called "segments", which should be electronically isolated from each other for measuring spatial current and temperature variations, from which the linked concentration variations can be extracted.

The segmentation method is extensively applied in PEMFCs (polymer electrode membrane

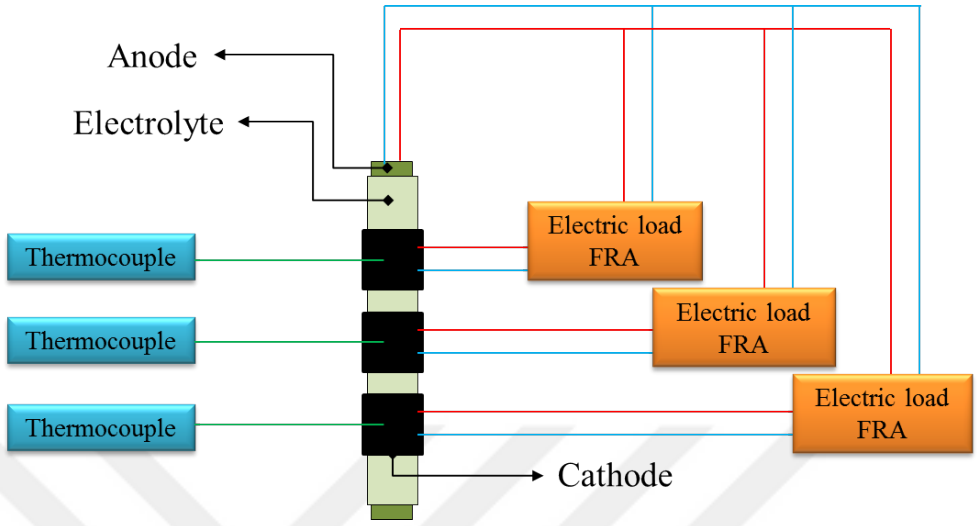

Figure 2.1: *Schematic of an anode-supported mt-SOFC onto which the segmentation method is applied for measuring longitudinal current, temperature, and impedance variations.*

fuel cells), where it is usually realized on gas distribution plates due to practical limitations. In this method, the EASA is not virtually splitted into segments; namely, the charge transport among the segments is not completely obstructed. In other words, depending on the potential difference between the segments, charge might flow among the segments. In the case of charge flow, accuracy of the spatial measurements becomes questionable. It is hence obligated to establish identical potential for all the segments. Depending on the size of the segments, the resolution of the spatial characterization can be adjusted; the smaller the dimension of the segment, the higher the spatial resolution.

2.2 Fabrication of Segmented mt-SOFCs

The process-flow for fabricating the segmented mt-SOFCs (microtubular-SOFCs) is illustrated in Fig. 2.2. The tubular anode substrates were manufactured by Repton Co. Ltd., Japan. These substrates were composed of NiO/YSZ (65:35 $wt\%$); upon reduction, they yield $\approx 37\%$ porosity. After dip-coating with $8YSZ$ electrolyte at room temperature, the substrates were sintered at 1420 $^{\circ}C$ for two hours. By masking the electronically-isolated

areas for the segmentation, the cathode slurry of $La_{0.7}Sr_{0.3}MnO_3/YSZ$ ($10:3wt\%$, Daiichi Kiganso Kagaka Kogyo Co. Ltd., Japan) was brush-coated onto the electrolyte surface at room temperature. Subsequently, the cathodes were sintered at 1050 $^{\circ}C$ for two hours. Ultimately, the segmented mt-SOFCs were obtained with the dimensions displayed in Fig. 2.7. Moreover, silver-paste was brush-coated onto the cathode surfaces at room temperature to enhance the electronic conductivity.

Since all the SOFC components were made of ceramic-based materials, full-segmentation of the EASA of the electrodes was indeed possible to inhibit the charge transport among the segments. However, we could have segmented only cathode, since anode was functioning as the electrode as well as the mechanical support. Given anode was made of highly conductive Ni/YSZ, charge might have flown among the segments depending on the spatial potential difference. We hence opted potentiostatic measurements where the same potential was applied on all the segments. The cathode of the cell was divided into three segments, as shown in Fig. 2.2. Although a higher spatial resolution could be realizable, the configuration of the peripheral equipment would be rather impractical.

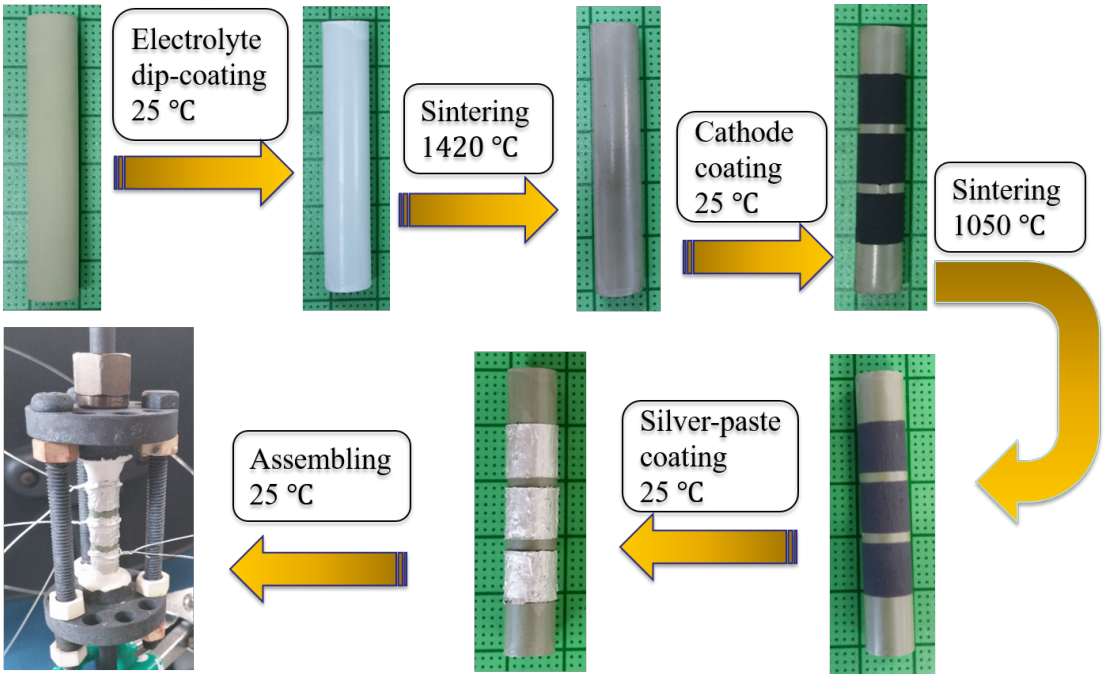

Figure 2.2: *The process flow for fabricating segmented mt-SOFCs.*

2.3 I-V Curve

Alike other electrochemical systems, such as battery, electric double layer capacitor, etc., performance of SOFCs is essentially characterized with current and voltage properties. These properties are measured with the aid of electric loads in either galvanostatic or potentiostatic modes referring to the constant-current or constant-voltage, respectively. Conventionally, current is plotted against voltage and the emerging curve is called as "I-V curve" as shown by Fig. 1.2. The I-V curve measurement is regarded as the fundamental characterization method. In fact, I-V curves appear with characteristic shapes representing the main processes within the systems.

2.4 Electrochemical Impedance Spectroscopy

Despite the I-V curve of a fuel cell provides general and quantitative information about the concerning processes, more detailed information is required to clarify the fundamental phenomena. This requirement is satisfactorily met by EIS (electrochemical impedance spectroscopy) which is a well established and non-intrusive characterization method applied in various disciplines as well as in fuel cells. Depending on the frequency range, EIS has the competence to quantify diverse physical and electrochemical processes simultaneously occurring within a cell. Thereby, it is extensively used in SOFCs to characterize the electrical and electrochemical charge transfer, and the mass transport processes.

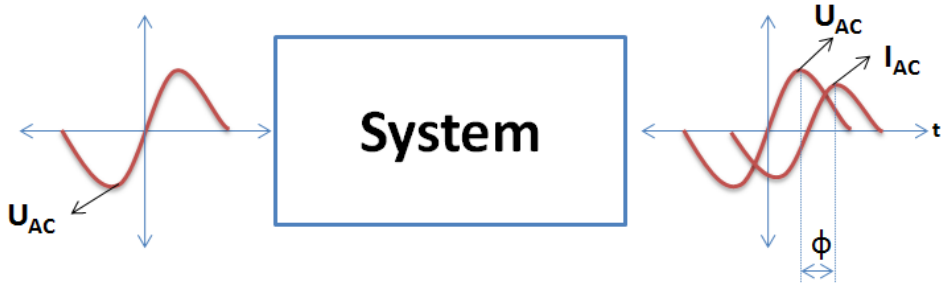

Figure 2.3: *The principle of the EIS measurement.*

EIS measurements are carried out via exciting the diagnostic system at the steady-state

and then detecting the response of the system as depicted in Fig. 2.3. When the excitement signal is a voltage (U (V)), the response signal must be a current (I (A)) and vice versa. The relationship among the voltage and current signals is defined as "impedance" according to the Ohm's law

$$Z(t) = \frac{U(t)}{I(t)} \tag{2.1}$$

Apart from the resistance, the impedance is defined with a phase and a magnitude. The phase refers to the shift among the voltage and current signals at a given frequency as displayed in Fig. 2.3. With this more comprehensive definition, the impedance can represent the resistive property of other circuit elements, such as capacitors and inductors; rather than solely resistors. As the resistive property of capacitors and inductors depends on the frequency, the impedance is a function of the frequency, unlike the resistance of the resistors. Considering as the excitement signal in an EIS measurement, a sinusoidal

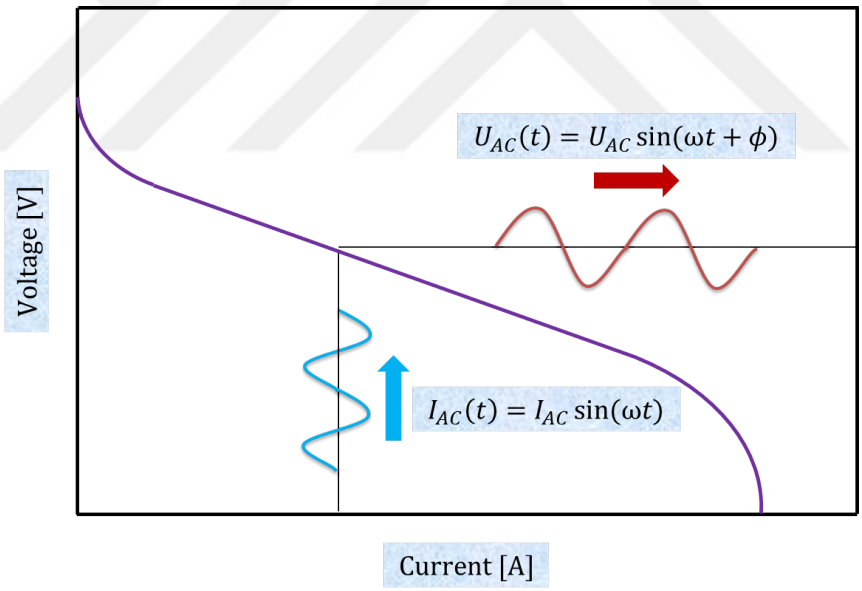

Figure 2.4: *The principle of the EIS carried out at the steady-state shown on a typical I-V curve.*

current is given as

$$I_{AC}(t) = I_0 sin(\omega t) \tag{2.2}$$

where I_{AC} (A) represents the sinusoidal input current at the time t, I_0 (A) the amplitude

of the sinusoidal current, ω (r/s) the radial frequency. The radial frequency is equal to $2\Pi f$ where f $(1/s)$ is the frequency. As illustrated in Fig. 2.4, the response of the excited system is a sinusoidal voltage

$$U_{AC}(t) = U_0 sin(\omega t + \Phi) \tag{2.3}$$

where U_{AC} (V) is the response voltage at the time t, U_0 (V) the amplitude of the sinusoidal voltage signal and Φ $(^\circ)$ the phase.

According to Eq. 2.1, the impedance can be written as

$$Z(\omega) = \frac{U_{AC}(t)}{I_{AC}(t)} = \frac{U_0 sin(\omega t + \Phi)}{I_0 sin(\omega t)} \tag{2.4}$$

Upon applying the Laplace transform, and substituting the trigonometric functions with the complex numbers, the impedance can be expressed in the complex domain as

$$Z(\omega) = |Z(\omega)| \, e^{j\Phi(\omega)} = Z_{re}(\omega) + jZ_{img}(\omega) \tag{2.5}$$

Since the impedance is computed in the complex domain, it is usually visualized in Nyquist plots, in which the negative imaginary part of the impedance is plotted against the real part as depicted in Fig. 2.5. However, impedance data are interpreted via equivalent electrical circuits, wherein basic circuit elements, such as resistors, capacitors and inductors are used to represent the processes proceeding in the system (e.g., SOFC). In fact, Fig. 2.5 presents the impedance spectrum of the Randle's electric circuit drawn in the upper corner of the diagram that is commonly employed in the fuel cell systems. In this circuit, R_{ohm} stands for the ohmic resistance of the cell components, R_{act} the charge transfer resistance giving rise to the activation polarization, C_{dl} (F) the double layer capacitance formed between the electrolyte and electrode. Being function of these parameters, the total impedance Z_{tot} of the Randle's circuit can be written as

$$Z_{tot}(\omega) = R_{ohm} + \frac{R_{act}}{1 + j\omega R_{act} C_{dl}} \tag{2.6}$$

The capacitance and the resistances enabling the computed impedance spectrum to match the experimentally measured spectrum allow us to quantify the ohmic and charge transfer

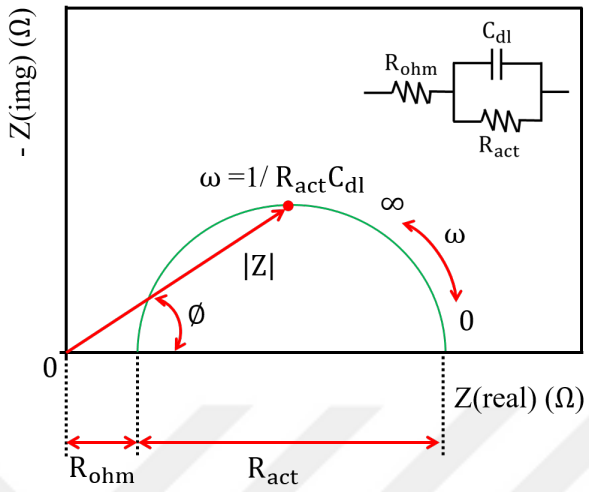

Figure 2.5: *Impedance of the elementary Randle's cell on the Nyquist plot accompanied with the corresponding equivalent electric circuit.*

resistances as well as the double layer capacitance. In the equivalent circuits, each component does not need to represent a physical process happening in the system; some circuit elements can be employed in order solely to match the spectra results.

According to Eq. 2.6, in Fig. 2.5, the intercept of the arc on the X-axis at high frequency divulges the R_{ohm}, whereas the other intercept on the same axis at low frequency shows the summation of the ohmic resistance and charge transfer resistance. Adopting the Randle's

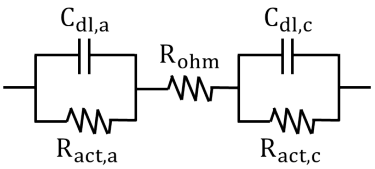

Figure 2.6: *The equivalent circuit commonly used for interpretation of SOFC impedance spectra. Herein, the subscript "a" stands for anode whereas "c" for cathode.*

circuit, the processes in SOFCs are modeled with the equivalent electric circuit given in Fig. 2.6 wherein both of the electrodes (anode and cathode) are regarded within the cell. From this circuit, two arcs are expected to appear on the Nyquist plot. Depending on the

characteristics of the cell and the experimental conditions, the arcs might get unified; as a result, they cannot be distinguished evidently. The total impedance for this circuit can be stated as

$$Z_{tot(\omega)} = \frac{R_{act,a}}{1 + j\omega R_{act,a} C_{dl,a}} + R_{ohm} + \frac{R_{act,c}}{1 + j\omega R_{act,c} C_{dl,c}} \tag{2.7}$$

Based on Eq. 2.7, at frequency approaching the infinity, the impedance spectrum intercepts the X-axis R_{ohm}. At frequency decreasing to zero, the spectrum intercepts again the X-axis disclosing $R_{act,a} + R_{ohm} + R_{act,c}$. Considering these parameters, the regarding processes can be evaluated.

2.5 Longitudinal Measurements of Current, Temperature, and Impedance

Segment currents were measured through three electrical loads (ELZ 175, Keisoku Giken Co. Ltd., Japan), separately connected to the segments through silver wires as depicted in Fig. 2.8. The electrical measurements were carried out by the "four point probe method" to eliminate the peripheral resistances. In addition to the segmentation of the cathode, the uniform voltage distribution along the cell was ensured by the "potentiostatic mode" to prevent the lateral current flow among the segments.

Segment temperatures were sensed on the cathode surfaces by K-type thermocouples, separately. The standard precision for this type of thermocouple is given as $\pm 1\ ^{\circ}C$ [56, 57].

At a constant voltage, segment currents and temperatures were simultaneously recorded by a data logger (midi LOGGER GL800, Graphtec Co. Ltd., Japan) per 200 ms for at least 30 s. The collected current and temperature data populations were averaged and plotted in the regarding figures. The standard deviation for the current measurements is approximately 0.01, whereas it is ca. 0.1 for the temperature measurements.

In order to measure the longitudinal impedance variation, two types of EIS (electrochemical impedance spectroscopies) were employed: an NF 5022 FRA (NF Co. Ltd., Japan) that swept the frequency from 100 kHz to 0.1 Hz, and a Solartron 1280Z FRA (Solartron Analytical) that swept the frequency from 20 kHz to 0.1 Hz. Impedance measurements were

performed by an AC perturbation voltage of 10 mV (peak-peak). For the measurements, the preceding EIS was coupled with the ELZ 175 electrical load of the concerning segment by the four point probe method. However, the Solartron EIS was originally coupled with an internal electrical load, therefore, it was directly connected to the concerning segment.

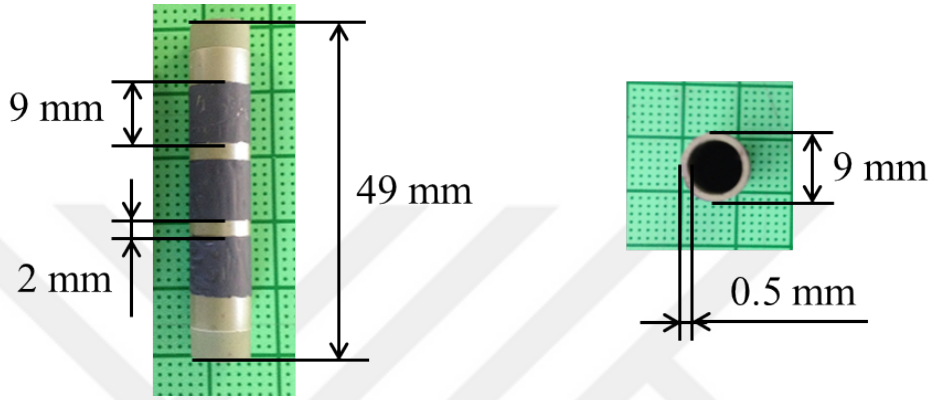

Figure 2.7: *Picture of a segmented mt-SOFC.*

2.6 Operation Conditions

Fig. 2.8 illustrates a schematic of the experimental setup used for the investigations presented in this dissertation. The investigations were conducted at 800 $°C$ sustained by an electric furnace. The segment temperatures were risen to 800 $°C$ prior to the gas supply. A quartz tube placed in the furnace served as an insulator to prevent the heat-loss to the surrounding as well as the air flow domain. The mt-SOFCs were positioned in the quartz tube by a metal fixture. The mt-SOFCs were sealed to the metal fixture by commercial sealants Ceramabond 516 and 552 (Aremco, USA). The fuel inlet tube was preheated, so that the convective cooling in the anode side was avoided. The fuel outlet tube was also heated to prevent the condensation of the product water vapor. Air was supplied into the quartz tube at room temperature, and preheated by the electric furnace prior to reaching the cell. The air temperature at the cell inlet was lower than the furnace temperature for the common convective cooling. Gas flow rates were metered at 25 $°C$ and 100 kPa with mass-flow-controllers (SEC-40, Horiba STEC, Japan) governed by LabVIEW 8.6. The setup was designed to supply the reactant gases in the co- and counter flow configurations.

Additionally, it comprised a humidifier (Chino Co. Ltd., Japan) used for humidifying the fuel stream for the investigations with syngas presented in Chapter 6. In order to reduce NiO to Ni, a dry mixture of $H_2/N_2 = 40/40\ cm^3/min$ (99,99 % pure) was initially fed to the anode for two hours.

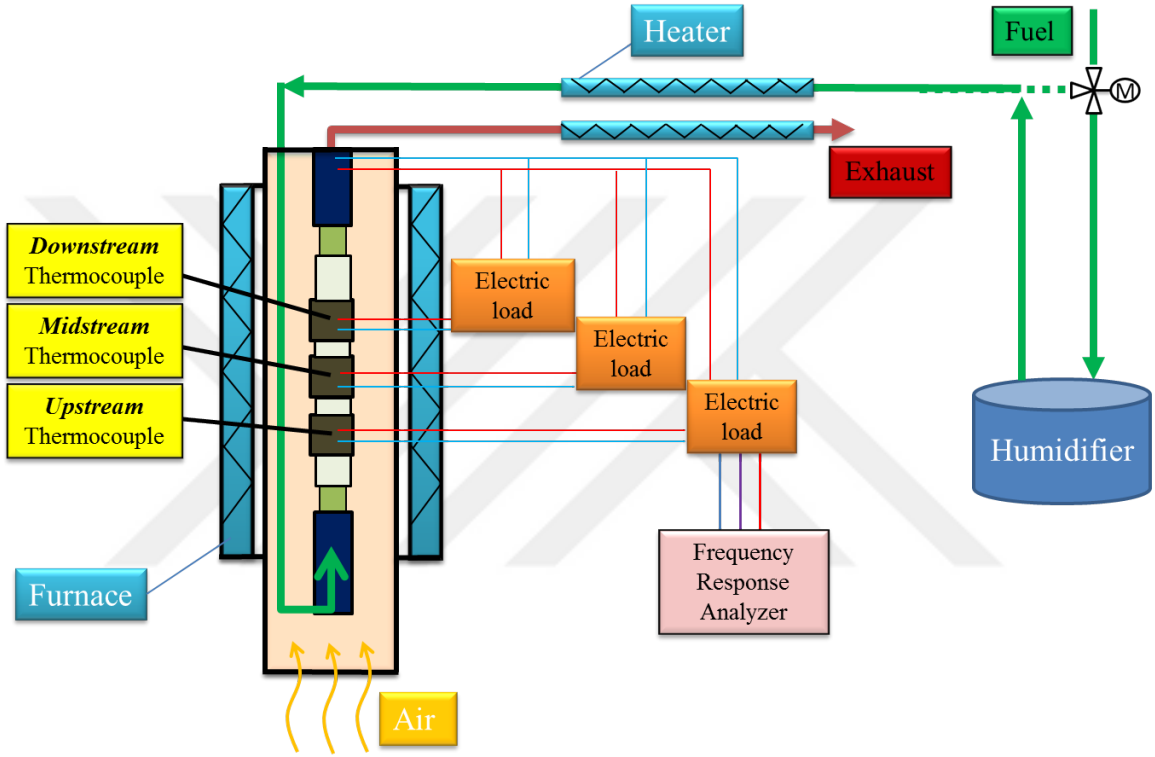

Figure 2.8: *Schematic of the experimental setup designed for the longitudinal characterization of mt-SOFCs.*

Chapter 3

In-situ Diagnosis and Assessment of Longitudinal Current Variations

3.1 Introduction

Regardless of dimension, hydrogen and air supplied to SOFCs as the fuel and oxidant deplete, while the product water-vapor increases from fuel inlet to outlet during electrochemical energy conversion. As a result, Nernst-loss develops along the gas flow field, affecting cell performance in relation with gas supply conditions, such as flow rate and partial pressure, particularly in anode [28, 29, 58].

In general, a tendency is expected in current variations along the flow filed, that is to gradually decrease from fuel inlet to outlet if solely the concentration polarization (including the Nernst-loss) is taken into account. In contrast, current of the downstream segment in a preliminary study was shown to be higher than that of the midstream segment under a particular fuel flow condition [52]. This phenomenon is attributed to the accelerated kinetics of the anodic reactions owing to higher concentration of the product-water in the downstream segment, pointing out that the spatial characterization of SOFCs might provide more insights into the electrochemical reactions.

From the durability point of view, so-called nickel RedOx cycling possibly occurs during the

local fuel starvation. Due to high volumetric expansion/contraction ratio of nickel (1.66), micro-cracks might form in anode [34, 39]. Durability and performance of SOFCs, as the most substantial properties, are hence related to concentrations of the species through current and temperature variations, which can be identified by spatial characterization.

Development of SOFCs requires elimination of the performance and structural degradations stemming from inhomogeneous fuel distribution (assuming sufficient air supply) within the EASA (electrochemical active surface area). Thus, spatial characterization of SOFCs in terms of current variation is of great importance. Although a number of numerical studies focusing on longitudinal current and temperature variations along SOFCs are presented in the literature [17, 59–64], experimental studies have been quite limited. This study is therefore devoted to in-situ diagnosis and evaluation of current variations in anode-supported mt-SOFCs (microtubular-SOFCs) by implementing the segmentation method described in section 2.1. mt-SOFCs were preferred due to the simple tubular form that can readily be segmented for spatial characterization.

3.2 Experimental

A segmented mt-SOFC was manufactured with the identical dimensions (Fig. 2.7), materials and processes given in section 2.2. Spatial current measurements were conducted according to the definition provided in section 2.5. Experimental conditions were established by the setup explained in 2.6. The operation temperature was 800 $^{\circ}C$ throughout the experiments. For reducing NiO to Ni, the procedure described in 2.6 was followed. All the investigations were performed in the co-flow configuration. As Table 3.1 displays, the air flow rate was kept rather high given that the concentration polarization including the Nernst-loss was of main interest; so that H_2/N_2 flow rate was systematically varied.

Table 3.1: *Reactant and oxidant flow rates in cm^3/min given at 25 $^{\circ}C$ and 100 kPa.*

Anode	H_2/N_2	80/40	40/20	40/40	20/20
Cathode	Air	2000	2000	2000	2000

3.3 Results and Discussion

As described in section 2.3, electrochemical performance of fuel cells is essentially evaluated by conventional I-V curves, which display average electrochemical performance of the EASA. In contrast, this study intends to diagnose spatial current variations and to underline the importance of spatial current variations. For the latter intension, conventional I-V curves are presented along with longitudinal I-V curves in the following figures. The conventional I-V curves of the segmented mt-SOFCs were however obtained by summing the longitudinally acquired segment currents according to Eq. 3.1

$$I_{sum} = \sum_{seg} I_{seg} \qquad (A) \tag{3.1}$$

leaning upon the satisfactory agreement achieved between the conventional I-V curves directly acquired from a full mt-SOFC and indirectly obtained from spatial current measurements shown in Fig. 3.1.

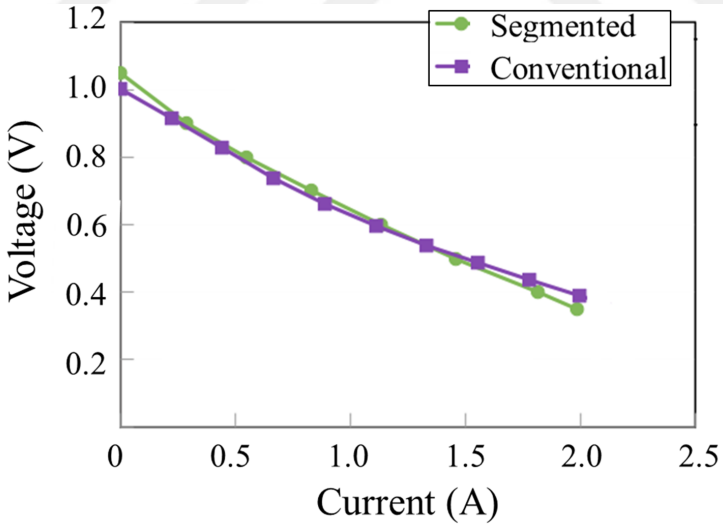

Figure 3.1: *Comparison of the I-V curves drawn by the currents summed from the segments and conventionally measured. H_2/N_2=40/40 and O_2/N_2 (air)=2000 cm^3/min, and T_{fur}=800 °C.*

3.3.1 Longitudinal Current Variations

Current variations along the cell were characterized through measuring the current of each segment in the potentiostatic mode. The evaluation of the experimental data is carried out over the graphs where the I-V curves are plotted for the corresponding segments for various fuel flow rates, respectively. The conventional I-V curves accompanied with the estimated total fuel stoichiometry are presented in the regarding graphs, too.

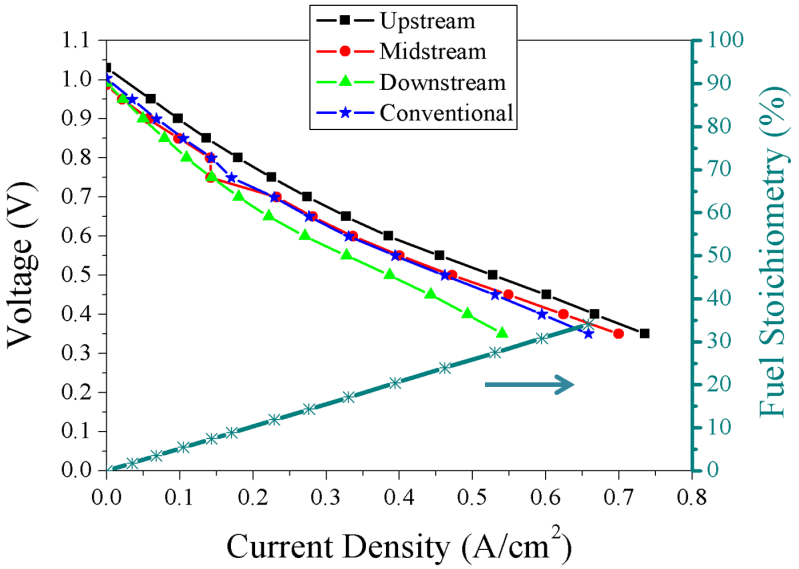

Figure 3.2: *Longitudinal current variations in the cell at H_2/N_2=80/40 and O_2/N_2 (air)=2000 cm^3/min, and T_{fur}=800 °C.*

Fig. 3.2 presents the current variations among the segments at a high fuel flow condition. The overall current density represented by the conventional I-V curve attains 0.65 A/cm^2 at 0.35 V where the fuel stoichiometry remains at 34%. Even though the current variations among the segments are not significant at high cell voltages, they become considerable at lower voltages. In this voltage range, no indication of the mass transport limitation exists. In a wide range of the voltage, the conventional I-V curve overlaps with the midstream I-V curve, which represents the mean current density of the EASA.

In Fig. 3.3, the difference among the segment currents becomes prominent with the de-

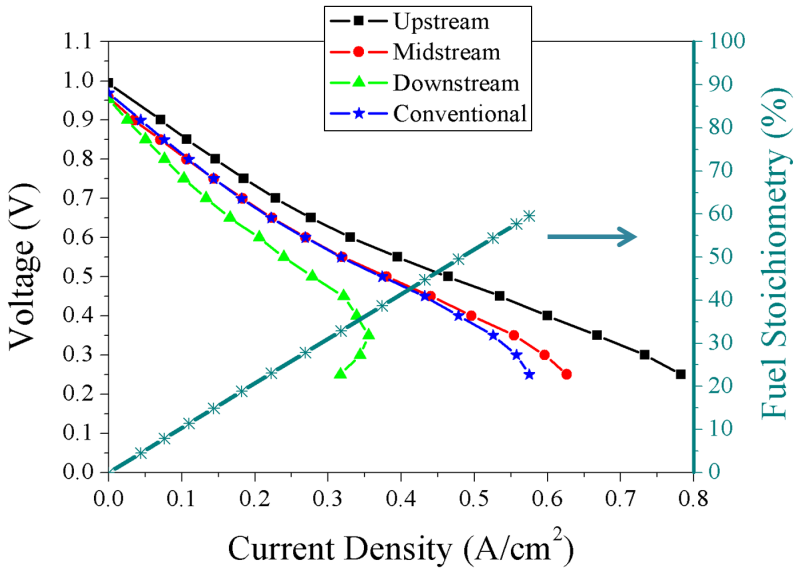

Figure 3.3: *Longitudinal current variations in the cell at H_2/N_2=40/20 and O_2/N_2 (air)=2000 cm^3/min, and T_{fur}=800 °C.*

creasing voltage. This variation is ascribed to the concentration polarization comprising the Nernst-loss. Accordingly, typical concave characteristic initiates firstly at 0.4 V and the fuel stoichiometry of 50% in the downstream, revealing the fuel starvation. Similar to the previous case, the conventional curve overlaps with the midstream I-V curve down to 0.4 V, but it distinguishes from the other segments remarkably. The concave characteristic of the conventional curve notably differs from that of the downstream segment in a way that the downstream current concurrently diminishes with the decreasing cell voltage, while the preceding segments generate higher currents with the increasing fuel stoichiometry.

For the case where the fuel dilution is enhanced with the higher flow of nitrogen, longitudinal current variations are presented in Fig. 3.4. Herein, the general characteristics of the segments are fairly analogous to the ones noted under the former conditions. However, the remarkable fuel starvation initiates at 0.4 V in the downstream at a higher fuel stoichiometry of 51%. The overlap between the conventional I-V curve and the midstream I-V curve down to 0.4 V fairly resembles the preceding case.

In contrast to the previous cases, longitudinal current variations were measured for a

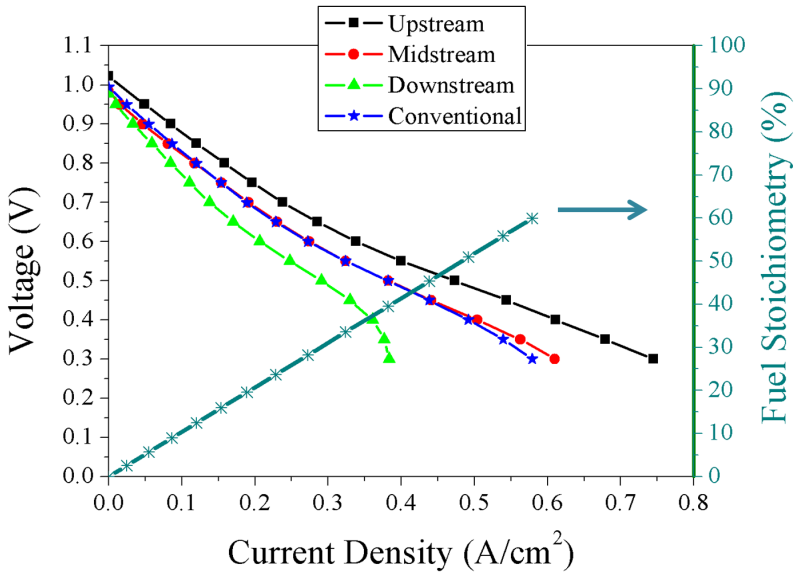

Figure 3.4: *Longitudinal current variations in the cell at H_2/N_2=40/40 and O_2/N_2 (air)=2000 cm^3/min, and T_{fur}=800 °C.*

lower hydrogen flow rate; the regarding I-V curves were drawn in Fig. 3.5. Despite of the analogous characteristics of the I-V curves, at any voltage the current variations are more significant than those in the preceding circumstances. The severe mass transport limitation initiates at 0.6 V at a lower fuel stoichiometry of 40%, implying the ineffective use of the downstream segment. With the declining cell voltage, even if the midstream and downstream segments exhibit the mass transport limitation, the situation is severer in the downstream, restricting the voltage range. On the other hand, the upstream segment continues to increase its current further leading to the higher fuel stoichiometry. Taking account of the significant fuel starvation in the downstream, the re-oxidation of nickel catalyst particles in the anode is likely to occur. The average of the segment currents giving the conventional curve overlaps with the midstream I-V curve. This finding shows that the conventional curve is the representative of the mean current of the EASA [65].

The comparison of the longitudinal current variations previously discussed for various cell voltage and flow rates is presented in Fig. 3.6. The severity of the longitudinal current variation is clearly shown by the steep slopes of the curves, especially at low cell voltages.

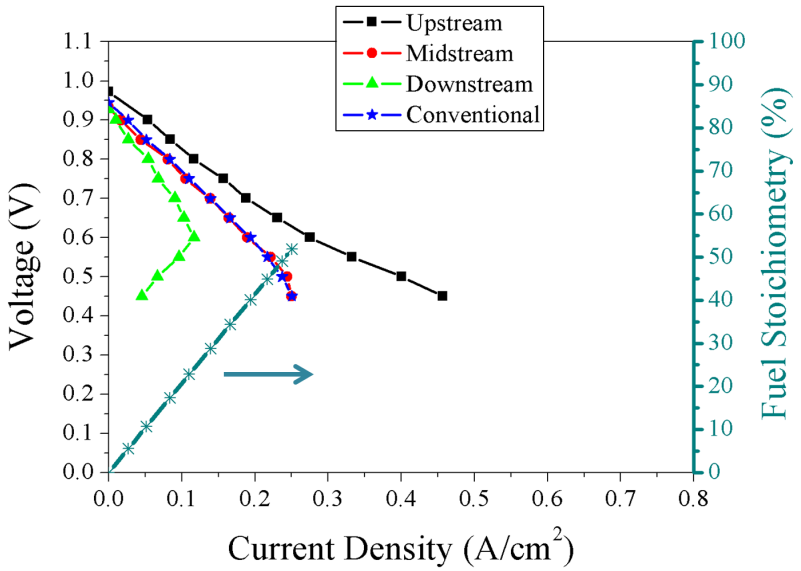

Figure 3.5: *Longitudinal current variations in the cell at H_2/N_2=20/20 and O_2/N_2 (air)=2000 cm^3/min, and T_{fur}=800 °C.*

As expected, the cell performance is the highest for H_2/N_2 = 80/40 cm^3/min condition. On the other hand, the overall performance improvement of the cell as a result of higher nitrogen flow at the identical hydrogen flow rate is evident. At 0.45 and 0.5 V, the slight impact of the higher nitrogen flow rate on the homogeneity of the longitudinal current distribution is recorded. Based on the fairly steep slope of the current distribution curve for H_2/N_2 = 20/20 cm^3/min, the re-oxidation of nickel catalysts is anticipated.

3.3.2 Performance Degradation Analysis

The current variations among the segments due to the Nernst-loss included in the concentration polarization were analyzed for various fuel flow conditions in the previous section. From the practical point of view, the impact of the longitudinal current variations on the cell performance depending on the fuel flow rate is of great importance. In fact, the inherent electrochemical capacity of the cell can be computed as threefold of the highest current density generated by one of the segments at any voltage, as given with Eqs. 3.2 and 3.3. Based on this approach, the performance degradation of the cell can be assessed over the

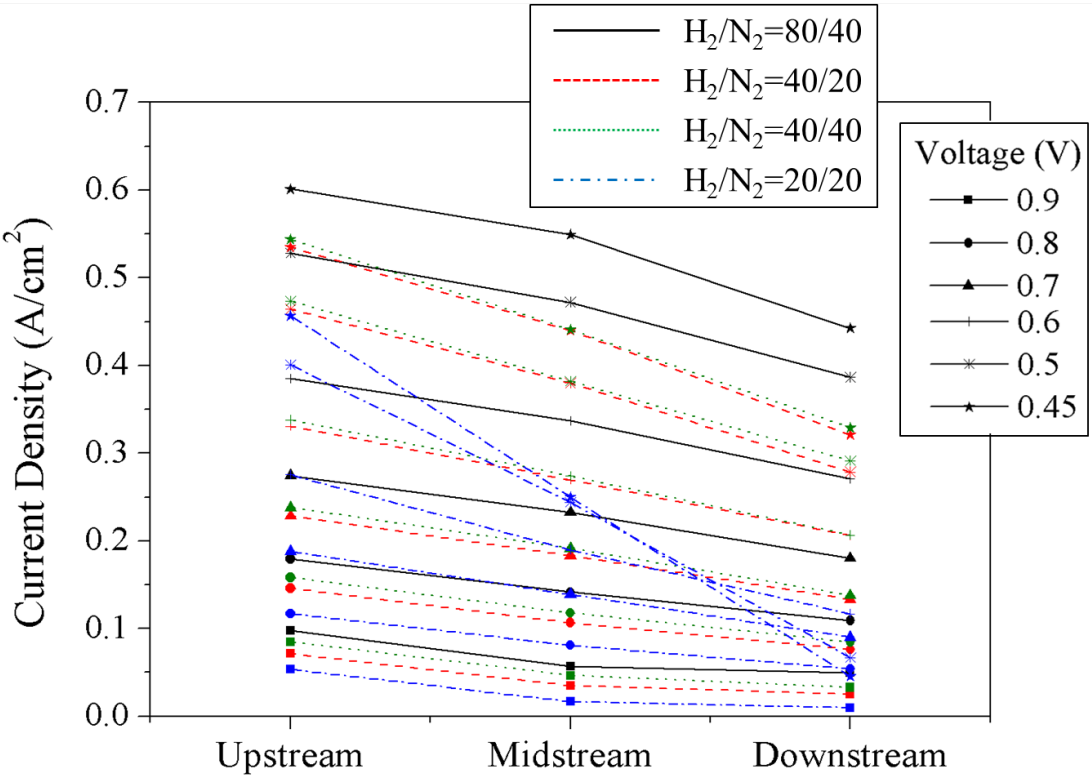

Figure 3.6: *Current distributions along the cell for various cell voltages and fuel flow rates at T_{fur}=800 °C and O_2/N_2 (air)=2000 cm^3/min.*

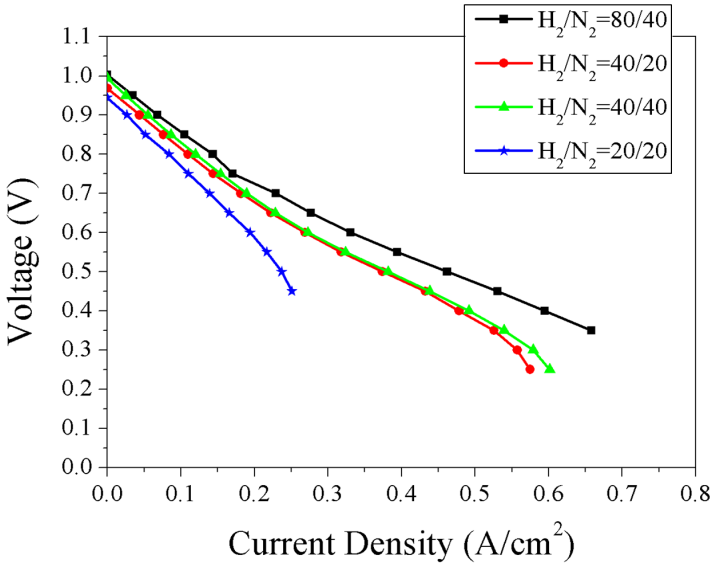

Figure 3.7: *Comparison of the conventional I-V curves of the cell for various fuel flow rates.*

conventional and capacity I-V curves drawn for various fuel flow rates in Figs. 3.7 and 3.8.

$$Max(I_{upstream}, I_{midstream}, I_{downstream}) = I_{upstream} \tag{3.2}$$

$$I_{cap} = 3 * (I_{upstream}) \tag{3.3}$$

Comparison of the conventional and capacity I-V curves in Figs. 3.7 and 3.8 reveals the performance degradation in the cell regardless of the fuel flow condition. Based on the numerical calculations, 10.5%, 18.8%, 19.3%, 29.6% performance degradation at 0.6 V is estimated for $H_2/N_2 = 80/40$, $H_2/N_2 = 40/20$, $H_2/N_2 = 40/40$ and $H_2/N_2 = 20/20$ cm^3/min, respectively. As a result of the fuel dilution with $H_2/N_2 = 40/40$ cm^3/min, the maximum fuel stoichiometry increases by 2.7%. It is important to note that the I-V curves drawn for the cell capacity for $H_2/N_2 = 20/20$ cm^3/min overlap with the conventional I-V curves of $H_2/N_2 = 40/40$ cm^3/min and $H_2/N_2 = 40/20$ cm^3/min, implying that if the capacity of the cell would have been fully utilized, the energy conversion efficiency would double.

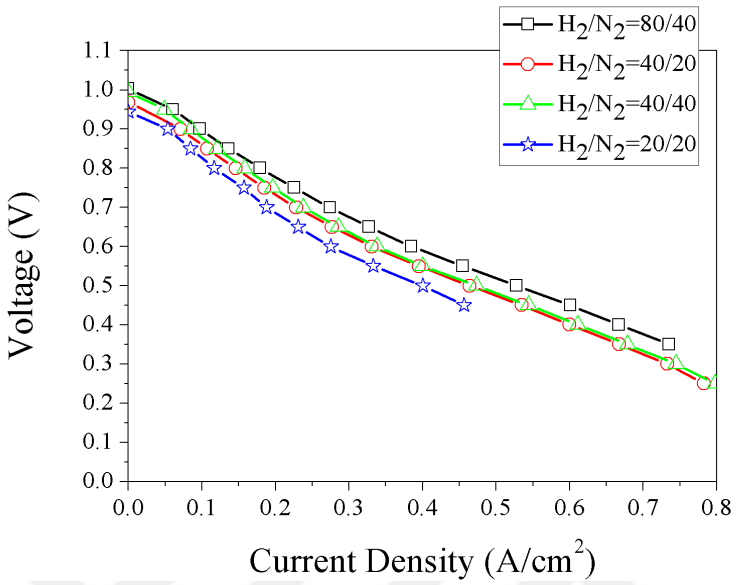

Figure 3.8: *Comparison of the capacity I-V curves of the cell for various fuel flow rates.*

3.4 Conclusions

Current variations along an anode-supported microtubular-SOFC were experimentally measured by the segmentation method for various cell voltages and fuel flow conditions. Relying on the negligible deviation between the performance of the whole and the segmented cell, the conventional I-V curves, as the summation of the segment currents, were presented along with the I-V curves of the segments. Current distributions for various cell voltages and flow rates were shown along the cell. From the practical point of view, an analysis of the performance degradation due to the mass transport limitation was carried out on the basis of the measured and estimated electrical quantities. Based on the evaluations, the following conclusions are drawn:

I) The segmentation is a useful method to in-situ reveal the current variations along mt-SOFCs,

II) Due to the remarkable current variations, notable temperature variations are anticipated,

III) The performance characteristics of the segments differ considerably. The downstream

current concurrently decreases with the declining voltage, implying the partial fuel starvation, whereas the currents of the other segments increase further,

IV) The partial fuel starvation in the downstream is not clearly presented by the conventional I-V curve, which overlaps with the midstream I-V curve regardless of the fuel flow conditions. Given that the fuel starvation causes nickel re-oxidation, the longitudinal characterization of the microtubular-SOFCs is highly appreciated,

V) Higher nitrogen flow rate improves the cell performance,

VI) The Nernst-loss included in the concentration polarization results in a remarkable performance degradation, which enhances at lower fuel flow rates.

Chapter 4

Elaboration of Processes Involving in Temperature Variations

4.1 Introduction

With a consensus among the researchers, the thermal stresses are accounted for the mechanical failure of SOFCs [1,32,33]. To resist the thermal stresses at the maximum achievable electrochemical performance, SOFCs are designed in various forms, for instance flat-tubular, tubular, and planar, etc.

Table 4.1: *The CTE of the cell components* [1]

Material	CTE $[K^{-1}]$
Ni/YSZ	13×10^{-6}
8YSZ	10×10^{-6}
LSM	11×10^{-6}

An SOFC fundamentally consist of three main components, anode, electrolyte, and cathode. The cell fabrication requires sequential heat-treatment processes at high temperature

(1000-1450 $°C$) for each component; thus, induction of the residual stresses to the cell is inevitable [1,32,37]. Because the components are made of distinct ceramic-based materials, they possess diverse CTE (coefficients of thermal expansion), as given in Table 4.1.

Basically, the CTE and temperature are the main parameters determining the thermal strain of materials according to

$$\varepsilon_{th} = \alpha_v(T - T_{ref}) \tag{4.1}$$

where ε_{th} is the thermal strain, α_v $(1/K)$ the CTE, T (K) the temperature, and T_{ref} (K) the reference (stress-free) temperature. According to Eq. 4.1, even a small difference among the CTEs of the components might result in thermal stresses due to the high operation temperature of mt-SOFCs [1,32,35–37]. Therefore, the cell components are required to be made of materials possessing similar CTEs.

Even if the materials with similar CTEs were selected, longitudinal temperature variations over the cell surface might induce thermal stresses [1, 32, 33, 35–37, 66, 67]. While a cell is operating with hydrogen and air (excess amount), concentrations (partial pressure) of the reactant and product gases in the anode differentiate along the flow field, resulting in the Nernst-loss due to the electrochemical HOR (hydrogen oxidation reaction) [28, 29, 58]. The Nernst-loss eventually gives rise to longitudinal current and temperature variations, as it affects the reversible and irreversible losses, such as the activation and concentration polarizations [52, 65, 68, 69]. In addition, as a common practice, air is supplied at high velocities (excess amounts) to the cathode for removing the waste heat via the convective cooling that intuitively influences the longitudinal temperature variations [32, 36, 70–72]. Thereby, in-situ investigation of the processes involving in the longitudinal temperature variations has been interesting to alleviate the variations.

Experimental difficulties in measuring the longitudinal temperature and current variations over the cell surface due mainly to the high operation temperature of SOFCs have been leading researchers to focus on numerical tools [66, 67]. Researchers have been developing thermo-electrochemical models by which they have been exploring the longitudinal variations of temperature, current, and concentration of species. They have been transferring the temperature variations to thermo-mechanical models for predicting the induced

thermal stresses [1,32,35–38,72]. Although the thermo-electrochemical models are usually validated with conventional I-V (current-voltage) curves, they are hardly validated in terms of the in-situ measured temperature variations. Given that temperature exerts remarkable impact on various processes involving the electrochemical energy conversion in SOFCs, for instance, reaction kinetics, ionic conductivity of electrolyte, etc., characterization of the temperature variations is of great importance to evaluate the reliability of numerical tools for computing spatial properties.

For in-situ measuring the longitudinal temperature variations, there have been valuable attempts indeed. Morel et al. predicted the temperature variations over a planar SOFC relying on the relation between ionic conductivity of electrolyte and temperature. Razbani et al. reported the temperature variations measured by thermocouples positioned in the gas stream of a planar SOFC [33]. Santarelli et al. measured the local temperatures at the inlet, middle and outlet of a 1.5 m long tubular cell bundle; unfortunately, they did not provide sufficient information on the positions of the thermocouples [73].

In this study, the processes involving in the temperature variations with their respective contributions are explored in mt-SOFCs (microtubular-SOFCs). Regarding as the main processes, the study focuses on the current variations and the convective heat transfer due to the fact that air is usually fed at excess rates for the cooling purpose in the practical systems. Thereby, the variations are analyzed with the co- and counter-flow configurations. The analyses are conducted based on the spatial properties in-situ measured through the segmentation method. In addition, the influence of the temperature variations on the current and concentration variations is investigated via analyzing spatial impedance variations.

4.2 Experimental

A segmented mt-SOFC was manufactured with the identical dimensions (Fig. 2.7), materials and processes given in section 2.2. Spatial current, temperature, and impedance measurements were conducted according to the definition provided in section 2.5. Experimental conditions were established by the setup explained in 2.6, which was however modified as in Fig. 4.1 to set the direction of the gas streams in the co- and counter-flow

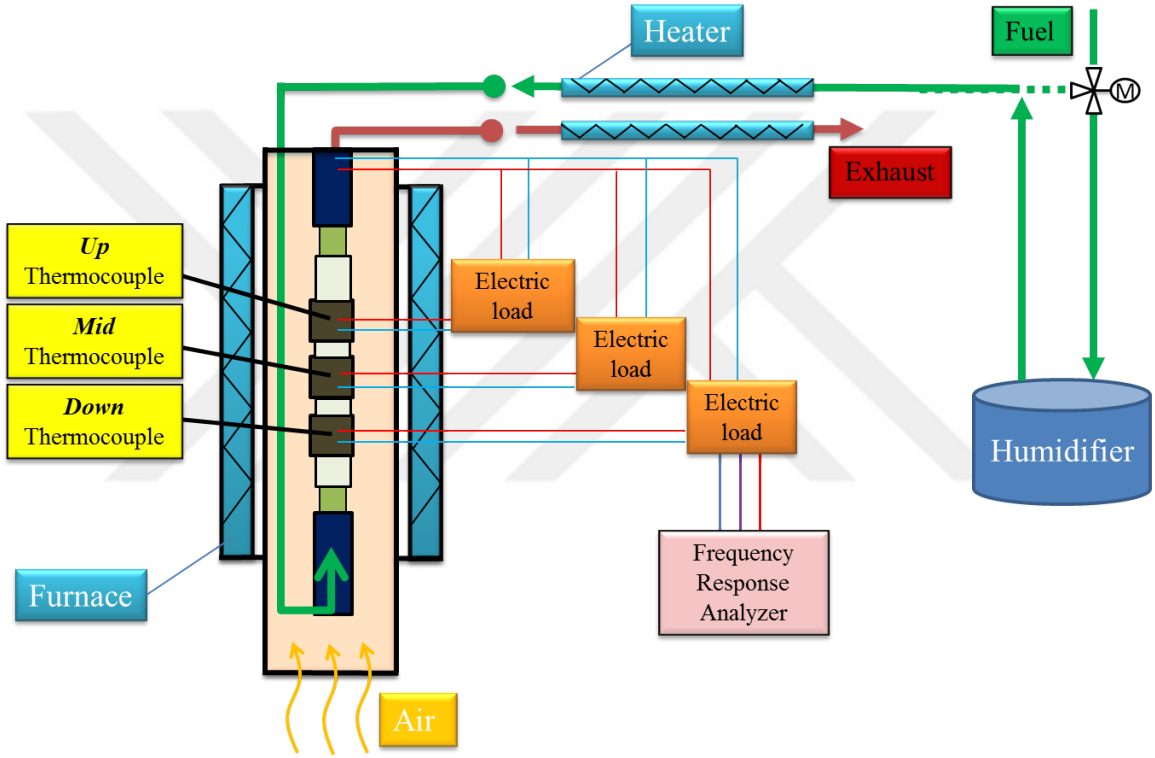

Figure 4.1: *Schematic of the modified experimental setup for the longitudinal characterization of mt-SOFCs in the co- and counter-flow configurations, where the impedance spectroscopy is also attached.*

configurations. To be consistent throughout the analyses of the variations in the co- and counter-flow configurations, the segments are called as "up-, mid-, and down-segments", referring to their positions on the cell. The operation temperature was 800 $°C$ throughout the experiments, whereas the air inlet temperature was ca. 775 $°C$. For reducing NiO to Ni, the procedure described in 2.6 was followed.

4.3 Results and Discussion

The segment temperatures are plotted as "temperature rise (ΔT_{seg})" that is the difference between the segment temperature (T_{seg}) and the furnace temperature ($T_{fur} = 800\ °C$), as given in Eq. 4.2.

$$\Delta T_{seg} = T_{seg} - T_{fur} \tag{4.2}$$

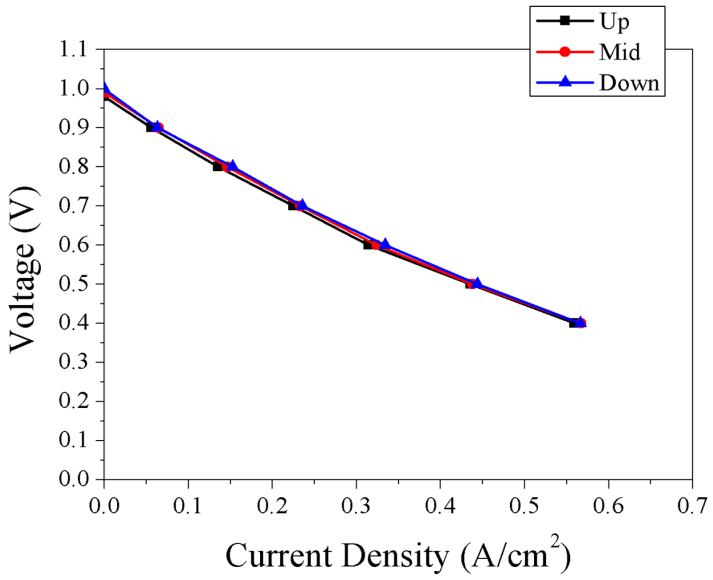

Figure 4.2: *I-V curves of the segments with the co-flow configuration for H_2/N_2=80/120 and O_2/N_2 (air)=2000 cm^3/min.*

4.3.1 Prevailing Processes on Longitudinal Temperature Variations

Since the reversible and irreversible losses are effective on the longitudinal temperature variations [65], and these losses are dependent upon current, elimination of the current variations is essential to disclose the other involving processes. Therefore, the analysis is beginning at a high fuel flow rate to keep the fuel stoichiometry low (λ_{H_2} = 29% at 0.4 V). Under these conditions with the co-flow configuration, the measured segment I-V curves are depicted in Fig. 4.2. In this figure, the I-V curves almost overlap, i.e., the current variations are quite small among the segments through the voltage range. Thereby, insignificant temperature variations are expected.

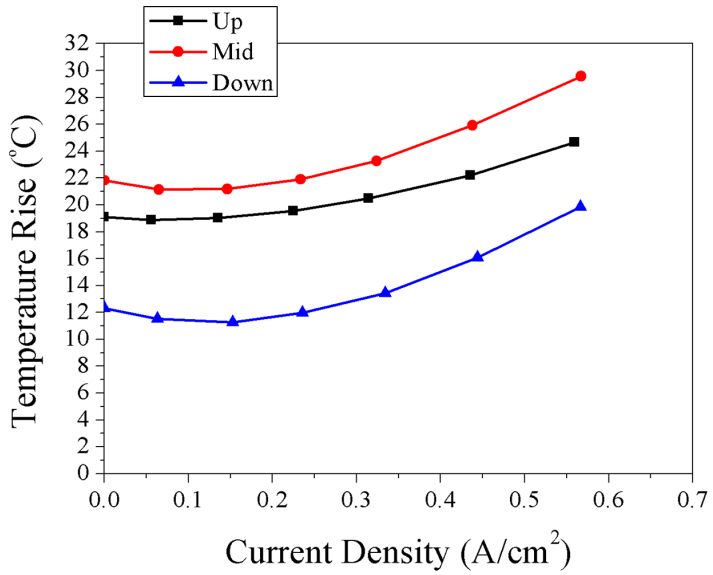

Figure 4.3: *I-T curves of the segments with the co-flow configuration for H_2/N_2=80/120 and O_2/N_2 (air)=2000 cm^3/min.*

Fig. 4.3 provides sufficient evidence to justify the stated expectation for the longitudinal temperature variations with the co-flow configuration. In this figure, all the segment temperatures are higher than the furnace temperature at OCV (open circuit voltage). The temperature rise at OCV stems from the combustion of the leaking hydrogen that mainly

occurs around the sealant (Aremco, Ceramabond 552) among the cell and metal holders. The extent of the hydrogen leakage can be estimated via analyzing the heat balance within the system. For this analysis, the initial state of the system, right after the hydrogen and air supply was regarded; and the segment temperatures were in-situ measured as plotted in Fig. 4.4.

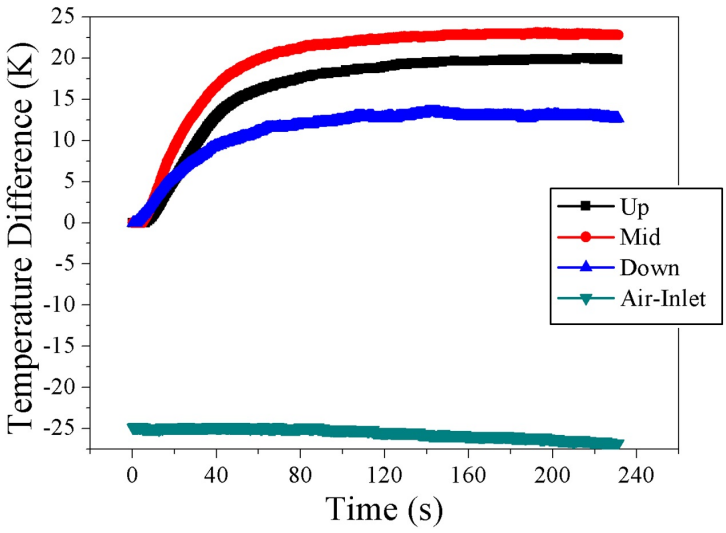

Figure 4.4: *Temperature difference normalized to the furnace temperature (800 °C) for the segments and air right after the supply of hydrogen and air with the co-flow configuration at H_2/N_2=40/40 and O_2/N_2 (air)=2000 cm^3/min.*

In the transition state, the total heat production rate $\Delta\dot{H}_{HOR}$ (kW) is released via the combustion of the leaking hydrogen $\Delta\dot{n}_{H_2}$ (mol/s)

$$\Delta\dot{H}_{HOR} = \Delta h_{HOR}\Delta\dot{n}_{H_2} \tag{4.3}$$

$$\Delta\dot{n}_{H_2} = \dot{n}_{H_2,in} - \dot{n}_{H_2,out} = \dot{n}_{H_2,leak} \tag{4.4}$$

While Q_{cell} (kJ) is absorbed by the cell, Q_{conv} (kW) is simultaneously removed by the air flow via the convective heat transfer on the cathode surface. Owing to the relatively low thermal conductivity of the sealant ($k = 30\ W/mK$), the conductive heat transfer to the

adjacent piping is neglected. Since the segment surfaces were coated with silver-paste that resembles the gray body (poor radiative properties), the radiative heat transfer is ignored, too [74]. In this regard, the heat balance within the system can be formulated as

$$\int_0^t \Delta \dot{H}_{HOR} dt = Q_{cell} + \int_0^t Q_{conv} dt \tag{4.5}$$

Herein the time interval for the temperature rise in the segments $t = 140\ s$ from Fig. 4.4. When the Q_{cell} and Q_{conv} are calculated, $\dot{n}_{H_2,leak}\ (mol/s)$ can be found.

Due to the varying thermo-physical property of the cell components

$$Q_{cell} = Q_a + Q_{el} + Q_c \tag{4.6}$$

where the subscript "a" stands for the anode, "el" for the electrolyte, and "c" for the cathode. For $i \in (a, el, c)$

$$Q_i = \rho_i V_i C_{p,i} (T_t - T_0) \tag{4.7}$$

where $V\ (m^3)$ represents the solid volume of the cell. The density ρ and the heat adsorption coefficient C_p of the cell components are given as 3310, 5160, and 3030 (kg/m^3); and 450,470, and 430 (J/kgK) for Ni/YSZ (anode), 8YSZ (electrolyte), and LSM/YSZ (cathode), respectively [71, 75].

According to the Newton's law

$$Q_{conv} = hA(T_{cell} - T_\infty) \tag{4.8}$$

where $A\ (m^2)$ is the surface area over which the convection takes place and the heat transfer coefficient $h = 2.8\ W/m^2K$ calculated from the Nusselt number Nu

$$Nu = hD_h/k = 10.2 \tag{4.9}$$

which is accepted due to the rather low Reynolds number ($Re = 6.98 << 2300$ (laminar flow)) [76]. Herein, $D_h\ (m)$ is the hydraulic diameter and $k\ (W/mK)$ the thermal conductivity of air. $T_\infty = 775\ ^\circ C$ is taken from Fig. 4.4. Considering the arithmetic average temperature of the segments at $t = 140\ s$ as

$$T_{cell} = (T_{seg,up} + T_{seg,mid} + T_{seg,down})/3 \tag{4.10}$$

The fuel leakage rate

$$\frac{\dot{n}_{H_2,leak}}{\dot{n}_{H_2,in}} 100 = 0.77 \tag{4.11}$$

Such amount of leakage rate is acceptable considering the operation at high temperature. In

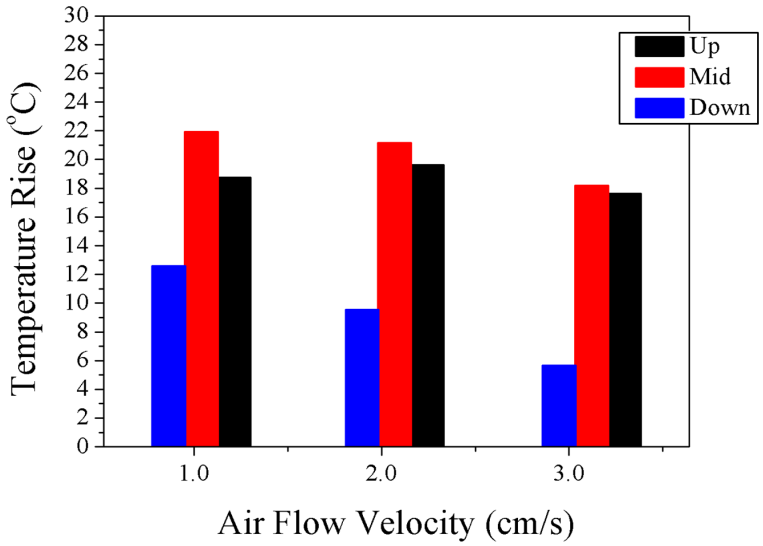

Figure 4.5: *Impact of the convective heat transfer on the segment temperatures at 0.7 V with the co-flow configuration for H_2/N_2=80/120 and O_2/N_2 (air)=2000 cm^3/min, which is equivalent to 2.0 cm/s.*

Fig. 4.3, the slight temperature drops with the rising segment currents are associated with the reduction in the fuel leakage rate owing to the increasing consumption of hydrogen by the electrochemical reaction. Though the up- and down-segments are nearest to the main combustion areas (sealant), at OCV the down-segment exhibits the smallest temperature, whereas the mid- and up-segments' temperatures are similar and rather high. Since the cell is positioned in the geometrical center of the furnace, and the segment temperatures were set approximately the same prior to the gas supply, such variations are not expected from the radiative and conductive heat transfers upon supplying the gases. Thereby, this temperature distribution profile is ascribed to the convective heat transfer. In fact, this argument is verified by Fig. 4.5, wherein the temperature of the down-segment at 0.7 V significantly drops with the rising air flow velocity. Note that, in this velocity domain no

mass transport limitation exists in the cathode side.

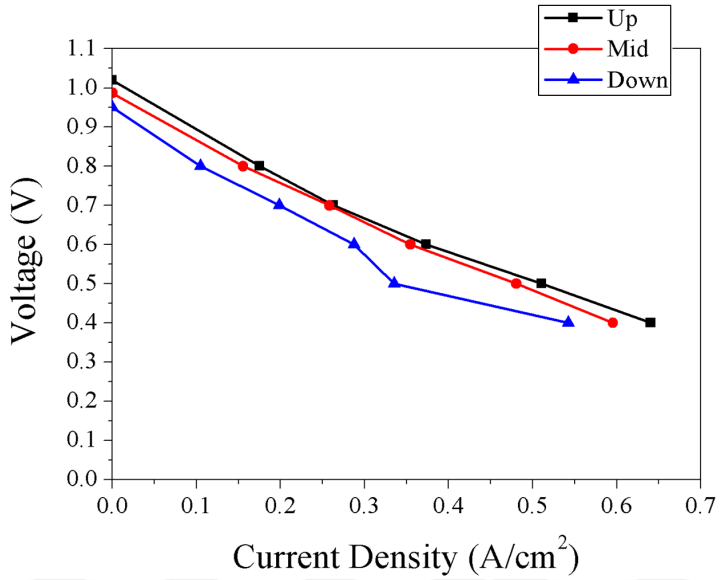

Figure 4.6: *I-V curves of the segments with the counter-flow configuration for H_2/N_2=80/120 and O_2/N_2 (air)=2000 cm^3/min.*

As Fig. 4.1 displays, the convective heat transfer is occurring in two distinct interfaces: firstly, between the quartz tube and the air stream; secondly, between the air stream and cell. The air is initially heated about 775 $°C$ (Fig. 4.4) by the quartz tube which is in direct contact with the furnace. This heated air proceeds along the cell; and cools the cell down. Although the flow velocity range shown in Fig. 4.5 is quite small, forming laminar flow (Re = 6.98 at 2.0 cm/s), the thermal boundary layer is not developed within the entrance region of the cell. This means that the flow in the entrance regions is not laminar yet. As a result, the local Nusselt number/heat transfer coefficient within the entrance region of the cell is higher than what was assumed while estimating the hydrogen leakage rate [67, 74] and it is a function of the flow velocity. The entrance length L_h (m) is given as [74]

$$L_h \approxeq 0.05 Re D_h \tag{4.12}$$

From Eq. 4.12, L_h = 12.9 mm can be calculated, that is slightly longer than the length of the down-segment (9 mm). The down-segment's temperature is thus highly affected by

the air flow velocity. In this respect, the hydrogen leakage is anticipated to be somewhat higher than 0.77%. However, the flow is fully developed around the mid-segment, so that the mid- and up-segments exhibit similar temperatures. As a result, the temperature gradient becomes significant along L_h. Assuming that temperature rises from the air inlet along the L_h linearly, and $T_{seg,down} = 12\ K$ represents the local temperature at $x = 4.5\ mm$, the longitudinal temperature gradient $\partial T/\partial x = 4000\ K/m$. According to Chiang et al., the temperature gradient must be below 2666 K/m to inhibit the crack formation [38]. Besides, 4000 K/m is relatively higher than what is estimated to be small by Fischer et al. [32]. Regarding these references, the temperature gradient developing in the entrance length is likely to pose crack formation.

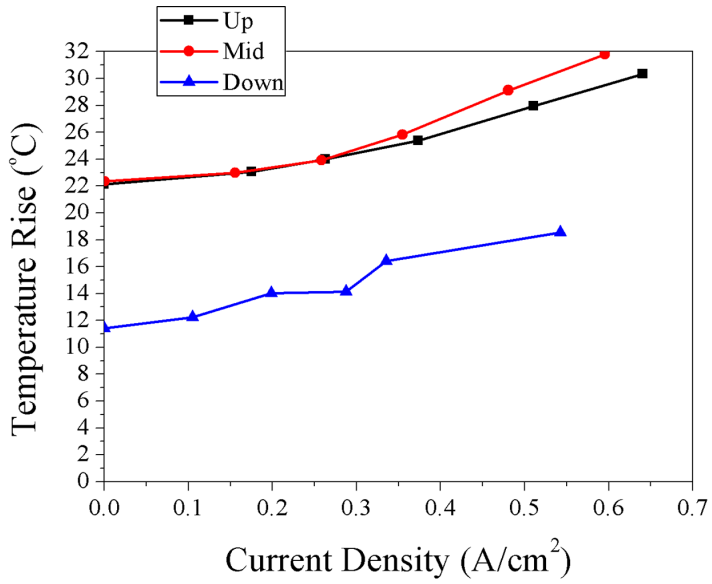

Figure 4.7: *I-T curves of the segments with the counter-flow configuration for H_2/N_2=80/120 and O_2/N_2 (air)=2000 cm^3/min.*

Since temperature is effective on the involving physical and electrochemical processes (ionic conductivity, kinetic, etc.), such a longitudinal temperature distribution profile points out the limitation in the down-segment, that probably reduces the local fuel stoichiometry and thus lets the mid- and up-segments to produce larger currents owing to their higher temperatures. Ultimately, the current variations become quite small as shown in Fig.

4.2. This hypothesis can be justified by switching the gas flow configurations to counter-flow (reversing the fuel flow direction), so that the up-segment would receive the highest hydrogen concentration with similar longitudinal temperature distribution profile by the prevailing impact of the convective heat transfer.

Upon switching the gas flow configuration to counter-flow, I-V curves depicted in Fig. 4.6 were measured. In contrast to the I-V curves measured with the co-flow configuration, current variations among the segments are observed, despite the low fuel stoichiometry ($\lambda_{H_2} = 31\%$ at $0.4\ V$). The mid- and up- segments produce higher currents than the down-segment through the voltage range. In terms of the flow configuration, at $0.4\ V$, the counter-flow configuration enhances the mid- and up-segments' currents, while the down-segment's current remains nearly the same. As a result, the fuel stoichiometry (total current output) at $0.4\ V$ with counter-flow is slightly higher than that observed with co-flow.

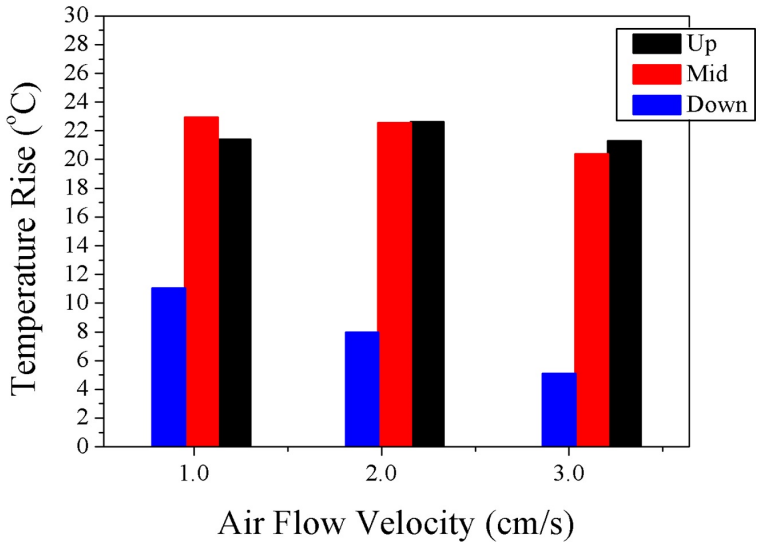

Figure 4.8: *Impact of the convective heat transfer on the segment temperatures at 0.7 V with the counter-flow configuration for H_2/N_2=80/120 and O_2/N_2 (air)=2000 cm^3/min, which is equivalent to 2.0 cm/s.*

In fact, the longitudinal current variation profile in Fig. 4.6 resembles the longitudinal

temperature variation profile shown in Fig. 4.7, which is acquired with the counter-flow configuration. This resemblance justifies the respective hypothesis that the temperature variations affect the current variations. In Fig. 4.7, the development of such a temperature distribution profile at OCV again confirms the prevailing impact of the convective heat transfer. This prevailing impact can be clearly seen in Fig. 4.8 as well. Alike the co-flow case (Fig. 4.3), herein, the segment temperatures are higher than the furnace temperature at OCV, that stems from the combustion of the leaking hydrogen. The exchange of the fuel flow direction influences the leakage rate somewhat.

As shown in the previous figures, the mid- and up-segments exhibit similar temperatures owing to the convective heat transfer. While analyzing the effect of the longitudinal temperature variations on the current variations in the next subsection, only the up-segment's temperature will thus be considered for the sake of simplicity.

4.3.2 Influence of Temperature Variations on Ohmic Resistance Along Cell

As mentioned previously, assuming that the main contribution to the ohmic resistance of an SOFC comes from the ionic resistance, Morel et al. proposed a method for predicting the temperature variations over a cell comprised a rather thick electrolyte (500 μm) by using the relationship between the ionic conductivity and temperature given as

$$\sigma_{el} = \frac{A_0}{T} exp\left(-\frac{E_{act}}{k_B T}\right) \tag{4.13}$$

where σ_{el} (S/m) is the ionic conductivity, A_0 the pre-exponential factor, E_{act} $(J/atom)$ the activation energy for the ionic conduction, k_B (J/K) the Boltzman constant, and T (K) temperature. In fact, the thickness of the electrolyte in this study is relatively smaller ($\approx$ 20 μm), and approximately constant along the cell. However, the significant temperature variation among the down- and up-segments depicted in Figs. 4.5 and 4.8 causes notable ohmic resistance difference between them. Table 4.2 presents the resistances measured by impedance spectroscopy for the co- and counter-flow configurations.

At 1.0 cm/s, the ohmic resistance in the down-segment is 16% higher than that in the up-segment with both flow configurations. As the air flow velocity increases, the down-

Table 4.2: *Impact of the temperature variations on the ohmic resistance along the cell at 0.7 V for H_2/N_2=80/120 cm^3/min. Note that 2000 cm^3/min is equivalent to 2.0 cm/s.*

Air Flow Velocity (cm/s)	Ohmic Resistance (Ω)			
	Co-Flow		Counter-Flow	
	Up-Segment	Down-Segment	Up-Segment	Down-Segment
1.0	0.127	0.145	0.125	0.145
2.0	0.127	0.152	0.126	0.149
3.0	0.129	0.157	0.128	0.154

segment's temperature drops (Figs. 4.5 and 4.8), which results in higher local ohmic resistance. In contrast, the temperature of the up-segment is weakly dependent on the air flow velocity; thus, the ohmic resistance of this segment changes slightly. Consequently, the resistance difference along the cell rises. This implies that at a constant cell voltage, the down-segment suffers from both ohmic and kinetic limitations that influence both the current and temperature variations.

4.3.3 Longitudinal Current Variations Arising from Nernst-loss Coupled with Temperature Variations

While analyzing the impact of the convective heat transfer on the longitudinal temperature variations in the preceding subsection, a high fuel flow rate (low fuel stoichiometry) was opted to eliminate the contribution from the Nernst-loss. This analysis has disclosed the effect of the temperature variations on the current variations (counter-flow). However, it is a fact that the Nernst-loss in the realistic fuel flow conditions is significant [12]. Therefore, the impacts of both the temperature variations and Nernst-loss on the current variations will be analyzed under the realistic conditions in the following.

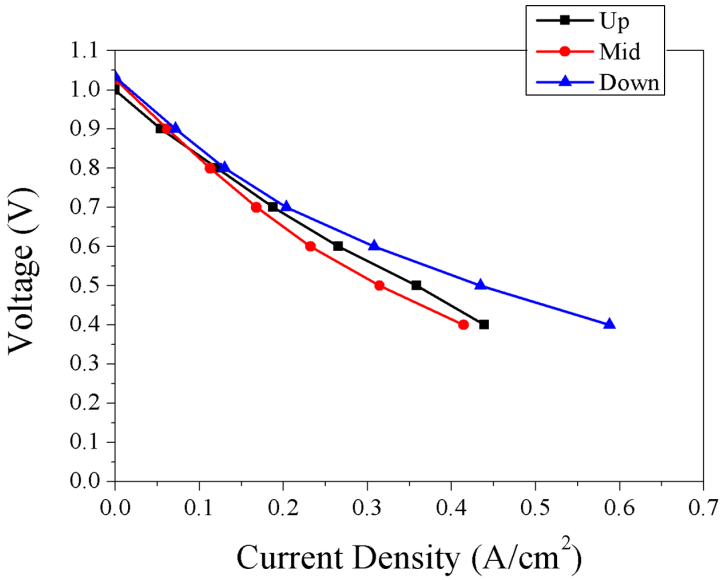

Figure 4.9: *I-V curves of the segments with the co-flow configuration for H_2/N_2=40/40 and O_2/N_2 (air)=500 cm^3/min.*

Fig. 4.9 illustrates the longitudinal current variations measured at the realistic fuel flow conditions. In comparison to the high fuel flow rate, herein the fuel stoichiometry is rather high (λ_{H_2} = 50% at 0.4 V). As a result, the current variations are larger, especially at lower voltages. Despite the higher temperature of the up-segment shown in Fig. 4.10 (mid- and up-segments have similar temperatures), the lower performances of the mid- and up-segments indicate that the Nernst-loss is the limiting factor. On the other hand, the longitudinal current distribution profile is different, i.e., the up-segment exhibits better performance than the mid-segment. Taking merely the continuous hydrogen consumption into account, such a current distribution profile would not be acceptable. However, it is known that the increasing concentration of the product water favors the HOR to an extent [77]. Relying on the development of a similar longitudinal temperature distribution profile with the counter-flow configuration, owing to the prevailing convective heat transfer, the interrelation among the temperature and current variations can be analyzed. This analysis will be carried out on Fig. 4.11 that presents the I-V curves measured under the realistic conditions with the counter-flow configurations. Herein, the current variations

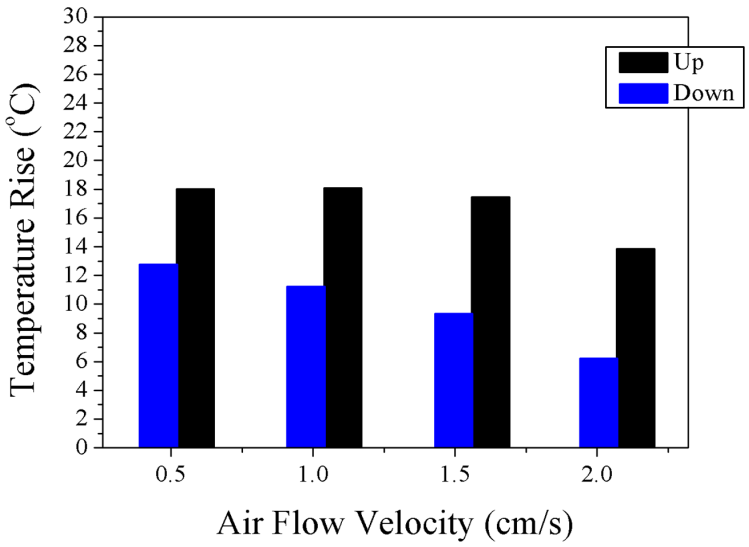

Figure 4.10: *Impact of the convective heat transfer on the segment temperatures at 0.7 V with the co-flow configuration for H_2/N_2=40/40 and O_2/N_2 (air)=500 cm^3/min, which is equivalent to 0.5 cm/s.*

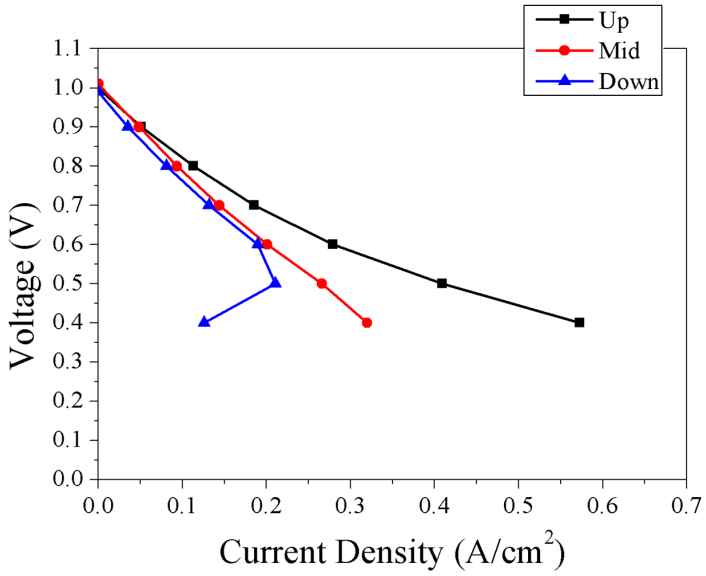

Figure 4.11: *I-V curves of the segments with the counter-flow configuration for H_2/N_2=40/40 and O_2/N_2 (air)=500 cm^3/min.*

are quite large and they become larger with the rising fuel stoichiometry (decreasing cell voltage). Beyond 0.5 V, the down-segment's current reduces, whereas the other segments' currents rise; namely, the down-segment experiences severe fuel starvation. In comparison to the co-flow case (Fig. 4.9), the longitudinal current distribution profile is distinct as well. Since the only difference between Figs. 4.9 (co-flow) and 4.11 (counter-flow) is the fuel flow direction, the large current variations can be attributed to the high temperature of the up-segment (Fig. 4.12) that boosts the local current production. Eventually, the Nernst-loss becomes more significant in the down-segment, changing the longitudinal current distribution profile.

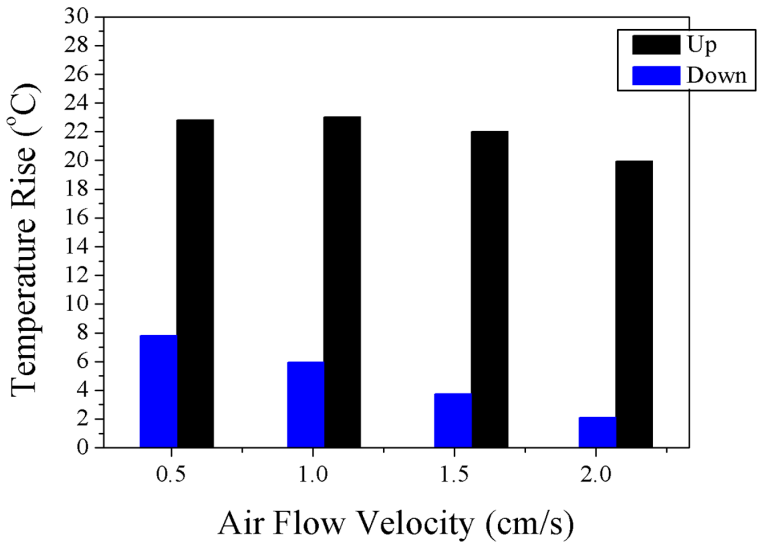

Figure 4.12: *Impact of the convective heat transfer on the segment temperatures at 0.7 V with the counter-flow configuration for H_2/N_2=40/40 and O_2/N_2 (air)=500 cm^3/min, which is equivalent to 0.5 cm/s.*

Even though the longitudinal temperature and current variations at low fuel utilization conditions are analogous in terms of the flow configurations, they become rather different under the realistic operation conditions, where the temperature and concentration variations couple. Through the analyses of Figs. 4.9-4.12, it is evident that the temperature and current variations are larger with the counter-flow configuration. The larger temperature

and current gradients are in good agreement with the numerical studies, which estimate quantitatively higher gradients indeed [35, 72, 78].

The boost in the up-segment's current production attributed to the high local temperature (Fig. 4.12) can be elaborated through the impedance analysis in a wide frequency range. In fact, the high frequency impedances (ohmic resistance) of the up- and down-segments were already discussed on Table 4.2. It was concluded that the up-segment exhibits smaller high frequency impedance owing to its higher temperature. The effect of the high temperature on the other processes will be analyzed through longitudinal impedance variations.

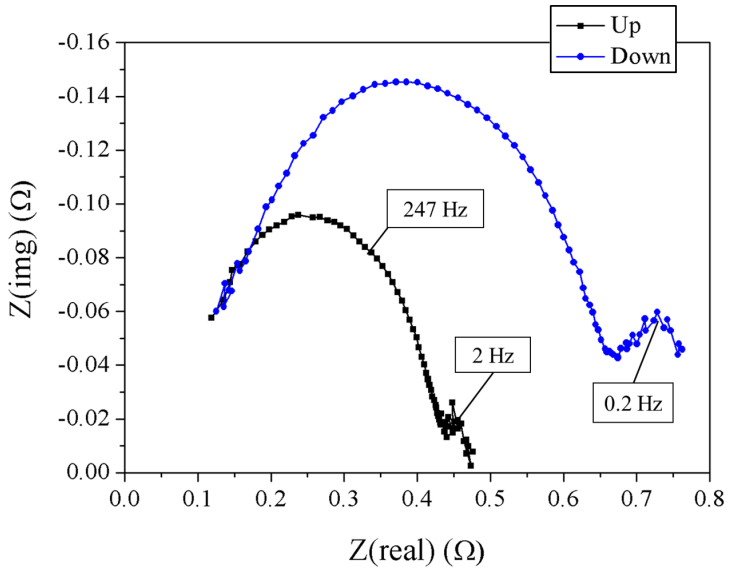

Figure 4.13: *Impedance difference between the up- and down-segments measured at 0.7 V with the counter-flow configuration for H_2/N_2=40/40 and O_2/N_2 (air)= 2000 cm^3/min, which is equivalent to 2.0 cm/s.*

Impedance spectra of the up- and down-segments measured with the counter-flow configuration are illustrated in Fig. 4.13. Though it is not easy to distinguish, in these spectra, three different frequency ranges can be defined, $\approx 10\ kHz - 376\ Hz, \approx 375\ Hz - 5\ Hz, and\ \approx\ 4\ Hz - 0.1\ Hz$, as the HFI (high frequency impedance), MFI (medium frequency impedance), and LFI (low frequency impedance), respectively. Herein, the significant impedance difference in the MFI and LFI of the segments is obvious. This no-

table impedance difference confirms the I-V curves depicted in Fig. 4.11. Namely, the total impedance is remarkably smaller in the up-segment that operates at high temperature (Fig. 4.12) and receives hydrogen at the highest concentration. Owing to the small impedance, the up-segment's current is boosted, so that the Nernst-loss rises toward the down-segment. As a result, the down-segment does not only suffer from the Nernst-loss, but also from rather low temperature shown in Fig. 4.12.

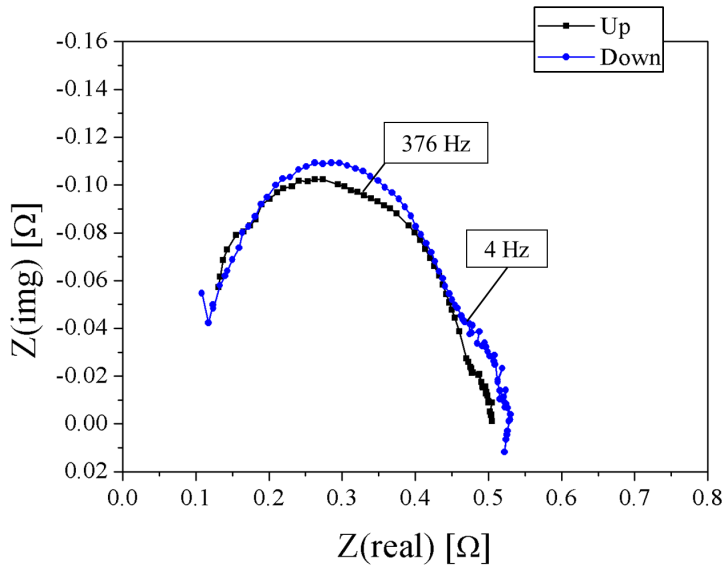

Figure 4.14: *Impedance difference between the up- and down-segments measured at 0.7 V with the co-flow configuration for H_2/N_2=40/40 and O_2/N_2 (air)= 2000 cm^3/min, which is equivalent to 2.0 cm/s.*

In contrast to the counter-flow, with the co-flow configuration the longitudinal temperature variations (Fig. 4.10) promote the uniformity of the current production along the cell. Fig. 4.14 depicts the impedance spectra of the up- and down-segments acquired with the co-flow configuration. Due to the lower temperature in the down-segment, the MFI is larger than that of the up-segment, implying the higher activation impedance. Despite the highest hydrogen concentration delivered to this segment, current production is kinetically limited. This limitation favorably restricts the boost in the Nernst-loss. Although the up-segment receives hydrogen at a smaller concentration, the total impedance of this segment is smaller

than that of the down-segment owing to the higher temperature and restricted Nernst-loss. Namely, the current distributions are leveled by the temperature variations. As a result, the further temperature variations stemming from the current variations are mitigated.

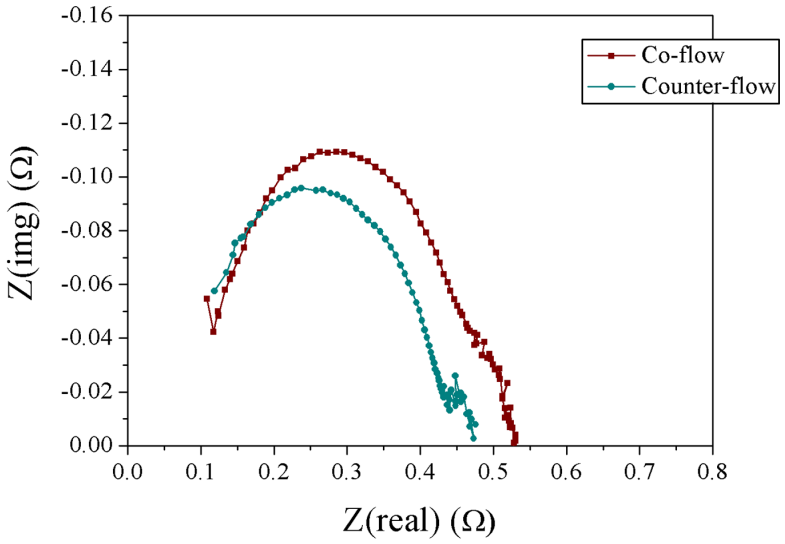

Figure 4.15: *Impedance spectra of the "upstream" segments in the co-flow (down-segment) and counter-flow (up-segment) configurations at 0.7 V for H_2/N_2=40/40 and O_2/N_2 (air)= 2000 cm^3/min, which is equivalent to 2.0 cm/s.*

Comparison of the "upstream" segments in the co- and counter-flow configurations supports the coupling of the temperature and current variations. Herein the "upstream" segment refers to the segment that receives the highest hydrogen concentration, i.e., the up-segment in the counter-flow case (Fig. 4.13) whereas the down-segment in the co-flow case (Fig. 4.14). Fig. 4.15 plots the impedance spectra of the upstream segments in both flow configurations. In this figure, the difference between the impedances of the up- and down-segments comes from the temperature difference. As the up-segment operates at higher temperature (Figs. 4.10 and 4.12), the MFI and LFI in this segment are smaller. Consequently, the current in the up-segment is boosted, resulting in larger Nernst-loss in the down-segment and eventually increasing the current variations (Fig. 4.11). In contrast, the down-segment operates at lower temperature that raises the MFI and thus reduces the

Nernst-loss. Ultimately, the longitudinal current variations become smaller (Fig. 4.9).

Since the activation and mass transport (including the Nernst-loss) impedances are coupled in the previous impedance analyses, the sensitivity of the local impedance to the temperature cannot be evidently observed. Yet, due to the direct impact of the convective heat transfer on the down-segment's temperature, it is possible to control the temperature of this segment at the same hydrogen concentration owing to the almost constant currents in the mid- and up-segments for identifying the effect of the local temperature on the local impedance. With this intention, the impedance of the down-segment was measured at

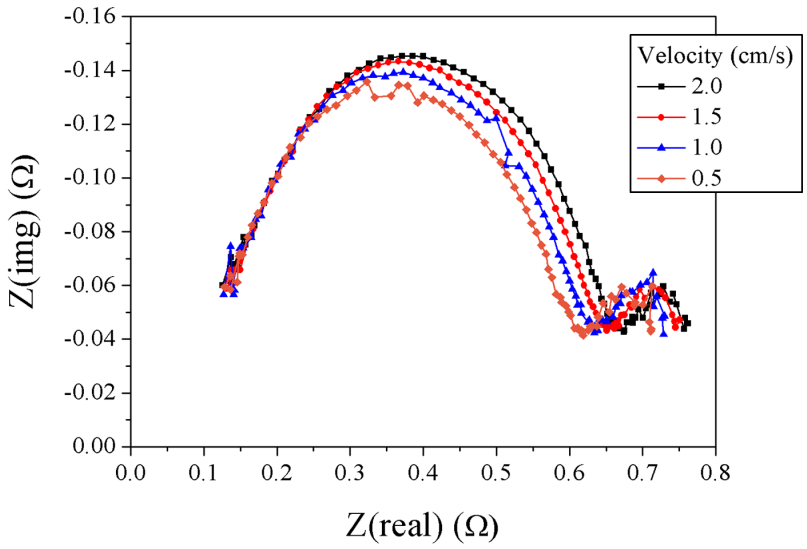

Figure 4.16: *Impact of the temperature drop achieved by increasing air flow velocity on the impedance of the down-segment measured at 0.7 V with the counter-flow configuration for H_2/N_2=40/40 and O_2/N_2 (air)= 2000 cm^3/min, which is equivalent to 2.0 cm/s.*

various air flow velocity with the counter-flow configuration as plotted in Fig. 4.16. In this figure, the sensitivity of the MFI and LFI to the local temperature is clearly shown. As the air flow velocity rises, the down-segment's temperature drops (Fig. 4.12) which in turn increases the MFI and LFI in this segment.

4.4 Conclusions

For ensuring the reliability of numerical tools developed for computing spatial variations in SOFCs, the processes involving in the temperature variations were investigated in a microtubular solid oxide fuel cell. For this elaborated investigation, in-situ measured current, temperature, and impedance variations were analyzed for the co- and counter-flow configurations at various air flow velocities. These local properties were measured by the segmentation method. Through these analyses, the following conclusions are deduced:

I) Determining the convective heat transfer rate, particularly in the entrance region, air flow velocity dominates on the longitudinal temperature variations,
II) The counter-flow exhibits larger temperature, current, and impedance variations in comparison with the co-flow configuration,
III) The high temperature coupled with the high fuel partial concentration in the fuel upstream with counter-flow configuration boosts the current density. As a result, the Nernst-loss grows toward the downstream, leading to larger current variations,
IV) Considering the dominance of the air flow velocity on the longitudinal temperature distribution and thus on the current variations, the temperature variations can be reduced by decreasing the excess air flow, so that the power consumption by the air blower can be reduced.

Chapter 5

Reliability of Numerical Tools for Characterizing Spatial Variations

5.1 Introduction

Basically, the high operation temperature (500-1000 $^{\circ}C$) of SOFCs poses nontrivial experimental difficulties [79, 80]. When it comes to the in-situ spatial characterization of current and temperature variations, the measurement becomes rather impractical. Although the segmentation method is feasible for the spatial characterization of SOFCs, application of this method on various forms of SOFC is not practical. While tubular SOFCs can easily be longitudinally characterized by the segmentation method, as they do not require gas distribution plates over the electrode surfaces, planar-forms demand a remarkable investment, because they need gas distribution plates on both anode and cathode. In other words, gas distribution plates are obliged to be segmented for longitudinal characterization [50, 51]. For such an instance, numerical models are particularly invaluable. Contribution of the numerical models to SOFC research and development can be evidently seen from the references [2, 3, 12, 25, 35, 36, 38, 61, 71, 72, 79–89, 91–98]. In principle, reliability of numerical calculations depends on the model-validation with the benchmark experimental data [82, 84–86]. Regarding the main principle of model development, the non-validated models [80, 87–92] are questionable in terms of their reliability.

The fact is that the existing SOFC models were utmost validated by conventional I-V curves [38, 71, 72, 79, 81, 83, 84, 86, 93–98]. Even though conventional I-V curves provide a good basis for the model-validation, they may not disclose spatial current and temperature variations accurately. First of all, a conventional I-V curve displays average current density, which can be mean value of different distributions of current density over the EASA at the corresponding voltage [68]. Thus, exact current variations and associated performance degradation might not be accurately identified. Secondly, an I-V validated model can predict a number of distinct temperature fields with respect to the incorporated heat transfer processes. As clearly seen from the studies by Fischer et al. [3] and Campanari et al. [2], the estimated temperature fields can in fact vary substantially from model to model. Evaluation of the temperature variations computed by numerical tools has been thus quite interesting. Thirdly, the models usually consider the influence of temperature on the overpotentials; however, they were not validated in terms of the temperature variations, except the models developed by Costamagna et al. and Razbani et al. [83, 93]. The impact of the temperature variations on the other parameters spatially computed by numerical tools has also been rather attractive.

In this study, reliability of the numerical tools for computing spatial properties is thus investigated by following analyses: first of all, accuracy of the current distribution predicted by the model validated with only the conventional I-V curve is evaluated; secondly, reliability of the temperature variations predicted by the model verified solely with the conventional I-V curve is assessed; finally, impact of validating the model with spatial temperature variations in addition to validating with the conventional I-V curve is presented for ensuring reliability of numerical tools.

For these evaluations, experimentally and numerically obtained spatial current and temperature variations are exploited. The experimental data were acquired by implementing the segmentation method on mt-SOFCs (microtubular-SOFCs). The numerical data were computed by a two-dimensional model developed for the experimental conditions.

5.2 Experimental

A segmented mt-SOFC was manufactured with the identical dimensions (Fig. 2.7), materials and processes given in section 2.2. Spatial current and temperature measurements were conducted according to the definition provided in section 2.5. Experimental conditions were established by the setup explained in 2.6. The operation temperature was 800 $^{\circ}C$ throughout the experiments. For reducing NiO to Ni, the procedure described in 2.6 was followed. All the investigations were performed in the co-flow configuration. The air flow rate was kept rather high given that the concentration polarization including the Nernst-loss was of main interest, so that H_2/N_2 flow rate was systematically varied.

5.3 Modeling

Thanks to the coupling feature of COMSOL Multiphysics (4.3a), this software was preferred to model mt-SOFCs. In order to consider various intertwined processes progressing simultaneously in mt-SOFCs, a complete model requires the equations standing for the mass, momentum, charge, and heat balances. Due to the concurrent calculation of the diverse nonlinear partial differential equations representing the balances, the coupling feature, on the other hand, constitutes a substantial computation burden. For alleviating this burden, the system was simplified as such that the mathematical equations were solved for only the EASA of the cell conjugated with the fluid channels. The model was constructed in two-dimension (2D-Axisymmetric), leaning upon the axial symmetry of the tubular geometry, which allows for well distribution of the species and the generated electrical charges in the polar coordinates. Such an approach alleviates the computation burden considerably, while yielding results as precise as a 3D model. The model was based on the following general assumptions:

- The system was at the steady-state,
- The involving species were ideal gases,
- The cell components possessed isotropic microstructures.

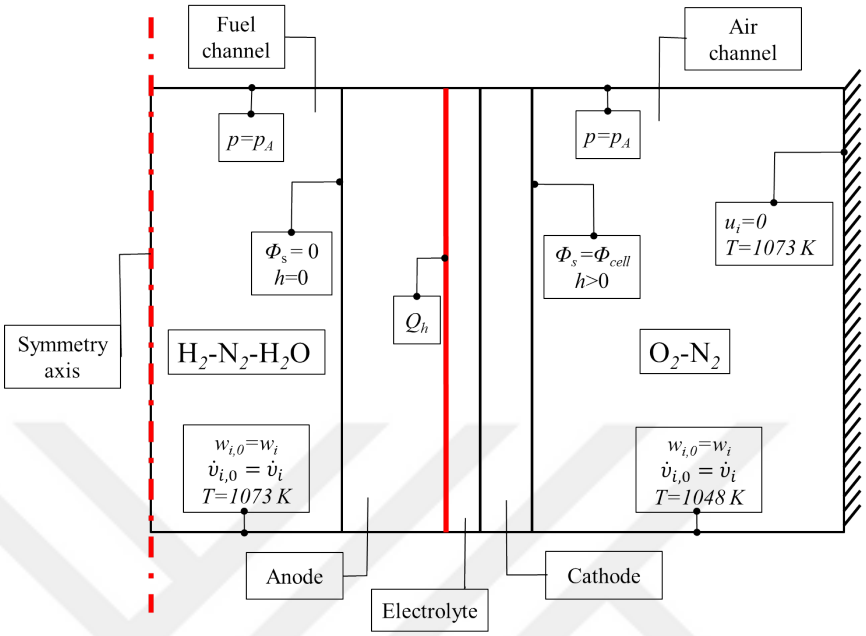

Figure 5.1: *The geometry and boundary conditions of the system considered in the model.*

5.3.1 Mass Transport

Hydrogen-nitrogen mixture was supplied to the anode, whereas air was fed to the cathode. Air was assumed to be composed of oxygen and nitrogen, ignoring the trace gases e.g., carbon-dioxide, water-vapor, etc. Upon production of water-vapor electrochemically, the gas mixture in the anode becomes three-component, (hydrogen, nitrogen, and water-vapor); however, the two-component composition of air is preserved in the cathode. Owing to the multicomponent composition of the fluids, the transport of the species was modeled by Stefan-Maxwell equations, where the divergence of the mass flux through diffusion and convection processes was considered. For each species, the following expression was solved within the channels and the porous electrodes of the anode and cathode depicted in Fig. 5.1

$$\nabla \cdot (\Upsilon + u(\rho w_i)) = X_i \qquad i \in (H_2, N_2, O_2, H_2O) \tag{5.1}$$

where the first term on the left-hand side of the equation stands for the diffusive mas transport, while the second term in the same side represents the convective mass transport. Herein u (m/s) and ρ (kg/m^3) symbolize the velocity and density, respectively. w_i, X_i,

and Υ are the mass fraction, the source term, and the diffusive mass flux vector of species i, respectively. The mass fraction was provided as the inflow boundary condition, separately for the anode and cathode.

$$w_i = w_{0,i} \tag{5.2}$$

The velocity was calculated by the momentum balance equation, which is given in the next subsection. The density of the mixture was computed via assuming the species as the ideal gases; namely,

$$\rho = \frac{pM_i}{RT} \tag{5.3}$$

where p (Pa), M_i (kg/mol), R $(J/molK)$, and T (K) stand for the pressure, the molar mass, the universal gas constant, and the temperature, respectively. The pressure and temperature values were predicted by the momentum and heat balance equations, respectively, which are described in the following subsections. In Eq. 5.1, the source term was defined as

$$X_{i,e} = \frac{\nu_{i,e} i_v}{n_e F} \qquad e \in (anode, cathode) \tag{5.4}$$

where $\nu_{i,s}$, i_v (A/m^3), n_e, and F (C/mol) are the stoichiometric coefficient, the volumetric current density, the number electrons participating in the reaction, and the Faraday constant (96485 C/mol), respectively.

The diffusive mass flux vector in Eq. 5.1 was described as

$$\Upsilon = -\rho w_i \sum_j D_{ij} \Upsilon - D_i^T \frac{\nabla T}{T} \tag{5.5}$$

where D_i^T (m^2/s), D_{ij} (m^2/s), and Υ denote the thermal diffusion coefficient, the binary diffusion coefficient of the species i and j, and the diffusion driving force, respectively. Based on the kinetic gas theory, the binary diffusion coefficient was calculated as [99]

$$D_{ij} = \frac{1 \times 10^{-3} T^{1.75} (1/M_i + 1/M_j)^{1/2}}{p(\Lambda_i^{1/3} + \Lambda_j^{1/3})^2} \tag{5.6}$$

where Λ_i (m^3/mol) is the specific atom diffusion volumes, given in Table 5.1.

In contrast to the mass transport in the channels, the mass transport within the porous electrodes was modeled by the effective binary diffusion coefficient of the species defined

by the Bruggeman correlation [100]

$$D_{eff,ij} = D_{ij}\varepsilon^{1.5} \tag{5.7}$$

assuming that $\tau \propto \varepsilon^{-0.5}$ in the

$$D_{eff,ij} = D_{ij}\frac{\varepsilon}{\tau} \tag{5.8}$$

where, ε and τ denote the porosity and tortuosity of the electrode. The porosity was determined as 0.4 for both electrodes according to the measurements.

In Eq. 5.5, the diffusion driving force is given as

$$\Upsilon = \nabla x_j + (x_j - w_j)\frac{\nabla p}{p} \tag{5.9}$$

where x_j is the molar fraction of the species j, which is defined as

$$x_j = \frac{w_j}{M_j}M_{tot}, \qquad M_{tot} = \left(\sum_i \frac{w_i}{M_i}\right)^{-1} \tag{5.10}$$

Upon inserting Eqs. 5.5 and 5.9 into Eq. 5.1, the following explicit expression is acquired

$$\nabla \cdot \left[-\rho w_i \sum_j D_{ij}\left(\nabla x_j + (x_j - w_j)\frac{\nabla p}{p}\right) - D_i^T\frac{\nabla T}{T} + u(\rho w_i)\right] = X_i \tag{5.11}$$

Table 5.1: *Properties of the species involving in the model.*

Species	Viscosity $(10^7 Pa\ s)$ [94]	Specific Heat (J/kgK) [94]	Thermal Conductivity (W/mK) [94]	Diffusion Volume [99]
H_2	$46.96 + 0.156T$	$12986 + 5.421T - 0.0045T^2$	$0.0784 + 3.7310^{-4}T$	7.07
N_2	$114.5 + 0.371T$	$1070 - 0.198T + 0.00034T^2$	$0.0116 + 5.3910^{-5}T$	17.9
O_2	$101.93 + 0.306T$	$896 + 0.0115T + 0.00026T^2$	$-0.0085 + 6.310^{-5}T$	16.6
H_2O	$-9.88 + 0.361T$	$1672 + 0.477T + 0.00019T^2$	$-0.00784 + 8.3710^{-5}T$	12.55

5.3.2 Momentum Transfer

Being coupled with the mass balance equations, the velocity and pressure of the concerning species in the free-flow mediums (channels) were modeled by weakly compressible Navier-Stokes equations. In the porous electrodes, however, Brinkman equations were employed in order to take account of the shear stress emerging within the flow. The Navier-Stokes equation reads

$$\rho(u \cdot \nabla)u = \nabla \cdot \left[-pI + \mu\left(\nabla u + (\nabla u)^T\right) - \frac{2}{3}\mu(\nabla \cdot u)I\right] + F \tag{5.12}$$

where I, μ $(Pa.s)$, and F (N/m^3) are the identity matrix, dynamic viscosity, and the volume force, respectively. In this equation, the term on the left-hand side represents the inertial forces. On the other side of the equation, the pressure forces, the viscous forces, and the external forces (e.g., gravity) applied to the fluid are standing, respectively. This equation was solved together with the continuity equation stated as

$$\nabla \cdot (\rho u) = 0 \tag{5.13}$$

Since the mixture of gases flow in the channels as well as in the porous electrodes, the dynamic viscosity of the mixture was averaged as

$$\mu_f = \sum_i w_i \mu_i \tag{5.14}$$

on the basis of the dynamic viscosity of the single species presented in Table 5.1.

Accounting the impacts of the porous structure via introducing the characteristic porosity (ε) and the permeability κ (m^2) (Table 5.2), Brinkman equation is

$$\frac{\rho}{\varepsilon}\left((u \cdot \nabla)\frac{u}{\varepsilon}\right) = \nabla \cdot [-pI + \frac{\mu}{\varepsilon}(\nabla u + (\nabla u)^T) - \frac{2\mu}{3\varepsilon}(\nabla \cdot u)I] - \left(\frac{\mu}{\kappa} + \psi|u| + \frac{X_i}{\varepsilon^2}\right)u + F$$

where ψ and X_i symbolize the Forscheimer drag and the source term, respectively. Alike the Navier-Stokes equation, the Brinkman equation was solved together with the continuity equation

$$\nabla \cdot (\rho u) = X_i \tag{5.15}$$

$$X_i = \sum_m \sum_i X_{i,e} M_i \tag{5.16}$$

The inlet boundary for the momentum balance was described as the volumetric flow rate

$$\dot{\upsilon} = \dot{\upsilon}_{i,0} \tag{5.17}$$

At the outlet, the pressure was defined to be equal to the atmospheric pressure

$$p = p_A \tag{5.18}$$

$$\left[\mu\left(\nabla u + (\nabla u)^T\right) - \frac{2}{3}\mu(\nabla \cdot u)I\right] \cdot y = 0 \tag{5.19}$$

At the wall surfaces, the non-slip ($u = 0$) condition was applied.

5.3.3 Charge Transfer

In fuel cells, electrochemical, ionic, and electronic charge transfer processes occur. The electrochemical charge transfer takes place in the TPB (triple-phase boundary) of the anode and cathode, separately. To model this type of charge transfer, Butler-Volmer equation was employed. Considering the concentration variation of the reacting species, in the present model, the concentration-dependent Butler-Volmer equation

$$i_{loc} = i_0 \left\{ \frac{c_i^*}{c_i^b} \exp\left(\frac{\beta n_e F \eta}{RT}\right) - \frac{c_j^*}{c_j^b} \exp\left(\frac{-(1-\beta) n_e F \eta}{RT}\right) \right\} \tag{5.20}$$

was used. In this equation, i_{loc} (A/cm^2), i_0 (A/cm^2), β, and η (V) are the local current density, the exchange current density, the symmetry factor, and the mixed (activation and concentration) overpotential, respectively. While c_i^b (mol/m^3) and c_i^* (mol/m^3) denote the concentration of the reactant species i in the channel inlet and in the TPB, respectively, c_j^b (mol/m^3) and c_j^* (mol/m^3) symbolize the concentration of the product species j in the channel inlet and in the TPB, respectively. Among these parameters, the symmetry factor was employed to correlate the simulation results to the experimental data, whereas the concentrations were computed from the mass balance equations.

Table 5.2: *Characteristic properties of the cell components.*

Specific heat of anode	$C_{p,a}$	450 J/kgK [75]
Specific heat of cathode	$C_{p,c}$	430 J/kgK [75]
Specific heat of electrolyte	$C_{p,el}$	470 J/kgK [75]
Porosity of anode and cathode	ε	0.4
Activation energy of anode	$E_{0,a}$	140 kJ/mol [12]
Activation energy of cathode	$E_{0,c}$	137 kJ/mol [12]
Thermal conductivity of anode	k_a	1.86 W/mK [75]
Thermal conductivity of cathode	k_c	5.86 W/mK [75]
Thermal conductivity of electrolyte	k_{el}	2.16 W/mK [75]
Reaction coefficient for anode	γ_a	$10^{11}\ \Omega^{-1}m^{-2}$
Reaction coefficient for cathode	γ_c	$10^{11}\ \Omega^{-1}m^{-2}$
Density of anode	ρ_a	3310 kg/m^3 [75]
Density of cathode	ρ_c	3030 kg/m^3 [75]
Density of electrolyte	ρ_{el}	5160 kg/m^3 [75]
Specific surface area of anode	ζ_a	$0.25 \times 10^4\ m^2/m^3$
Specific surface area of cathode	ζ_c	$2.9 \times 10^4\ m^2/m^3$
Permeability of anode	κ_a	$10^{-14}\ m^2$ [101]
Permeability of cathode	κ_c	$10^{-14}\ m^2$

Being characteristic to the electrode and electrolyte materials exist in the TPB, the exchange current density was described as [12]

$$i_0 = \gamma_e \frac{RT}{n_e F} \exp\left(-\frac{E_{0,e}}{RT}\right) \tag{5.21}$$

where γ_s $(\Omega^{-1}m^{-2})$ and $E_{0,s}$ (kJ/mol) denote the reaction coefficient and the activation energy for the hydrogen oxidation and oxygen reduction reactions in the anode and cathode, respectively. Upon inserting the values of the reaction coefficient and activation energy given in Table 5.2 into Eq. 5.21, at 800 $°C$ the exchange current density is estimated 4585 and 1153 A/m^2 for Ni/YSZ and LSM/YSZ, respectively.

The mixed overpotential was described as

$$\eta = \phi_e - \phi_{el} - \phi_{eq} \tag{5.22}$$

where ϕ_e (V), ϕ_{el} (V), and ϕ_{eq} (V) symbolize the potential of the electrode, the electrolyte, and the equilibrium, respectively. The equilibrium potential is

$$\phi_{eq} = \phi_c - \phi_a \tag{5.23}$$

at standard conditions. When the chemical activities of the species are taken into account along with the operation temperature in the Nernst equation, the equilibrium "open-circuit voltage (OCV)"

$$\phi_{eq}^{OCV} = \phi_{eq} - \frac{RT}{nF} \ln\left(\frac{c_{H_2O}}{c_{H_2} c_{O_2}^{0.5}}\right) \tag{5.24}$$

The electronic and ionic charge transfers by the electronic and ionic conductions were modeled by the Ohm's law given in the general form as

$$\nabla \cdot i_m = Q_m, \qquad i_m = -\sigma_m \nabla \phi_m, \qquad m \in (el, e) \tag{5.25}$$

where Q_m and σ_m (S/m) represent a general source term and the ionic/electronic conductivity for the electrolyte (el) and the electrodes (a, c), which are [12]

$$\sigma_{el} = 33.4 \times 10^3 \exp\left(-\frac{10.3 \times 10^3}{T}\right) \tag{5.26}$$

$$\sigma_a = \frac{4.2 \times 10^7}{T} \exp\left(-\frac{1200}{T}\right) \tag{5.27}$$

$$\sigma_c = \frac{9.5 \times 10^7}{T} \exp\left(-\frac{1150}{T}\right) \tag{5.28}$$

Due to the intrusion of the TPB into the three dimensional structure of the porous electrodes via incorporation of the 8YSZ into the electrodes, the ionic and electronic charges within the electrodes were defined as

$$\nabla \cdot i_{el} = Q_{el} + i_{v,tot} \tag{5.29}$$

$$\nabla \cdot i_{e} = Q_{e} + i_{v,tot} \tag{5.30}$$

$$\tag{5.31}$$

where

$$i_{v,tot} = \sum_{m} i_{v,m} + i_{dl} \tag{5.32}$$

given with the Faradaic and double-layer current densities represented by $i_{v,m}$ (A/m^3) and i_{dl} (A/m^3). The Faradaic current was defined as

$$i_{v,m} = -\zeta_e i_{loc} \tag{5.33}$$

where ζ_e (m^2/m^3) is the specific surface area of the electrodes, which was exploited in parallel to the symmetry factor for correlating the simulation results to the experimental data.

In order to control the cell voltage, the inner surface of the anode (the interface with the fuel stream) was set as the "electric ground" (Fig. 5.1), namely,

$$\phi_e = 0 \tag{5.34}$$

whereas the outer surface of the cathode, the interface with the air stream, was defined as the "electric potential"

$$\phi_e = \phi_{cell} \tag{5.35}$$

where ϕ_{cell} (V) stands for the cell voltage.

5.3.4 Heat Balance

The heat released during the electrochemical energy conversion process is mainly removed by the convection and radiation heat transfer processes occurring among the electrode

surfaces and the gas (fuel/air) streams. In this study, however, the heat transfer in the anode side was ignored on the ground of pre-heating pointed out in the experimental section. On this basis, the heat transfer in the cell was modeled by the general heat balance equation

$$\rho C_{p,i} u \cdot \nabla T = \nabla \cdot (k_m \nabla T) + X_{heat} \tag{5.36}$$

where $C_{p,i}$ (J/kgK), k_m (W/mK), and X_{heat} (W/m^3) symbolize the specific heat of the species i, the thermal conductivity of the cell components, and the source term. The term on the left-hand side of this equation stands for the convective heat transfer, whereas the first term on the right-hand side represents the heat conduction by the Fourier's law. The density and the velocity were coupled with the mass and the momentum balance equations.

Since the mixture of gases flow in the channels and porous electrodes, the specific heat of the mixture was described as

$$C_{p,f} = \sum_i w_i C_{p,i} \tag{5.37}$$

$$\tag{5.38}$$

considering the specific heat of the single species given in Table 5.2.

Due to the porous structure of the electrodes, the effective thermal conductivity of the electrodes

$$k_{eff,e} = (1 - \varepsilon) k_e + \varepsilon k_f \tag{5.39}$$

where k_f (W/mK) stands for the thermal conductivity of the fluid mixture f given as

$$k_f = \sum_i w_i k_i \tag{5.40}$$

where k_i (W/mK) is the thermal conductivity of species i (Table 5.2).

The fact of the power generation by a fuel cell is that the reversible overpotential (Nernst-loss) corresponding to the entropy change and the irreversible overpotential arising due to the electrochemical, electronic, and ionic charge transfer processes are converted to heat. Including both the reversible and irreversible components, the heat sources in each domain were coupled with Eq. 5.36.

The convection heat transfer occurring between the cathode surface and air stream was described by the Newton's law of cooling

$$- y \cdot (-k_c \nabla T) = h(T - T_\infty) \tag{5.41}$$

where h (W/m^2K) and T_∞ (K) refer to the heat transfer coefficient and the external temperature, respectively. In the present model, the external temperature equals to the temperature of the air stream.

The heat transfer coefficient was estimated via

$$Nu_D = \frac{hD_h}{k_i} \tag{5.42}$$

where Nu_D and D_h (m) denote the Nusselt number and the hydraulic diameter, respectively. Considering the constant heat flux through the boundary between the cathode and air stream, and the annular geometry of the system, $Nu_D = 10.2$ was adopted [76]. This condition was applied for the default temperature calculations, yet, it was altered for the temperature validation purposes.

Relying on the electric furnace that maintained the cell operation temperature at 800 $°C$, the temperature at the outer surface of the quartz tube was assumed to be constant at 800 $°C$ for the default temperature calculations; however, it was changed for validating the temperature variations.

As for the radiation heat transfer, only the surface-to-ambient radiation is considered between the cathode surface and the air stream in this model, which was defined by the Stefan-Boltzmann law

$$-y \cdot (-k_c \nabla T) = \epsilon \sigma_{SB}(T_\infty^4 - T^4) \tag{5.43}$$

where ϵ and $\sigma_{SB} = 5.67 \times 10^{-8}\ W/m^2K^4$ represent the emissivity of the silver paste coated on the cathode surface and Stefan-Boltzmann constant, respectively. The emissivity was set 0.49 [102] for the default temperature calculations, whereas it was varied for verifying the temperature variations. The ambient temperature equals to the air temperature.

The surface-to-surface radiation was omitted to alleviate the computation burden.

5.4 Results and Discussion

5.4.1 Experimentally and Numerically Obtained Conventional and Spatial I-V Curves

Due to the continuous consumption (e.g., hydrogen and oxygen) and production (e.g., water, carbondioxide) of reactants and products, respectively, variation of the current over the EASA of an SOFC is inevitable. These spatial current variations might result in remarkable performance degradation, depending on the cell design and the operation conditions [68]. In SOFCs, the obligation of the high operation temperature, for attaining a satisfactory ionic conductivity, favors the electrochemical charge transfer kinetics to a notable degree; as a result, the concentration gradient over the EASA becomes substantial [103]. For mitigating/eliminating the concentration gradient, numerous studies were devoted to the diagnosis of the current variations. Many of these studies have been conducted via the numerical models, but the accuracy of the models has not been discussed anywhere, due presumably to the difficulties in executing experiments at high temperatures. Based upon the in-situ measured spatial data, in the following subsection, the reliability of the numerical models are analyzed in terms of the current variations. At a given temperature and cell voltage, the spatial current variations in an SOFC are a function of the inlet conditions, for instance, the flow rates and the compositions of the gases flowing into the anode and cathode, separately. To alleviate the current variations, the inlet conditions should thus be optimized, for which the numerical models are extensively exploited.

The conventional and spatial I-V curves of the cell are hence presented for distinct inlet flow rates and compositions in this subsection. In order to obtain realistic results for practical applications, the operation conditions yielding the conventional I-V curves plotted in Fig. 5.2 were determined as the "benchmark conditions" in this study, as will be referred hereafter. Upon adjusting the specific surface areas (ζ_a and ζ_c) and the symmetry factor (β) of the electrodes finely, the numerical and the experimental conventional I-V curves were correlated and plotted in Fig. 5.2. The agreement between the conventional I-V curves is rather good down to 0.5 V; however, it deteriorates at lower cell voltages. Such characteristics appear in the other SOFC models as well [38, 83, 86, 93, 95]. Relying on this

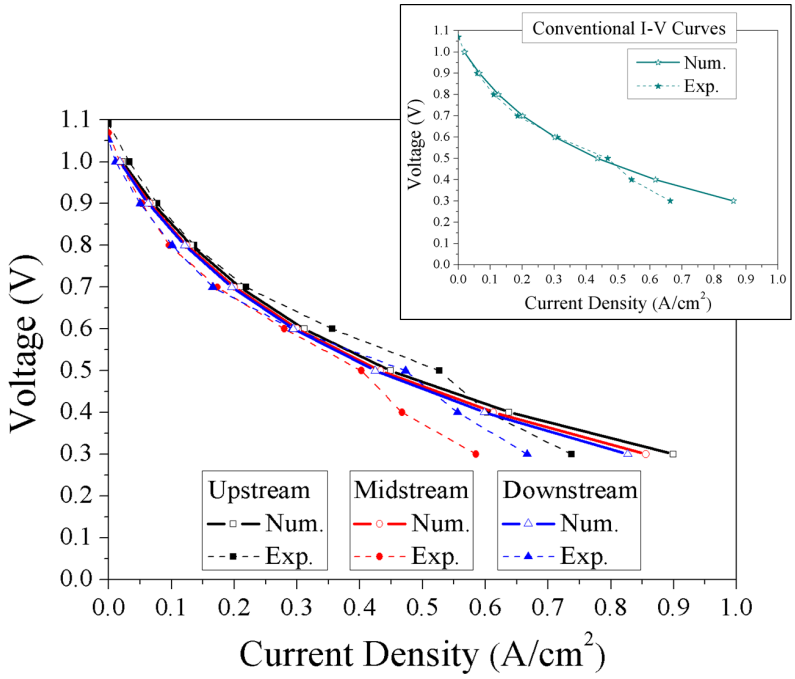

Figure 5.2: *The conventional and spatial I-V curves of the mt-SOFC obtained experimentally and numerically for H_2/N_2=40/20 and O_2/N_2 (air)=2000 cm^3/min.*

correlation, the spatial I-V curves in the mt-SOFC were also computed and attached to Fig. 5.2. Overall, the numerical model estimates smaller current variations, irrespective of the cell voltage. Since the current variations grow at low cell voltages, the numerical results depart from the experimental ones further. The largest deviation between the numerical and experimental I-V curves is observed in the midstream segment. According to the experimental data, the most striking evidence is that the downstream segment yields higher performance than the midstream segment, despite the higher reactant concentration (hydrogen and oxygen) in the midstream. This "irregular" longitudinal current distribution profile does not appear in the numerical results, disclosing the fact that an additional process takes place in the cell, which is not considered in the model.

As stated previously, inlet flow rates and compositions of the gas streams are typically optimized via employing the numerical models, which are validated by the conventional I-V curves under benchmark conditions. With the same approach, preserving the inlet fuel composition in the benchmark conditions, the numerical data for higher hydrogen and nitrogen flow rates were computed by the model validated with the benchmark conditions (Fig. 5.2). The correlation between the numerically and experimentally obtained conventional I-V curves accompanied with the spatial I-V curves are illustrated in Fig. 5.3.

In contrast to Fig. 5.2, Fig. 5.3 presents a better correlation between the conventional I-V curves through the cell voltage span. From this correlation, it is possible to deduce that the discrepancy at low cell voltages (below 0.5 V) in Fig. 5.2 is associated with the transport of hydrogen to the TPB. In other words, the model does not compute the mass transport limitation accurately. According to the spatial I-V curves, the numerical calculations underestimate current variations, due evidently to the inaccuracy in the computation of the mass transport limitation. The experimental results again exhibit the irregular current variation profile at higher fuel flow rates, too.

While exploring the optimum operation conditions by employing a numerical model, as outlined previously, the second practice would be varying the inlet composition of the gas streams. In this respect, the inlet molar ratio of hydrogen is reduced from 0.66 (Figs. 5.2 and 5.3) to 0.4, which would intuitively disclose the competence of the model in predicting the mass transport limitations. Note that the numerical calculations were carried out

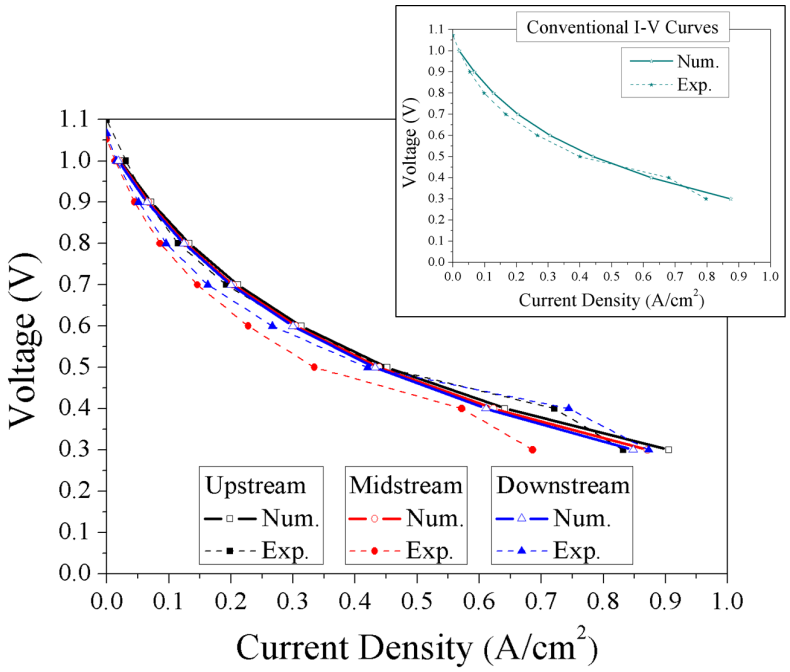

Figure 5.3: *The conventional and spatial I-V curves of the mt-SOFC numerically and experimentally acquired for H_2/N_2=80/40 and O_2/N_2 (air)=2000 cm^3/min. The numerical calculations were executed by the model validated for H_2/N_2=40/20 and O_2/N_2 (air)=2000 cm^3/min (Fig. 5.2).*

by the model validated under benchmark conditions (Fig. 5.2). The obtained numerical results are compared with the experimental data in Fig. 5.4.

Alike Fig. 5.3, Fig. 5.4 depicts a good correlation between the numerical and experimental conventional I-V curves, through the voltage range. However, Fig. 5.4 displays also a rather good correlation among the numerical and experimental spatial I-V curves. This correlation could get distorted, if the I-V curves were plotted down to 0.3 V. Note that Fig. 5.4 shows the I-V curves down to 0.4 V, due to lack of experimental data; in contrast to the former figures presenting the curves down to 0.3 V.

In Fig. 5.4, the experimental results show that the decrease in the inlet molar ratio of hydrogen via increasing the nitrogen flow rate restricts the current variations, indicating the improved mass transport process. The increase in the nitrogen flow rate (molar ratio)

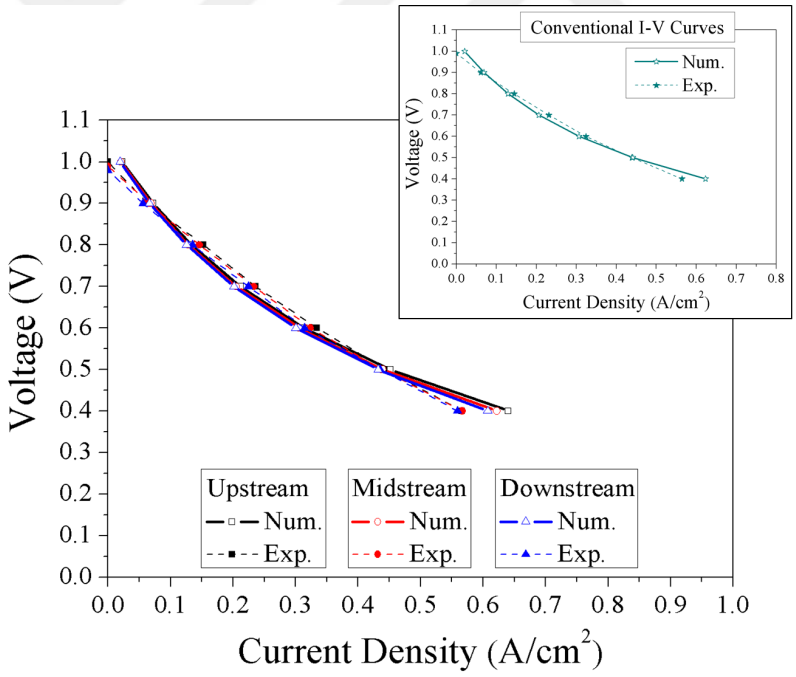

Figure 5.4: *The conventional and spatial I-V curves acquired experimentally and numerically for H_2/N_2=80/120 and O_2/N_2 (air)=2000 cm^3/min. The numerical data are from the model validated for H_2/N_2=40/20 and O_2/N_2 (air)=2000 cm^3/min. (Fig. 5.2)*

seems to aid the removal of product water-vapor. Since the model lacks the function to

capture the mass transport limitation, the numerical data agree well with the experimental data. When the nitrogen flow rate is lower, as in Figs. 5.2 and 5.3, the mass transport limitation emerges in the midstream because of the product water-vapor, which yields the irregular current distribution profile. Depending on the concentrations of hydrogen and water-vapor, however, the product water-vapor favors the reaction kinetics [77], as noticed in the downstream segment.

The good correlations among the numerically and experimentally obtained conventional I-V curves for different fuel flow rates and compositions allow us to state that the model-validation with the conventional I-V curve under benchmark conditions provides accurate results for other fuel flow rates and compositions as well. However, the numerical calculations exhibit smaller current variations than the experimental measurements. In particular, the mass transport limitation appearing at low cell voltages (smaller than 0.5 V) is not captured by the model, which might be related to the temperature variations. If the temperature elevates toward the downstream, the mass transport limitation can be compensated; because temperature can favor the reaction kinetics in a fully coupled multiphysic model [103]. The presence of the compensating effect is analyzed in the following subsection.

5.4.2 Experimentally and Numerically Acquired Spatial Temperature Variations

Basically SOFCs are obliged to operate at rather high temperatures, at which only a limited number of materials can sustain. Besides, the specific functions of the components are assured upon subsequent heat treatment processes at temperatures even higher than the operation temperatures (ca. 1450 $°C$). Since an SOFC is composed of various components (electrodes, electrolyte, interconnectors), the divergence among the thermal expansion coefficients of the cell components poses a high risk of thermal stresses. Due to the high temperatures, the thermal stresses can either arise during fabrication or during the operation; as a result, the components can get cracked [32, 37, 54, 55, 90] For the thermal stresses emerging during the operation, the spatial temperature variations are held responsible. In this respect, modeling has been widely applied to estimate the temperature

variations [2, 3, 35, 38, 72, 79, 80, 84, 86–91, 94–96, 98]. However, the regarding models are hardly validated with the experimentally collected temperature data. The models developed by Costamagna et al. [83] and Razbani et al. [93] indeed present the agreement among the numerical and experimental temperatures. Yet, in these studies, the temperatures were measured in the gas streams for only quite small current densities, utmost 0.25 A/cm^2. The rest of the SOFC models are either not validated at all [2, 3, 35, 80, 87–92], or rely on the validation with the conventional I-V curves [38, 72, 79, 84, 86, 94–96, 98], as discussed in the former subsection. Therefore, in the following, it is attempted to analyze the reliability of the temperature variations computed with the model validated solely with the conventional I-V curve.

When the SOFC models validated with the conventional I-V curves are evaluated, it can be seen that the temperature variation profile and the maximum temperature gradient change significantly from model to model. Thus, it is difficult to draw a trustworthy conclusion about the contribution of the spatial temperature variations to the thermal stresses. As the models are contrasted, the incorporation of the radiant heat transfer appears to be the major difference among them. In the planar-SOFC models, both the surface-to-ambient and the surface-to-surface radiations are often neglected [67, 72, 86, 87, 104]. The surface-to-surface radiation is omitted, because the planar-SOFCs are sandwiched between interconnectors; namely, the temperature difference between the contiguous cell surfaces is negligible. Within the gas channels, the length-to-height ratio is quite large to restrict the surface factor for radiation [72]. However, this assumption does not hold according to the study conducted by Yakabe et al. [35]. In their model, the radiant heat transfer influences the spatial temperature profile and the gradient considerably. After adding the radiant heat transfer, albeit the maximum and minimum surface temperatures do not change, the temperature distribution profile changes, dropping the maximum temperature gradient significantly. It is usually stated that the surface area of a single planar-SOFC opening to the ambient is sufficiently small to ignore the surface-to-ambient radiation. This type of radiation is indeed considered by Costamagna et al.; as a result, a good agreement is achieved among the numerical and experimental results, at least for small current density [83].

In tubular-SOFCs, the impact of the radiant heat transfer is expected to be quite large,

Table 5.3: *Spatial temperature distributions along with the concerning processes and parameters from the model developed by Campanari et al. [2]. Note that the numerical values corresponding to the cell voltage are approximately extracted from the respective graphs.*

Form	**Heat transfer**	**Gases**	**Composition**	**Inlet temp. (K)**	**Inlet velocity (m/s)**
Tubular SOFC	Conduction, convection	Hydrocarbons	0.258 H_2, 0.284 H_2O, 0.11 CH_4, 0.057 CO, 0.228 CO_2, 0.063 N_2	823	--
		Air	0.21 O_2, 0.79 N_2	1104	--

Cell voltage (V)	**Current density (A/cm^2)**	**Heat flux (W/cm^2)**	**Min. temp. (K)**	**Max. temp. (K)**	**Max. temp. gradient (K/m)**	**Vicinity of max. temp. (Axial direction)**
0.69	0.18	0.0972	940	1210	500	Outlet

because the total EASA of a cell interacts with the ambient and the neighbor cell surfaces in a bundle. Regarding the Westinghouse concept, the surface-to-surface radiation occurs between the cell and the air feed tube as well. Incidentally, the models from Campanari et al. and Fischer et al. were developed for the same Westinghouse concept and they present numerical results for rather similar boundary conditions, as presented in Tables 5.3 and 5.4. Although both models ignore the surface-to-ambient, only Fischer et al. take account of

Table 5.4: *Spatial temperature distributions along with the concerning processes and parameters from the model developed by Fischer et al. [3]. Note that the numerical values corresponding to the cell voltage are approximately extracted from the respective graphs.*

Form	**Heat transfer**	**Gases**	**Composition**	**Inlet temp. (K)**	**Inlet velocity (m/s)**
Tubular SOFC	Conduction, convection, surface-surface radiation	Hydrocarbons	0.217 H_2, 0.317 H_2O, 0.123 CH_4, 0.057 CO, 0.223 CO_2, 0.063 N_2	884	--
		Air	0.21 O_2, 0.79 N_2	1100	--

Cell voltage (V)	**Current density (A/cm^2)**	**Heat flux (W/cm^2)**	**Min. temp. (K)**	**Max. temp. (K)**	**Max. temp. gradient (K/m)**	**Vicinity of max. temp. (Axial direction)**
0.6	0.2	0.126	1100	1600	600	Middle

the surface-to-surface radiation between the cell and the air-feed-tube. Due primarily from this difference, the maximum temperature gradient as well as the temperature distribution profile along the cell alter considerably.

As to the other models, it is hard to conduct a fair comparison among them, because the calculations were carried out under diverse boundary conditions. In this circumstance, it is more straightforward to analyze the temperature variations computed by the present model, as realized in the following.

Table 5.5: *The parameters employed for computing the temperature variations.*

Air velocity	**Air inlet temperature**	**Furnace temperature**	**Heat transfer coefficient**	**Emissivity of cell surface**
0.02 m/s	1069 K	1073 K	18.6 W/m^{2}K	0.49

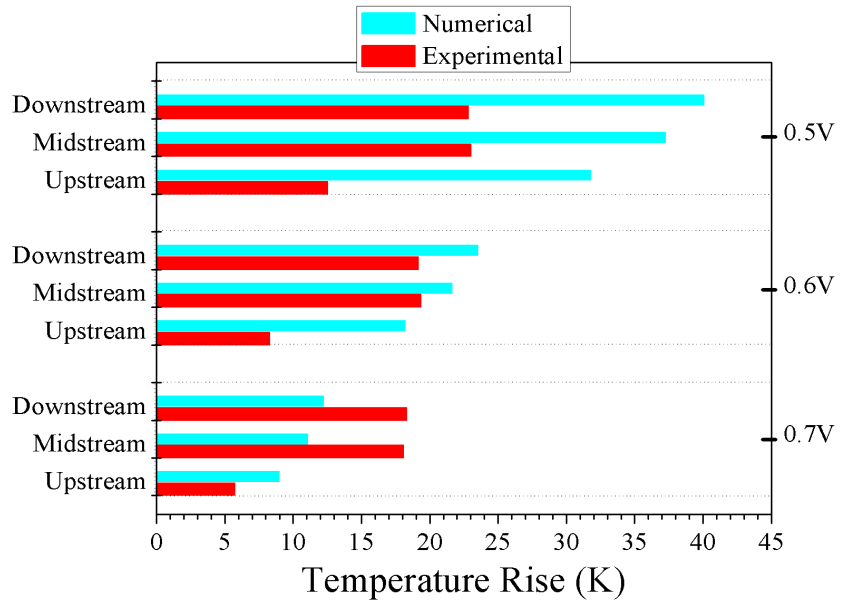

Figure 5.5: *The numerically computed and experimentally measured segment temperatures normalized to the operation temperature (800 °C) for H_2/N_2=40/20 and O_2/N_2 (air)=2000 cm^3/min. Note that the numerical temperatures were calculated by the model verified for H_2/N_2=40/20 and O_2/N_2 (air)=2000 cm^3/min (Fig. 5.2).*

Following the identical model-validation strategy with the other models, based on the conventional I-V validation for $H_2/N_2 = 40/20\ cm^3/min$ and $O_2/N_2(air) = 2000\ cm^3/min$ (Fig. 5.2), the segment temperatures were numerically computed on their cathode surfaces. The parameters employed for the calculations are given in Table 5.5; which were determined according to the concerning material characteristics and the experimental conditions. Unlike that of the current variations, the accuracy of the temperature variations is analyzed for only the benchmark conditions, because the difference in the cell performance with respect to the fuel flow conditions is negligible, as presented in the previous subsection. Besides, the heat transfer was neglected in the anode side, owing to the pre-heating.

The numerical and experimental segment temperatures are presented for various cell voltages in Fig. 5.5. In this figure, the numerical and experimental segment temperatures exhibit distinct temperature distribution profile as well as the maximum temperature gradients. Herein, the numerical segment temperatures are higher than the experimental ones, and the difference grows significantly with the decreasing cell voltage.

Even though the descending cell voltage prompts the steep elevations in the numerically estimated segment temperatures, the experimental temperatures do not exhibit such big elevations. The large difference seen among the experimental temperatures of the upstream and the other segments remains almost the same regardless of the voltage. This temperature difference is attributed to the convective heat transfer, because it is a function of air velocity [103].

Since all the physics are coupled in the model, the rather high numerical temperatures displayed in Fig. 5.5 should have enhanced the current density at low cell voltages (below $0.6\ V$). Due to the large deviations between the numerically and experimentally acquired segment temperatures, the discrepancy among the numerical and experimental I-V curves analyzed in the former subsection should have enlarged. This argument is justified in the next subsection, upon validating the model in terms of temperature variations.

Previously, it was argued that the radiation has a big effect on the accuracy of the temperature variations in tubular-SOFCs. In order to justify this effect, the surface-to-ambient radiation is ignored in the present model, so that the calculations were conducted, maintain-

ing all the other settings. In Fig. 5.6, the calculated segment temperatures are compared with the numerical and experimental segment temperatures depicted in Fig. 5.5

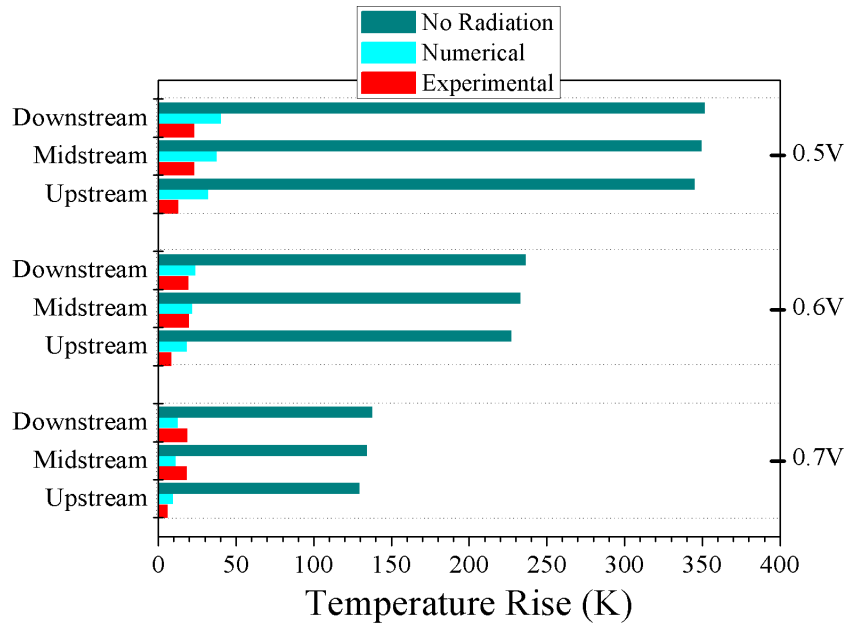

Figure 5.6: *The numerically computed segment temperatures normalized to the operation temperature (800 °C) with/out surface-to-ambient radiation contrasted with the experimentally measured segment temperatures for H_2/N_2=40/20 and O_2/N_2 (air)=2000 cm^3/min. Note that the numerical temperatures were estimated by the model verified for H_2/N_2=40/20 and O_2/N_2 (air)=2000 cm^3/min with/out radiant heat transfer.*

Fig. 5.6 manifests the enormous temperature rise in all the segments, when the radiant heat transfer is not considered. The temperature rise increases with the reducing cell voltage. From this finding, it can be concluded that the radiant heat transfer must be included in the similar SOFC models.

5.4.3 Impact of Model Validation by Spatial Temperature Measurements

As expressed with the equations in the charge transfer subsection, temperature is quite influential on the kinetics of the electrochemical reactions, and on the electronic and ionic conductivities of the electrodes and the electrolyte [103]. Temperature is also effective on the diffusion processes. As presented in Fig. 5.5, the numerically estimated temperatures substantially depart from the experimentally measured ones at high current densities,

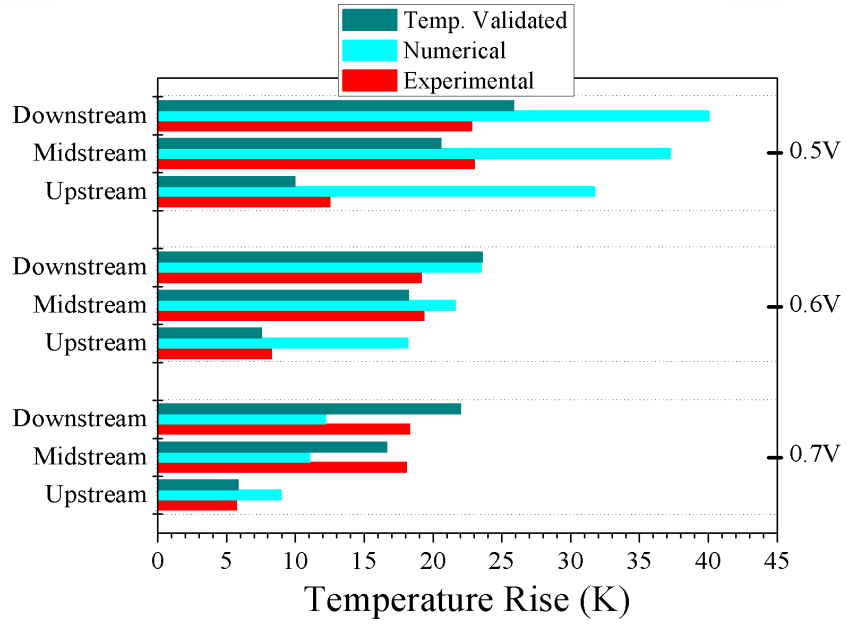

Figure 5.7: *The agreement among the numerical and experimental segment temperatures normalized to the operation temperature (800 °C) for H_2/N_2=40/20 and O_2/N_2 (air)=2000 cm^3/min after validating the model for the temperature variations, in addition to the validation with the conventional I-V curve.*

where the electronic/ionic conductivity of the components and the diffusivity of the species play a quite important role in terms of the respective overpotentials. Recalling the deviation among the numerical and experimental I-V curves in the high current density region (below 0.5 V, Figs. 5.3 and 5.2), validation of the model in terms of the temperature variations is anticipated to improve the accuracy of the numerical calculations. To justify

this anticipation, the numerical and experimental segment temperatures were correlated, as illustrated in Fig. 5.7. For achieving this correlation, the parameters associated with the convection and radiation heat transfer processes, namely, the air flow velocity, the heat transfer coefficient, the furnace temperature, and the emissivity of the cell material (silver paste) were finely adjusted. With this model, the conventional and spatial I-V curves were computed for the benchmark conditions, as illustrated in Fig. 5.8.

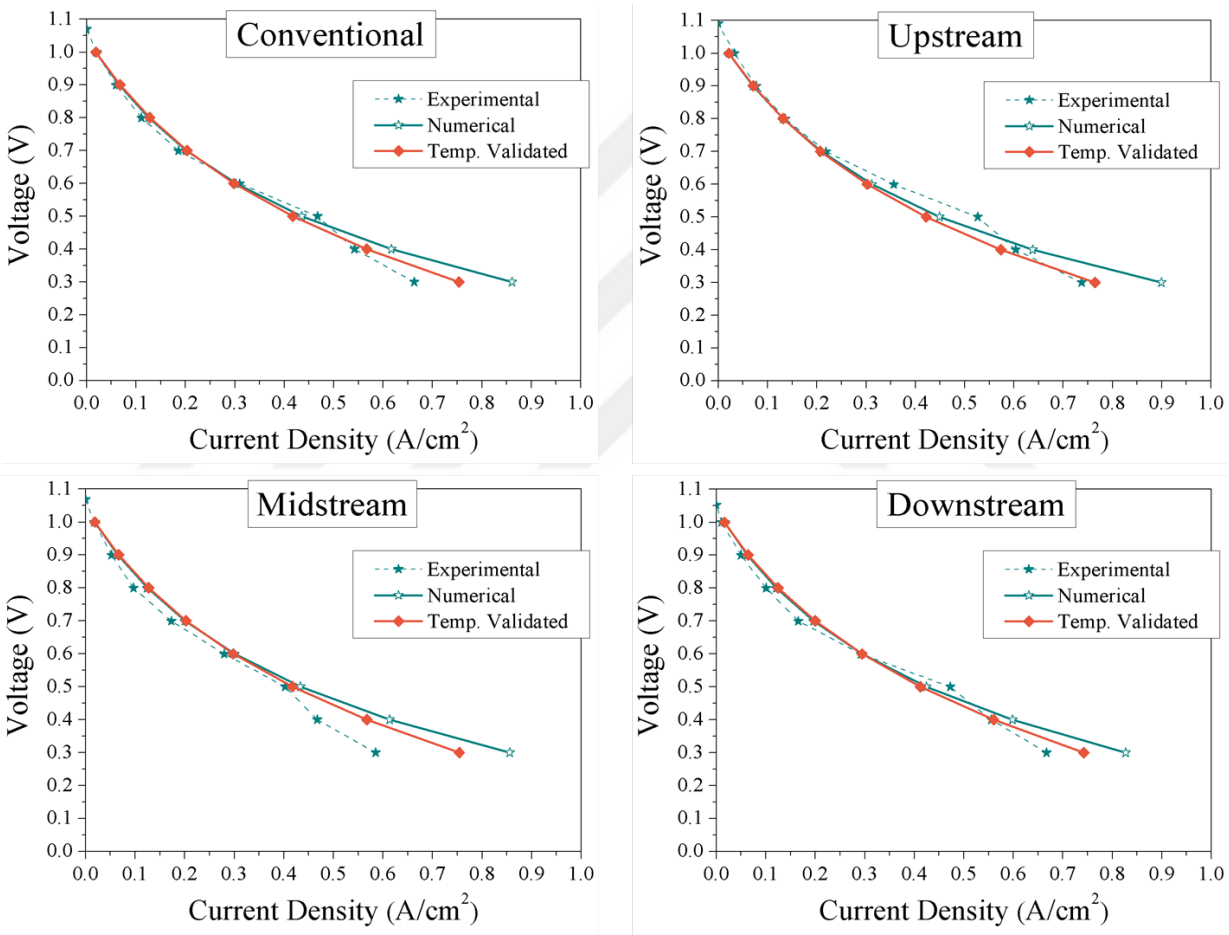

Figure 5.8: *The numerically computed and experimentally measured conventional and spatial I-V curves for H_2/N_2=40/20 and O_2/N_2 (air)=2000 cm^3/min upon validating the model with temperature variations, in addition to the validation with the conventional I-V curve.*

Fig. 5.8 shows a better correlation between the numerical and experimental conventional and spatial I-V curves. The improvement in the correlation appears particularly in the low voltage (high current) region. Thanks to the rather high temperatures predicted based on the essential consideration of the heat transfer processes (Fig. 5.5), the concerning overpotentials were underestimated; as a result, the numerical current density was greater than the experimental one (Figs. 5.3 and 5.2). After verifying the temperature variations with the spatially measured values (lower temperatures), the numerical current density reduces due to the smaller segment temperatures, which approaches to the experimental current density. These findings demonstrate that the model-validation with the spatial temperature measurements improve the reliability of the numerical SOFC tools for computing the spatial variations in the characteristic properties. It should be recalled that the mass and heat transfer processes in the recent model were simplified as much as possible. It is hence expected that more precise numerical results might be obtained upon improving the mass transport modeling.

5.5 Conclusions

Due mainly to the concentration variations of the reactants and products along the respective flow channels, the longitudinal current and temperature variations are crucial in SOFCs, as they result in the performance and structure degradations (e.g. RedOx cycling). It is hence required to characterize the longitudinal variations. The high operation temperature of SOFCs poses nontrivial experimental difficulties. When it comes to the in-situ spatial characterization of the current and temperature variations, the measurement becomes rather impractical. Although numerical tools are available, they need to be verified with the experimental data. Based on the spatial current and temperature measurements, which were in-situ carried out via the segmentation method, in this study, the reliability of a numerical model was evaluated and the following conclusions are drawn:

I) Validating the model with only a conventional I-V curve obtained under benchmark conditions provides good conventional I-V prediction at high cell voltages for other inlet fuel flow conditions as well,
II) Spatial current variations computed by the conventional I-V validated model are un-

derestimated, particularly at low cell voltages,
III) Numerical and experimental results display substantially distinct spatial temperature distribution profiles,
IV) The radiant heat transfer exhibits significant impact on the spatial temperature gradients emerging in microtubular-SOFCs,
V) Verification of the model with both the conventional I-V curve and the temperature variations improves the accuracy of the numerical calculations, particularly at low cell voltages.

Chapter 6

Spatial Variation in Reforming Rate of Methane in SOFCs

6.1 Introduction

In combination with its storage and transport issues, the insufficient distribution infrastructure of the most appropriate energy carrier hydrogen has been postponing the commercialization of various fuel cell systems. In regard of the recent demands for using conventional fuels, such as methane and other higher hydrocarbons, owing to their widespread distribution lines accompanied with the easy-to-store characteristics [75, 105, 106], SOFCs have been relatively promising for various applications, ranging from mega-scale power plants to micro-scale portable applications.

Referring to the fuel tolerance of SOFCs, though the electrochemical oxidation of methane in SOFCs is quite slow [31, 107, 108], the rate of the electrochemical carbon-monoxide oxidation is reported to be comparable to that of the HOR (hydrogen oxidation reaction) [31, 108]. Since SOFCs operate with nickel-based catalysts at high temperatures, they resemble CSRs (catalytic steam reformers), which are usually employed to produce hydrogen from hydrocarbons through reforming processes [13, 25, 41]. The operational and structural analogy between CSRs and SOFCs inspires researchers to unify the regarding fuel reforming and energy conversion processes. This unified concept is referred to as

DIR (direct internal reforming) and investigated extensively with various numerical and experimental approaches [13, 25, 31, 41, 53, 60, 61, 105–107, 109–113].

In CSRs, methane is reformed through so-called MSR (methane steam reforming) and water gas shift reactions given in Eq. 6.1 and 6.2, respectively. During the DIR, however, the water gas shift reaction is frequently reported to remain in the thermodynamic equilibrium. Therefore, the MSR reaction has been the focus of researches [75, 107, 113].

$$CH_4 + H_2O \leftrightharpoons CO + 3H_2 \qquad \Delta H_{1273K} = 227kJ/mol \tag{6.1}$$

$$CO + H_2O \leftrightharpoons CO_2 + H_2 \qquad \Delta H_{1273K} = -31kJ/mol \tag{6.2}$$

Despite CSRs operate with the external supply of heat and water, the DIR allows for replacing the external sources by the products of the exothermic HOR in SOFCs written as

$$2H_2 + O_2 \leftrightharpoons 2H_2O \qquad \Delta H_{1273K} = -250kJ/mol \tag{6.3}$$

Depending on the conditions, 40-70% of the heat released from SOFCs is estimated to be sufficient for maintaining the power generation through the MSR reaction [25, 75, 110]. In practice, the waste heat generated during the operation of SOFCs is removed by an excess flow of air in the cathode channel based on the convective heat transfer. This waste heat can indeed be internally consumed by the MSR reaction, so that the air flow rate, size of the air blower, and the respective power consumption can be reduced.

It is a fact that the rate of the MSR reaction substantially varies along the flow field of fuel depending on the thermodynamic equilibrium of the MSR reaction, which is established by concentrations of the involving species. Namely, concentrations of the species change notably along the fuel flow field. As a result, the heat absorption rate by the MSR reaction and the heat production rate by the HOR alter spatially. The balance between the absorption and production rates of heat affects the temperature distribution profile remarkably [25, 41, 107, 108, 110, 112, 113]. Given temperature variations are very crucial in SOFCs, their characterization is highly appreciated. Bearing in mind that SOFCs are designed in various forms, numerical tools are considered to be the most appropriate spatial characterization tools for DIR-SOFCs as well. For computing temperature variations in DIR-SOFCs, the energy balance in numerical tools requires accurate definition

of the MSR reaction rate as a function of species-concentrations. Due to the complexity of the DIR, the experimental investigation of the MSR reaction rate has been conducted in CSRs [25, 31, 75, 105–107, 109, 110]. Although CSRs operate at similar temperatures on the nickel-based catalysts, characteristics of operating SOFCs remarkably differ from CSRs because of the HOR. Moreover, particular structural differences between them were reported [41, 105, 110]. Even though few research groups explored the DIR in operating SOFCs [110, 113], they did not address the spatial variations in the MSR reaction rate along the cell, which is highly demanded for ensuring reliability of numerical SOFC tools for spatial computation.

Given that the segmentation method can easily be applied on mt-SOFCs (microtubular-SOFCs), temperature variations can be in-situ identified. Comparison of the local temperatures obtained from the operations of a mt-SOFC with syngas (a mixture of hydrocarbons) and its equivalent H_2/N_2 would disclose the endothermic cooling by the MSR reaction, and provide insights into the MSR reaction rate along the cell. In this study, local currents and temperatures were thus in-situ measured by the segmentation method along a mt-SOFC operated with syngas (50% pre-reformed methane) and equivalent (100% conversion of syngas to hydrogen) mixture of H_2/N_2. Leaning upon the longitudinal current (concentration) and temperature variations, variation in the rate of the MSR reaction is analyzed.

6.2 Experimental

A segmented mt-SOFC was fabricated with the same dimensions, materials, and processes described in section 2.2. Spatial current and temperature measurements were conducted according to the definition provided in section 2.5. Experimental conditions were established by the setup explained in section 2.6. The operation temperature was 800 $^{\circ}C$ throughout the experiments. For reducing NiO to Ni, the procedure described in section 2.6 was followed. All the investigations were performed in the co-flow configuration. The air flow rate was rather high at 2000 cm^3/min (25 $^{\circ}C$, 100 kPa) for all the experiments, given that the internal reforming was the main focus. On the other hand, the fuel type and flow rate were changed consistently as shown in Table 6.1. In this table, the inlet syngas compositions are identical and correspond to 50% pre-reformed methane [114], assuming a

Table 6.1: *Syngas and equivalent H_2/N_2 flow rates in cm^3/min at 25 °C and 100 kPa.*

	Syngas					Equivalent
Matrix	H_2	H_2O	CO_2	CH_4	CO	H_2/N_2
SYN-1	36.0	33.4	8.0	10.4	2.4	80/40
SYN-2	27.0	25	6.0	7.8	1.8	60/30
SYN-3	18.0	16.7	4.0	5.2	1.2	40/20

S/C (steam/carbon) ratio of two. The equivalent H_2/N_2 flow rates in Table 6.1 correspond to 100% conversion of syngas to hydrogen. The content of water in syngas was adjusted by a humidifier (Chino Co. Ltd.) depicted in Fig. 2.8.

It is important to note that the ideal DIR-SOFCs concept aims to eliminate the pre-reforming process completely, where the inlet H_2 and CO concentrations would be zero. In this case, SOFCs would operate under quite severe conditions, e.g., substantial temperature gradient, carbon deposition, etc., which would likely prompt rapid degradation processes. The inlet syngas composition in this study was hence arranged relatively mild in comparison with the ideal conditions for conducting reliable and sustainable operation at least during the investigations.

6.3 Results and Discussion

6.3.1 Current and Temperature Fluctuations

Segment currents were measured during the cell operations with three different syngas flows, the SYN-1, SYN-2, and SYN-3 and their equivalent H_2/N_2 flows as defined in Table 6.1. Although the segment currents were rather stable ($\pm 10\ mA$) at any voltage with the H_2/N_2 mixture, they became relatively unstable with the supply of syngas. The segment currents and temperatures were thus recorded with a sampling rate of 200 ms for all the syngas flow conditions through the voltage range and plotted in Figs. 6.1, 6.2, 6.3, respectively, to provide insights into the simultaneously progressing HOR and MSR

reaction.

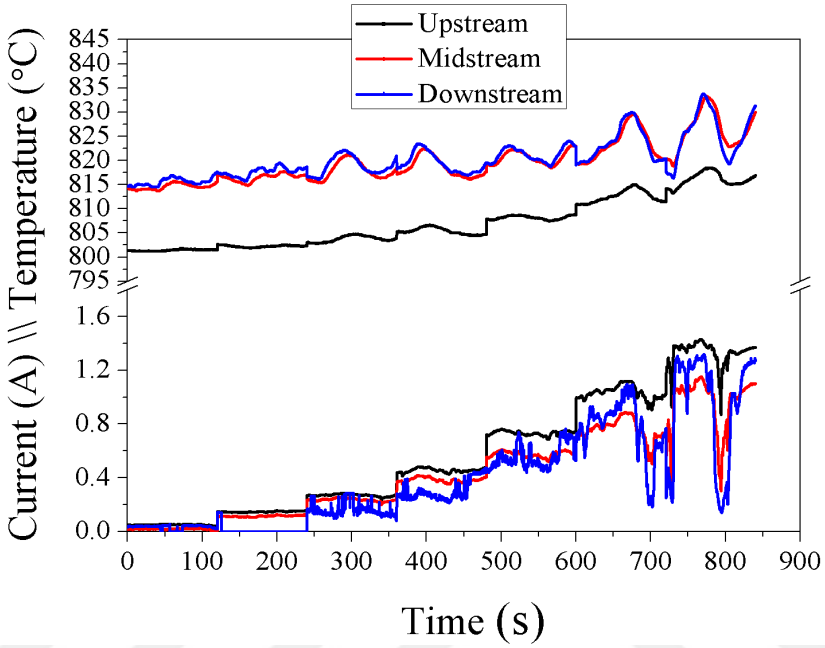

Figure 6.1: *Fluctuating segment currents and temperatures at various cell voltages for the cell operation with the SYN-1. The segments are represented by three different colors which are identical in both current and temperature curves.*

Fig. 6.1 presents the current and temperature fluctuations at various voltages from 0.9 to 0.3 V for the cell operation with the SYN-1. In this figure, all the segments show irregular fluctuations in their temperatures. However, the midstream and downstream segments exhibit similar and more frequent fluctuations with the larger amplitudes than the upstream segment. As the segment currents rise, the amplitudes of the temperature fluctuations in all the segments increase. Despite the upstream and midstream segments indicate rather stable currents in the low and middle current regions until 600 s, the amplitudes of the current fluctuations in both segments become larger with the increasing currents. Moreover, the midstream and downstream segment currents temporarily approach to zero in the high current region between $650 - 850$ s. On the other hand, the downstream segment current fluctuates through the voltage range with an amplitude growing as the segment

current rises.

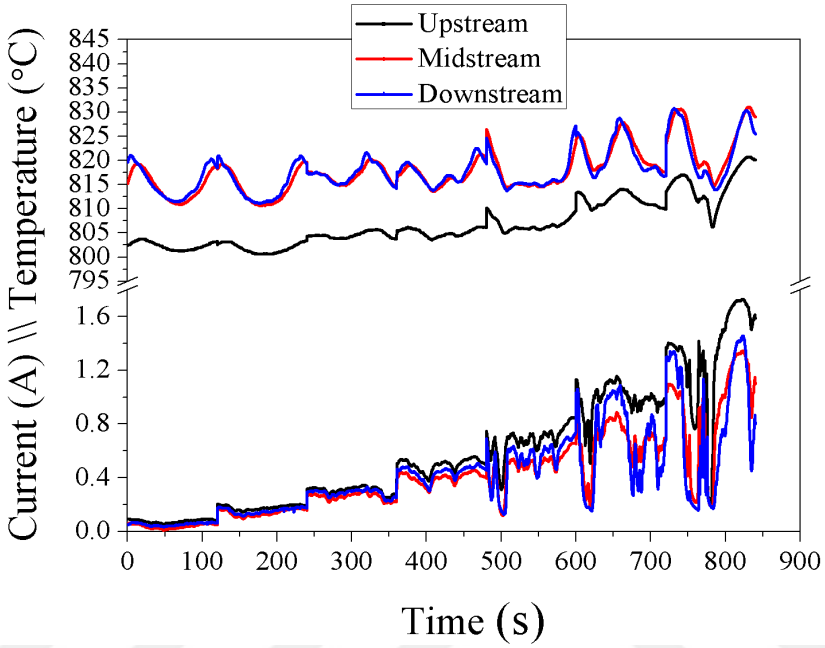

Figure 6.2: *Fluctuating segment currents and temperatures at various cell voltages for the cell operation with the SYN-2. Note that the segments are represented by three different colors which are identical in both current and temperature curves.*

The current and temperature fluctuations of the segments at various cell voltages from 0.9 to 0.3 V for the cell operation with the SYN-2 are shown in Fig. 6.2. Similar to the previous case, the midstream and downstream segment temperatures vary with the quite similar fluctuations, where the upstream segment indicates the smallest fluctuations. The amplitudes of the fluctuations in all the segments grow with the increasing segment currents. Apart from the SYN-1 case, all the segment temperatures exhibit almost the same fluctuation profile in varying amplitudes. Although the segment currents are stable and analogous in the low current region until 240 s, they become rather unstable with the increasing segment currents. In the high current region beyond 480 s, the segment currents temporarily approach to zero. Unlike the SYN-1 case, the fluctuation profiles of all the segment currents are rather similar through the voltage range.

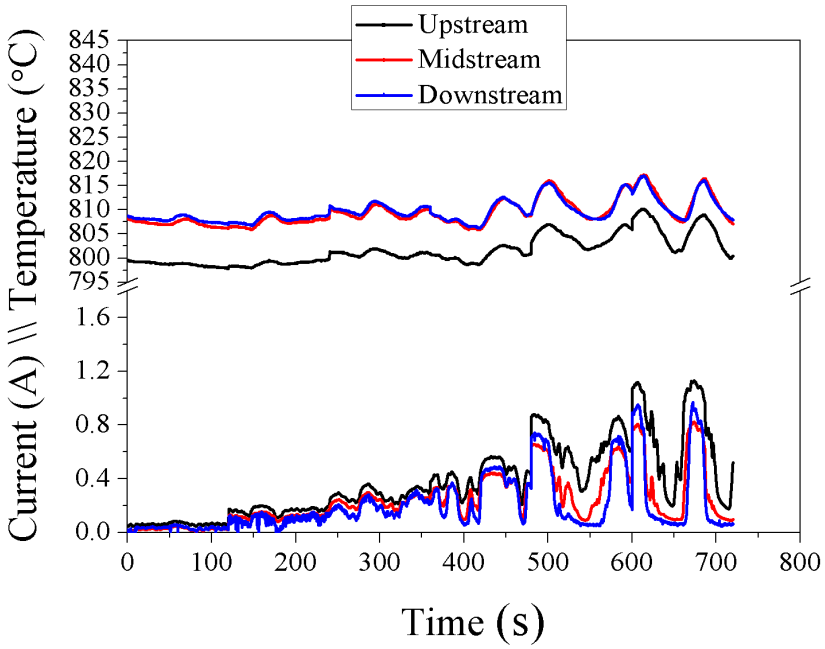

Figure 6.3: *Fluctuating segment currents and temperatures at various cell voltages for the cell operation with the SYN-3. The segments are represented by three different colors which are identical in both current and temperature curves.*

In Fig. 6.3, the fluctuating segment currents and temperatures are plotted through the voltage range from 0.9 to 0.4 V for the SYN-3. In this condition, the fluctuation profiles of the segments are rather similar. Further, the amplitudes of the fluctuations in all the segments are quite analogous. The current fluctuation profiles of the segments are also resembling each other. Moreover, the fluctuation amplitudes are similar through the voltage range. The segment currents are unstable in the low current region, and the fluctuations become quite larger as the segment currents increase. In addition, the duration of the drops in the segment currents are considerably wide in the high current region.

The experimental results reveal that the increasing segment currents and decreasing syngas flow rates from the SYN-1 to SYN-3 make the segment temperature fluctuations resemble each other. Besides, the temperature fluctuations become larger with the increasing segment currents. In particular, the midstream and downstream segments show fairly similar temperature profiles, regardless of the flow rates. The instability in the segment currents initiates at higher segment voltages as the anode gas flow rate decreases from the SYN-1 to SYN-3. Even though the instability of the upstream current in the SYN-1 and SYN-2 is less than that of the other segments, it becomes rather similar to the others in the SYN-3. In addition, the frequency and duration of the current drops enhance from the SYN-1 to SYN-3. Regardless of the fuel flow rate, the downstream segment exhibits the largest current fluctuations.

The current and temperature profiles disclose the relation between the fluctuations and the hydrogen partial pressure in the regarding segments due to the fact that the fluctuations become more frequent and larger with the increasing segment currents and decreasing fuel flow rate from SYN-1 to SYN-3. The inlet hydrogen flow rate even in the SYN-3 case is adequate to maintain the current generation by the HOR reaction [52, 68]. As the contribution of the MSR reaction is taken into account, fuel starvation is not expected, at least in the upstream segment. Therefore, it is speculated that the MSR reaction starts to dominate occupying the nickel catalysts in the TPB, causing fluctuations as the local pressure of hydrogen falls down. Namely, the MSR reaction does not proceed along with the HOR, but instead the nickel catalysts in the TPB are temporarily occupied with the MSR reaction as sketched in Fig. 6.4.

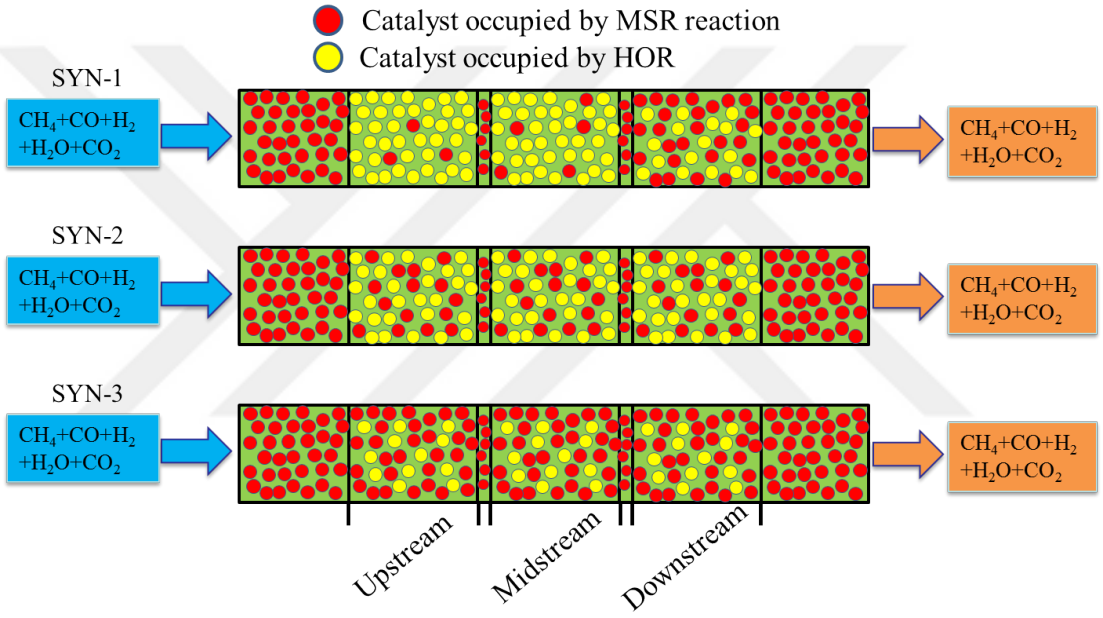

Figure 6.4: *The occupation of the nickel catalysts in the TPB (triple phase boundary) by the HOR and MSR reaction with different syngas flow rates. This schematic is intended to capture the state of the catalysts between 240-360 s corresponding to 0.7 V.*

In fact, Timmerman et al. have experimentally investigated the electrochemical performance of the planar type electrolyte-supported SOFCs operating at 800 $^{\circ}C$ with the DIR over Ni/YSZ anodes [113]. With a mixture of CH_4/H_2O at three different S/C ratios (0, 1, and 3), they show the experimental I-V curves of the whole cell for the current density up to 0.16 A/cm^2. They conducted the experiments with a fuel flow rate that is 246% larger than the SYN-1 (the inlet fuel flow rates are compared considering the electrochemical active surface area, and 100% conversion of syngas to hydrogen). They have not stated the current fluctuations in their cell, which indeed agrees well with recent findings in the same current range.

6.3.2 Longitudinal Current Variations

Based on the averages of the fluctuating currents discussed in the previous subsection, I-V curves of the segments are presented for the SYN-1, SYN-2, and SYN-3 accompanied with their equivalent H_2/N_2 flow rates in Figs. 6.5, 6.6, and 6.7, respectively. In these figures, longitudinal current distributions are shown at selected cell voltages (0.5, 0.6, and 0.7 V) in addition to the I-V curves. The fuel distribution along the cell is analyzed during the internal reforming by comparing the current distributions obtained with the syngas and H_2/N_2 flows. During the fuel distribution analysis, the water gas shift reaction is disregarded, as is frequently reported to remain in the thermodynamic equilibrium [75, 107, 113].

For the SYN-1 and the equivalent H_2/N_2 flows, I-V curves of the segments and the longitudinal current distributions at the selected cell voltages are depicted in Fig. 6.5 (a) and (b), respectively. In the H_2/N_2 case, the downstream current is close to the upstream current despite the lower fuel concentration. The high downstream current is attributed to the enhanced rate of the anodic electrochemical reaction owing to the higher partial pressure of water by the HOR [52, 115]. In the SYN-1 case, all the segments exhibit lower currents than those in the H_2/N_2 case. As the highest current in the SYN-1 case, the upstream current approaches the midstream current of the H_2/N_2 case, which is the smallest current indeed. In contrast to the H_2/N_2 case, the downstream current in the SYN-1 case is lower than the upstream current; whereas it overlaps with the midstream current for a wide

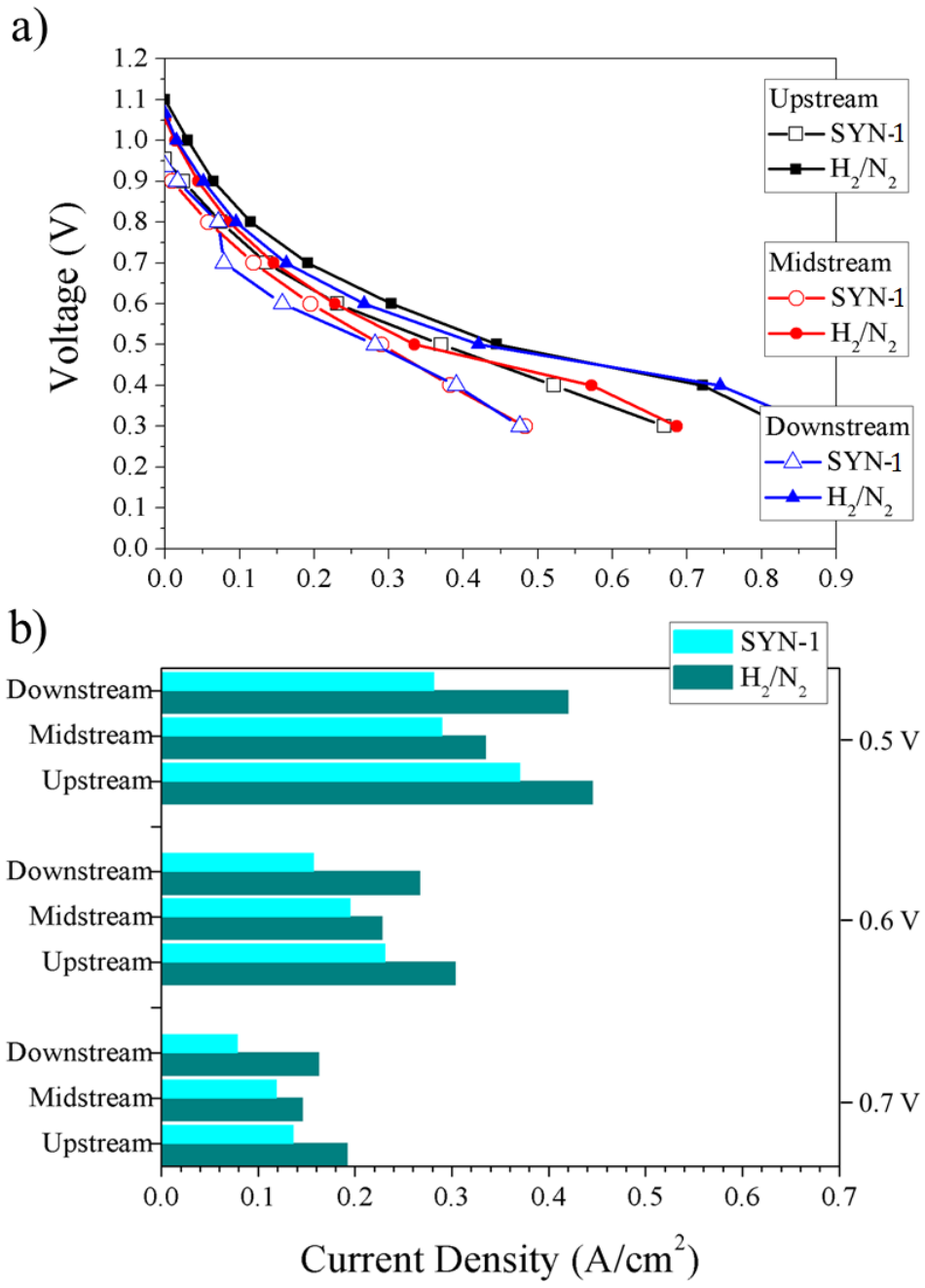

Figure 6.5: *(a) I-V curves of the segments and (b) longitudinal current distributions at various cell voltages with the SYN-1 and its equivalent H_2/N_2=80/40 cm^3/min.*

voltage range. This overlap agrees well with the analogous temperature fluctuations in the midstream and downstream segments due to the occasional occupation of the catalysts in the TPB by the MSR reaction.

Fig. 6.6 (a) and (b) present I-V curves of the segments and the longitudinal current distributions at the selected cell voltages for the SYN-2 and the equivalent H_2/N_2 flows, respectively. The I-V curves for both types of fuels are rather similar to those in the former case. In the H_2/N_2 case, the downstream current approaches the upstream current as the cell voltage decreases. The segment currents in the SYN-2 case are lower than those in the H_2/N_2 case, where the differences increase at lower voltages. In the SYN-2 case, the downstream current approaches the midstream current, whereas the midstream current is relatively lower than the upstream current. The longitudinal current distribution with the SYN-2 flow is thus different. This difference is attributed to the occasional occupation of the nickel catalysts in the TPB by the MSR reaction.

I-V curves of the segments and the longitudinal current distributions at the selected cell voltages are plotted for both the SYN-3 and equivalent H_2/N_2 flows in Fig. 6.7 (a) and (b), respectively. Apart from the previous conditions, the longitudinal current distribution profiles are different for both types of fuels. In the H_2/N_2 case, the downstream current is smaller than the upstream current. This lower downstream current shows the fuel starvation due to the lower gas flow rate. Alike the previous cases, the segment currents are smaller with the SYN-3. As the cell voltage decreases, the current differences between the SYN-3 and H_2/N_2 flows increase in all the segments. The downstream current in the SYN-3 case is lower than the midstream current, where the midstream current is considerably smaller than the upstream current. This finding discloses that the fluctuations expanded to the upstream and became larger in the midstream and downstream due to the dominantly occupation of the nickel catalysts in the TPB by the MSR reaction.

The experimental results in Figs. 6.5-6.7 show that the segment currents in the syngas conditions are lower than those in the equivalent H_2/N_2 cases. The deviation in the currents increases in all the segments as either the cell voltage or the gas flow rate decreases. This tendency agrees well with the fluctuations happening due to the occasional occupation of the nickel catalysts in the TPB by the MSR reaction.

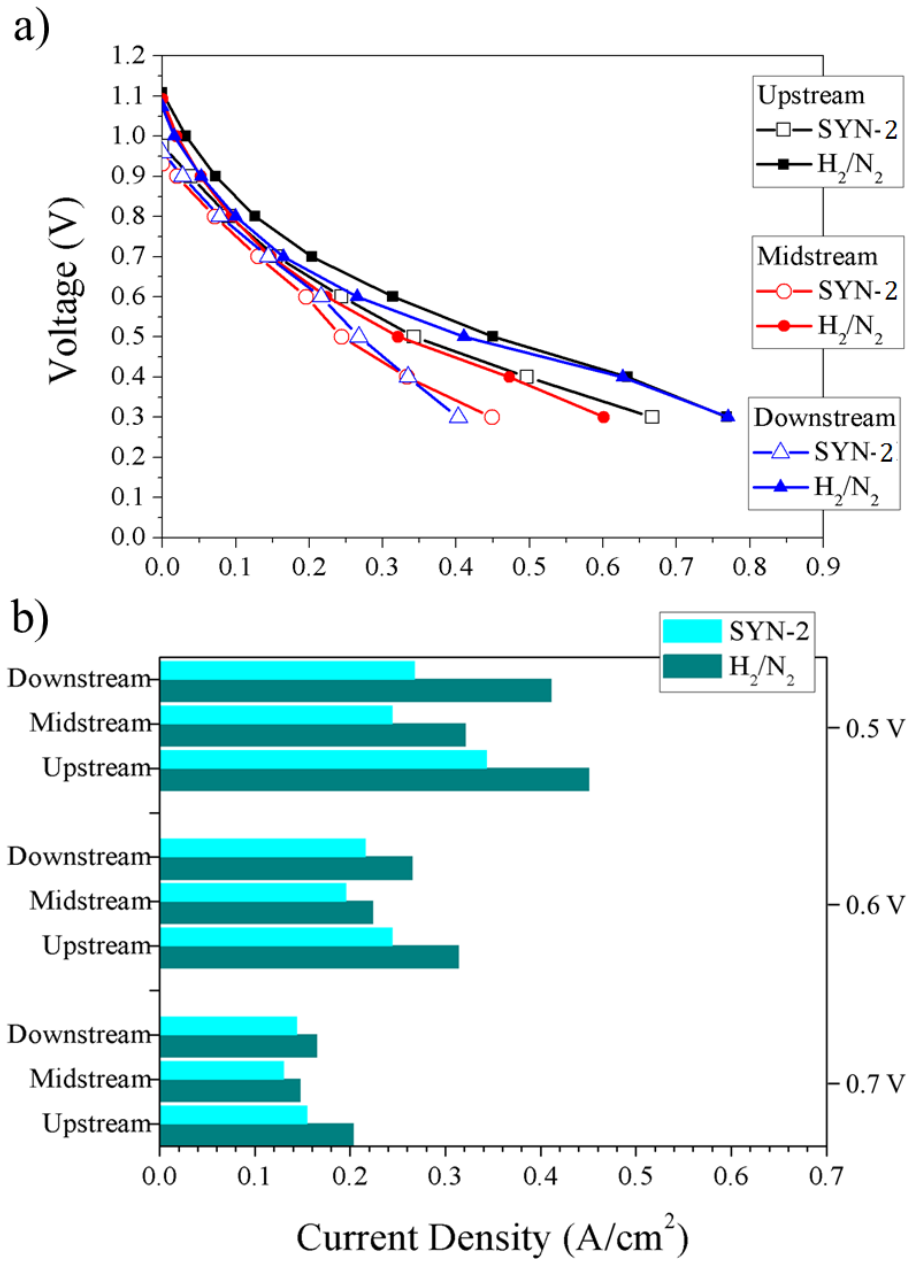

Figure 6.6: *(a) I-V curves of the segments and (b) longitudinal current distributions at various cell voltages with the SYN-2 and its equivalent H_2/N_2=60/30 cm^3/min.*

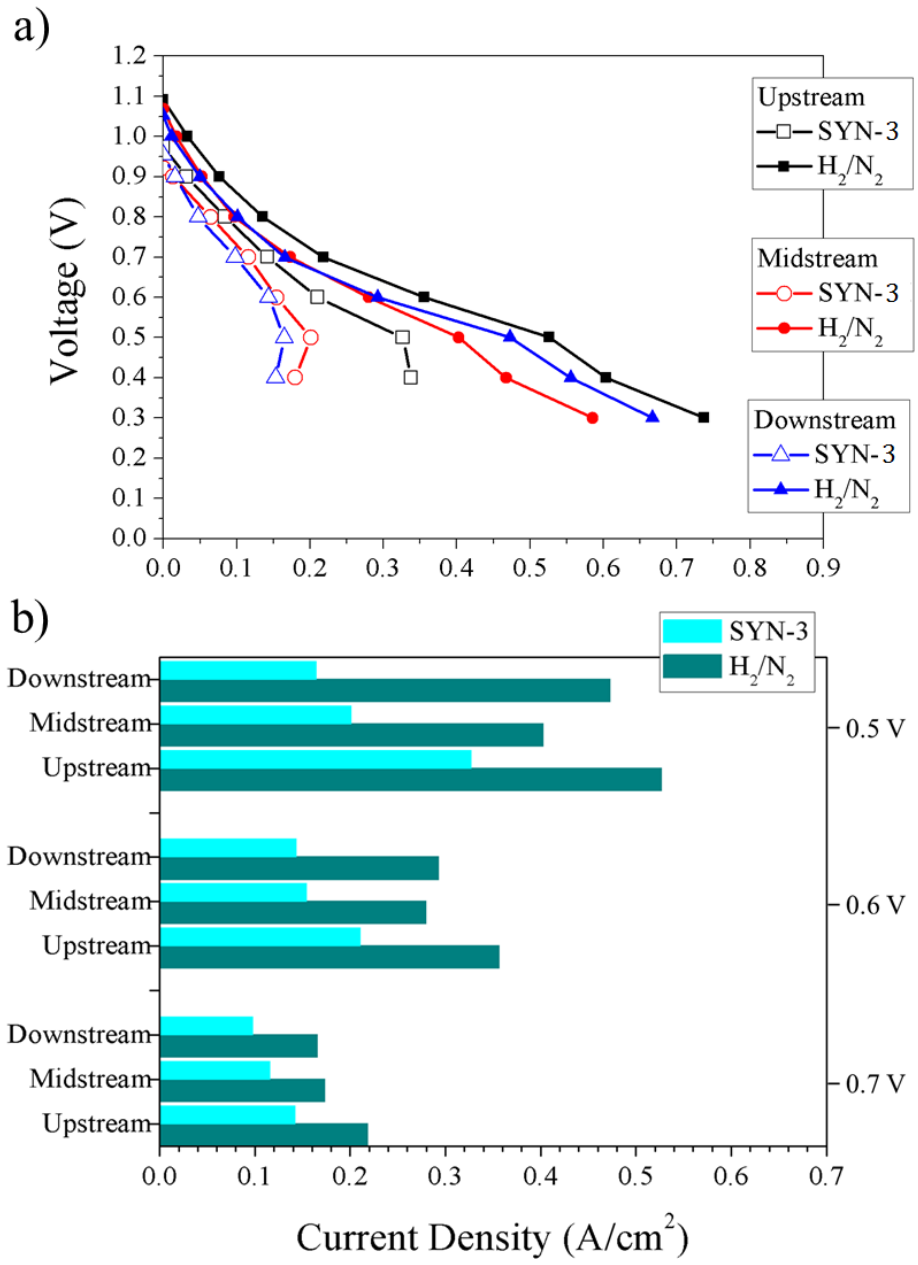

Figure 6.7: *(a) I-V curves of the segments and (b) longitudinal current distributions at various cell voltages with the SYN-3 and its equivalent H_2/N_2=40/20 cm^3/min.*

6.3.3 Longitudinal Temperature Variations

In parallel to the previous subsection, I-T curves of the segments are presented for the SYN-1, SYN-2, and SYN-3 and the equivalent H_2/N_2 flows in Figs. 6.8, 6.9, and 6.10, where the segment temperatures and currents are means of the fluctuations. These figures show also the longitudinal temperature distributions and the temperature drops due to the endothermic cooling at the selected cell voltages (0.5, 0.6, 0.7 V). For displaying the longitudinal distributions, the segment temperatures are given as the temperature rise, which refers to the elevation of the segment temperature from the furnace temperature (800 $^{\circ}C$). The temperature drop associated with the endothermic cooling was computed as the difference between the temperatures acquired with equivalent H_2/N_2 and the equivalent syngas conditions.

Fig. 6.8 (a) and (b) present I-T curves and the temperature distributions of the segments at the selected cell voltages for the SYN-1 and the equivalent the H_2/N_2 flows, respectively. Note that the segment temperatures are higher than the furnace temperature even at the OCV (open circuit voltage), indicating the heat production by the combustion of a particular amount of H_2 leaking from anode to cathode. The amount of the leakage is estimated to be negligible in subsection 4.3.1. Considering the slightly deviating segment OCVs with respect to the fuel type, the fuel leakage rate is assumed to be identical in the syngas and equivalent H_2/N_2 cases. On this basis, the temperature drops because of the endothermic cooling were computed and shown in Fig. 6.8 (b). The convective heat transfer between the cell surfaces and the co-flowing reactant/oxidant gases reduces the upstream segment temperature for both types of fuels. This heat transfer results in a significant temperature gradient between particularly the upstream and midstream segments, whereas the temperature difference between the midstream and downstream segments is small [103]. Due to the prevailing effect of the convective heat transfer, the decreasing cell voltage makes all segment temperatures rise, whereas the upstream temperature remains relatively smaller than the others. The cell operation with the SYN-1 flow causes the temperature drops in all segments with varying magnitudes, comparing with the local temperatures in the equivalent H_2/N_2 case, as presented in Fig. 6.8 (b). The temperature drop in the upstream segment is smaller than those in the other segments, which exhibit similar

temperature drops. The variations in the temperature drop of the segments are in line with the temperature fluctuations analyzed previously.

Given methane and water are reacting in the upstream, their partial pressures decrease towards the downstream. Accordingly, the temperature drops of the midstream and downstream segments are expected to decline due to the smaller methane conversion. Inversely, these segments show larger drops than the upstream segment, indicating the higher methane conversion. These larger temperature drops can thus be ascribed to the higher temperatures of the segments, which accelerate the MSR reaction according to the Arrhenius equation

$$\nu = Kexp\left(-\frac{E_{act}}{RT}\right) \tag{6.4}$$

where ν (mol/s) is the rate constant of a chemical reaction, K the pre-exponential factor, and E_{act} (kJ/mol), the activation energy.

With the rising segment temperatures (increasing cell current), higher methane conversion and hence greater temperature drops are anticipated. In contrast, the temperature drops become smaller in all the segments. This implies that the local heat production rate associated with the polarizations with the syngas flow is higher than that with the equivalent H_2/N_2 flow. Thereby, the impact of the endothermic cooling on the local temperatures is smaller [65, 116].

Fig. 6.9 (a) presents I-T curves of the segments for the SYN-2 and the equivalent H_2/N_2 flows, while Fig. 6.9 (b) shows the segment temperatures (rise) accompanied with the temperature drops due to the endothermic cooling at the selected voltages. Similar to the prior case, Fig. 6.9 (a) displays the segment temperatures higher than the furnace temperature at the OCV, indicating the H_2 leakage from anode to cathode. Leaning upon the slightly diverging segment OCVs according to the fuel type, the fuel leakage rate is again assumed to be identical in the syngas and equivalent H_2/N_2 cases while calculating the temperature drop due to the endothermic cooling. In Fig. 6.9 (a), the longitudinal temperature distribution profiles for both types of fuels resemble those in the previous case due to the convective heat transfer [103]. In Fig. 6.9 (b), all the segments exhibit the temperature drops with altering magnitudes by the endothermic cooling. In comparison

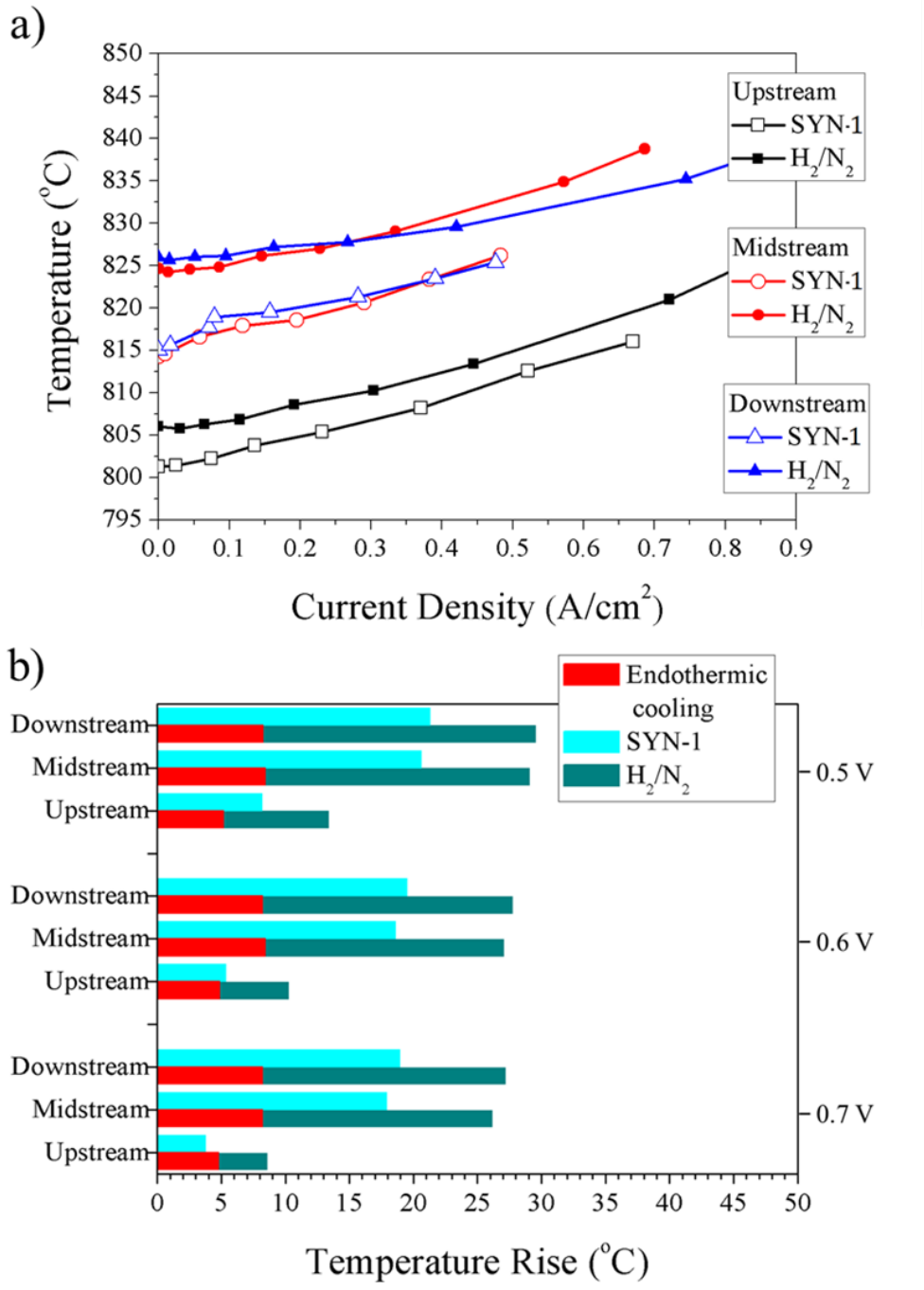

Figure 6.8: *(a)I-T curves of the segments, (b) longitudinal temperature distributions and the temperature drops due to the endothermic cooling at various cell voltages with the SYN-1 and its equivalent H_2/N_2=80/40 cm^3/min.*

with those in the SYN-1 case, the temperature drops are smaller in all the segments. These smaller drops confirm the impact of the segment temperatures on the methane conversion according to the Arrhenius equation. The temperature drops tend to decrease with increasing cell current in all the segments, as shown in Fig. 6.9 (a). This decrease is analogous to that in the SYN-1 case, indicating the larger polarizations during the syngas utilization. It should be underlined that the endothermic cooling reduces the maximum temperature difference at the OCV from 18 to 13 $°C$ along the cell. This maximum temperature difference becomes even smaller with growing cell current.

I-T curves of the segments for both the SYN-3 and equivalent H_2/N_2 flows are shown in Fig. 6.10 (a). Segment temperatures (rise) with the temperature drops at the selected voltages are displayed in Fig 6.10 (b). Alike the preceding cases, Fig. 6.10 (a) presents higher segment temperatures than the furnace temperature at the OCV, pointing out the H_2 leakage from anode to cathode. Since the difference in the segment OCVs is rather small in terms of the fuel type, the fuel leakage rate is again assumed to be same in the syngas and equivalent H_2/N_2 cases while determining the temperature drop due to the endothermic cooling. In Fig. 6.10 (a), the temperature distribution profiles with both types of fuels are analogous to the preceding cases because of the convective heat transfer [103]. Despite the smallest segment temperatures in comparison to the previous cases, the highest temperature drops are observed in all the segments. These smallest drops contradict the impact of the segment temperature on the methane conversion according to the Arrhenius equation; however, they agree well with the large temperature fluctuations. The largest methane conversion (in this case) is thus ascribed to decreasing hydrogen partial pressure towards the downstream. In parallel to the former conditions, the temperature drops in all the segments reduce with increasing current. Again, this finding reveals that the heat production rate by the polarizations are larger than the heat consumption rate by the MSR reaction. The maximum temperature difference along the cell at the OCV falls from 15 to 9 $°C$ by the endothermic cooling. This maximum temperature difference decreases further at lower cell voltages.

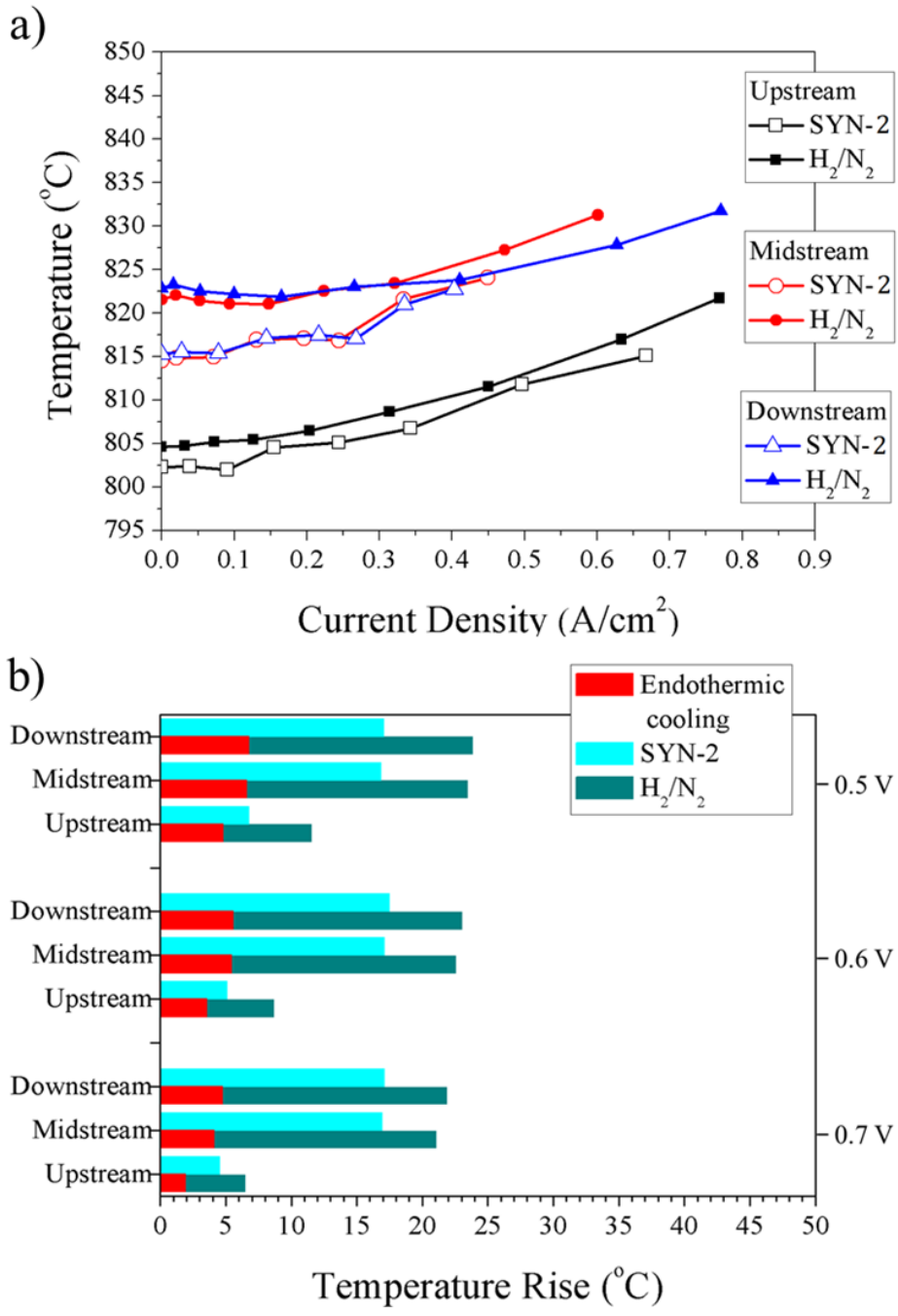

Figure 6.9: *(a) I-T curves of the segments, (b) longitudinal temperature distributions and the temperature drops due to the endothermic cooling at various cell voltages with the SYN-2 and its equivalent H_2/N_2=60/30 cm^3/min.*

6.3.4 Impact of Gas Flow Rate (Residence Time) on Methane Conversion Rate

Timmerman et al. and Saunders et al. have investigated the impact of the gas flow rate on the methane conversion over the Ni/YSZ anodes in an operating SOFC (at the OCV) at 800 $°C$ and in a single catalytic stream reformer at 700 $°C$, respectively [53,113]. They both state that the methane conversion decreases with increasing inlet gas flow rate (reducing residence time). As the HOR exhibits a notable effect on the methane conversion revealed by the current and temperature fluctuations, herein, it is intended to analyze the impact of the gas flow rate on the methane conversion at a high current density. Thereby, the longitudinal temperature (rise) distributions are compared with the temperature drops discussed previously for the three different syngas and equivalent H_2/N_2 flow rates at 0.6 V in Fig. 6.11.

The longitudinal temperature distribution profiles for both types of the fuels resemble each other regardless of the flow rate due to the convective heat transfer [103]. The temperature drops in all segments reduce with decreasing anode gas flow rate, from the SYN-1 to SYN-2. This reduction in the temperature drops implies that the methane conversion diminishes with the smaller anode gas flow rates. However, this evidence disagrees with the other researchers [53, 113]. On the other hand, all the segments show the highest temperature drops in the SYN-3 with the lowest anode gas flow rates (longest residence time). These highest temperature drops are in line with the largest and most frequent fluctuations, indicating the prevailing occupation of the nickel catalysts in the TPB by the MSR reaction. In this case, it is deduced that the effect of temperature and residence time on the methane conversion is limited in a particular range.

6.4 Conclusions

Local currents and cathode surface temperatures were in-situ measured along an anode-supported microtubular SOFC by the segmentation method for syngas (a mixture of hydrocarbons) at various flow rates. The same experiments were carried out with the equivalent H_2/N_2 flow rates, which correspond to 100% conversion of syngas to hydrogen. The current

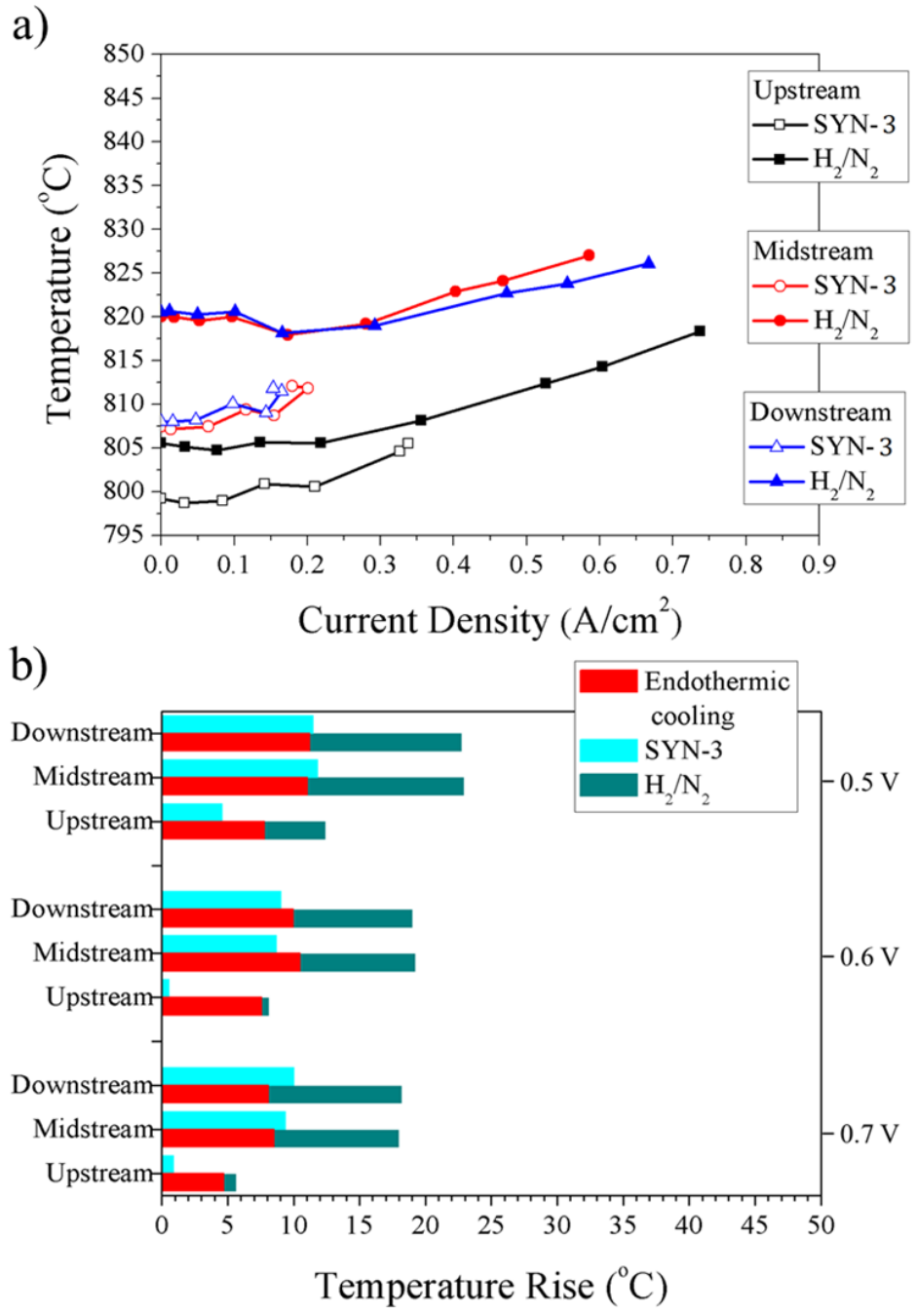

Figure 6.10: *(a) I-T curves of the segments, (b) longitudinal temperature distributions and the temperature drops due to the endothermic cooling at various cell voltages with the SYN-3 and its equivalent H_2/N_2=40/20 cm^3/min.*

and temperature distributions were analyzed along the cell during the cell operation with both types of the fuels to address the fuel distribution, endothermic cooling, and methane conversion.

The cell operation with syngas exhibits remarkable irregular fluctuations in the currents and temperatures of the segments. Analysis of the fluctuations allows us to ascribe the occurrence of the fluctuations to the occasional occupation of the nickel catalysts in the triple phase boundary by MSR (methane steam reforming) reaction.

Comparison of the current distributions along the cell for the regarding fuels reveals that, with the use of syngas, the overall performance of the cell degrades, and the inhomogeneity in the current distribution increases. Considering the local current, it can be deduced that the fuel starvation is enhanced during the syngas utilization, as a result of the insufficient methane conversion.

While using syngas, all the segment temperatures drop in the varying magnitudes due to the endothermic MSR reaction comparing to the operation with the equivalent H_2/N_2 flow. However, the maximum temperature difference along the cell becomes smaller with the internal reforming, which cancels the impact of the convective heat transfer. The temperature drops enhance from the upstream to the downstream segment regardless of the fuel flow rate. The temperature drops become smaller with the increasing segment currents. This means that the heat production rate by the polarizations is higher than the heat absorbed by the MSR reaction.

Diminishing inlet syngas flow rate (increasing residence time) makes the temperature drops larger, which implies the larger methane conversion. However, this is not consistent with all the flow rates, due to the effect of temperature. It can thus be concluded that the effect of the each parameter on the MSR reaction rate is limited in a particular range.

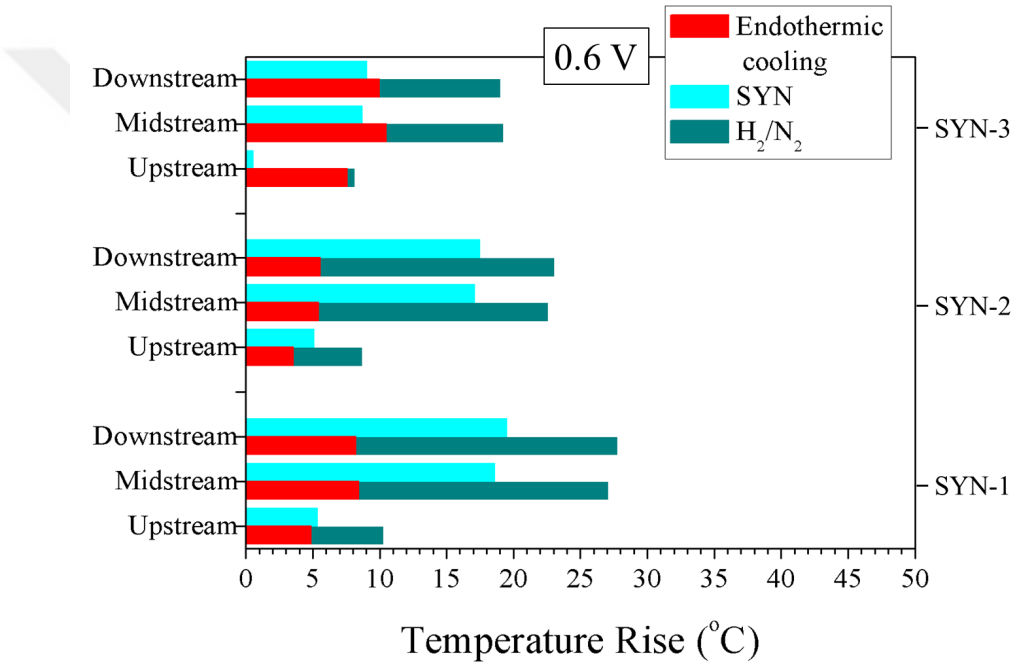

Figure 6.11: *At 0.6 V longitudinal temperature distributions with the temperature drops due to the endothermic cooling for SYN-1-3 and their equivalent H_2/N_2=80/40, 60/30, and 40/20 cm^3/min.*

Chapter 7

Conclusion and Outlook

7.1 Conclusion

Owing to the continuous consumption of the reactants and the release of the products in SOFCs (solid oxide fuel cells), as in any fuel cell, the concentrations of the reactants and products vary along the respective flow channels of the electrodes. Being related to operation conditions, the longitudinal concentration variations lead to a reversible polarization, referred to as Nernst-loss. Ultimately, in the practical sense, longitudinal current and related temperature variations emerge in the cell, resulting in performance and structure degradations (e.g., thermal stresses, RedOx cycling, and carbon deposition while utilizing hydrocarbons, etc.). Conventionally, the degradations are investigated with small cells (button cell) to gather fundamental understanding, wherein the longitudinal variations cannot be observed. In this context, the degradations are required to be elaborated in the realistic dimensions via analyzing their relationships with the longitudinally varying parameters.

The longitudinal variations can be identified either experimentally or numerically. The segmentation method being extensively applied in PEMFCs (polymer electrolyte membrane fuel cells) is feasible for the longitudinal characterization of SOFCs. In fact, it has been already implemented to characterize the Nernst-loss in few projects. Unlike PEMFCs, SOFCs are designed in various forms, such as planar, tubular, etc., to cope with ther-

mal stresses. Although the longitudinal variations and the regarding consequences occur regardless of the form, the application of the segmentation method on the various forms is not practical. While tubular-SOFCs can easily be longitudinally characterized by the segmentation method, as they do not require gas distributing plates over the electrode surfaces, planar-SOFCs demand a remarkable effort, because they need gas distribution plates on both anode and cathode. In other words, the gas distribution plates are also obliged to be segmented for the longitudinal characterization. Numerical investigations are hence quite practical, as they save time, energy, material to be invested for the investigations, and provide high resolution in terms of the longitudinal investigations. Nevertheless, numerical models can only be trusted upon validation with reliable experimental data. This Ph.D. study has thus been devoted to elaborating current and temperature variations along mt-SOFCs utilizing hydrogen and syngas (a mixture of hydrocarbons) by applying segmentation method along with a finite element model for improving the reliability of the numerical SOFC tools. Since the segmentation method can easily be realized on mt-SOFCs (microtubular-SOFCs), this study was carried out in mt-SOFCs.

Initially, the extent of the performance degradation due to the Nernst-loss was necessary to disclose. Accordingly, longitudinal current variations were in-situ measured in a mt-SOFC utilizing hydrogen. The importance of the longitudinal investigations was drawn upon demonstrating the incompetence of the conventional characterization method for longitudinal variations. The current variations were analyzed under various fuel flow conditions, and the severity of the longitudinal variations was identified under realistic operation conditions. The high risk of the RedOx cycling at low fuel flow conditions was clearly shown.

Secondly, the relationship among the longitudinal current and temperature variations was explored by analyzing longitudinal current, temperature, and impedance variations, which were in-situ acquired in a mt-SOFC. The experimental data exhibit remarkable temperature variations along the cell in both co- and counter-flow configurations. Longitudinal impedance measurements show a strong impact of the large temperature gradients on both electrolyte conductivity and reaction kinetics, influencing the longitudinal current and concentration variations. It is found that the longitudinal current (concentration) and temperature variations couple in the counter-flow configuration, exhibiting larger variations

in comparison with the co-flow configuration. Analysis of the longitudinal temperature and current variations together under various operation conditions discloses the contributions by the current variations, and the convective heat transfer between the air and the cathode surface to the longitudinal temperature variations. It is shown that the large temperature variations stem mainly from the excess air supplied as a common practice to sweep the waste heat produced in SOFCs. In this regard, the excess air supply should be avoided to minimize the temperature variations in the co-flow configuration, which would also reduce the power consumption by the air blower.

In the third phase, reliability of numerical tools was evaluated, for which a two dimensional finite element model was constructed for a mt-SOFC. With the model, the conventional I/V curve of the cell was numerically computed and correlated to the in-situ measured one. Upon this conventional validation process, longitudinal current and temperature variations were predicted by considering the heat transfer processes (including radiant heat transfer); however, remarkable deviations among the numerical and experimental values (current and temperature) were identified. Upon excluding radiant heat transfer, the deviation among the experimental and numerical temperature values became significantly larger, revealing the notable impact of radiant heat transfer on the longitudinal temperature variations. Due to the poor accuracy of temperature computation and substantial impact of temperature on the other processes in such a fully-coupled model, the model was modified to capture the in-situ measured temperature variations. As a result, a positive impact of the spatial temperature validation on estimation of the longitudinal current variations, i.e., on the reliability of numerical model is shown.

Spatial variations in characteristic properties of SOFCs are expected to be more crucial while internal reforming of hydrocarbons due to the fact that the rate the reforming reaction also spatially varies depending on the concentrations of the species exist in the fuel mixture. In this regard, numerical tools are to play a substantial role. Apart from the hydrogen-utilizing SOFCs, the rate of the heat absorption by the reforming reaction, which results in the endothermic cooling, is required to be considered for estimating the spatial variations. The endothermic cooling and the associated spatial variation in the rate of the reforming reaction were thus in-situ analyzed in this study. For these investigations,

longitudinal temperature and current variations were measured in a mt-SOFC for different syngas and equivalent (100% conversion of hydrocarbons to hydrogen) hydrogen flow conditions. Leaning upon the local temperature difference between syngas and hydrogen utilizations, the extent of the endothermic cooling along the cell was identified. Based on the endothermic cooling, the variation in the rate of the reforming reaction along the cell was analyzed as well. It is shown that the endothermic cooling varies along the cell, leveling the temperature variations identified during hydrogen utilization. The variation in the endothermic cooling was affected by the gas flow rate (residence time). In parallel to the varying rate of the endothermic cooling, remarkable fluctuations in the local currents and temperatures were observed, which were affected by the residence time. The fluctuations were attributed to the competition among the reforming reaction and hydrogen oxidation reaction, as they were both catalyzed by nickel within the anode. With syngas the electrochemical performance of the cell was lower than the counterpart seen with hydrogen.

In summary, the importance of the longitudinal current and temperature variations and the regarding characterization methods in terms of the performance and structure degradations has been disclosed. The processes involving in the temperature variations and their respective contributions have been revealed. The relationship among the current and temperature variations has been elucidated. The reliability of numerical tools for the spatial characterization of SOFCs has been analyzed; for improving the reliability of numerical tools, the spatial temperature variations has been proposed as an advanced validation method. It is concluded that accurate computation of the longitudinal current and concentration variations by numerical tools strongly depends on rigorous consideration of the mass and heat transfer processes along the cell. Furthermore, the endothermic cooling and the corresponding rate of the reforming reaction have been in-situ analyzed along a mt-SOFCs utilizing syngas to improve the reliability of numerical tools employed for internal reforming SOFCs .

7.2 Outlook

For improving the reliability of the numerical tools to characterize spatially varying properties (concentration, current, and temperature) in SOFCs regardless of the form, in this study, the segmentation method was applied on mt-SOFCs along with a two-dimensional finite element model. Through diverse experimental and numerical investigations, the longitudinal current and temperature variations were elaborated. All the processes involving in the temperature variations including the current variations have been disclosed and their respective contributions were analyzed. With the numerical method, the reliability of numerical tools has been evaluated. However, the precision of the numerical computation has been seen to be insufficient due presumably to the simplified heat and mass transport processes. Improvement of the heat and mass transport processes in the numerical model would hence enhance the precision of the numerical computation.

Spatial variations in the characteristic properties of SOFCs are more crucial while direct internal reforming of hydrocarbons. This is due to the fact that the rate the reforming reaction also varies spatially with respect to the concentrations of the species present in the fuel stream. In relation with the rate of the reforming reaction, particular issues, e.g., endothermic cooling, carbon deposition, etc. occur, resulting in the structure degradations. The spatial characterization is hence more demanded in the direct internal reforming SOFCs. In this regard, the numerical tools are expected to play a substantial role. Apart from the hydrogen-utilizing SOFCs, the rate of the heat absorption by the reforming reaction is required to be incorporated for accurately estimating the spatial variations. The endothermic cooling and the associated spatial variation in the rate of the reforming reaction was indeed in-situ analyzed in this study. Although this study has revealed the extent of the endothermic cooling due to the internal reforming, it is found that the spatial variation in the rate of the reforming reaction could only be elucidated by a more fundamental study. Diagnosis of the spatial variation in the rate of the reforming reaction would allow for shedding light on the issues related to the rate of the reforming reaction.

References

[1] A. Selimovic, M. Kemm, T. Torisson, and M. Assadi, "Steady state and transient stress analysis in planar solid oxide fuel cells," *J. Power Sources*, vol. 145, pp. 463–469, 2005.

[2] S. Campanari and P. Iora, "Definition and sensitivity analysis of a finite volume SOFC model for a tubular geometry," *J. Power Sources*, vol. 132, pp. 113–126, 2004.

[3] K. Fischer and J. Seume, "Location and magnitude of heat sources in solid oxide fuel cells," *J. Fuel Cell Sci. Technol.*, vol. 6, no. 011002, pp. 1–11, 2009.

[4] S. Singhal, "Solid oxide fuel cells," *The Electrochemical Society Interface*, vol. Winter, pp. 41–44, 2007.

[5] T. Klemensoe, C. Chung, and M. Larsen, P.H. amd Mogensen, "The mechanism behind redox instability of anodes in high-temperature SOFCs," *J. Electrochem. Soc.*, vol. 152, pp. 2186–2192, 1995.

[6] S. Singhal, "Solid oxide fuel cells for statinoary, mobile, and military applications," *Solid State Ionics*, vol. 152-153, pp. 405–410, 2002.

[7] "Fuel cell reaction kinetics," in *Fuel Cell Fudamentals* (R. O'Hayre, S.-W. Cha, W. Colella, and F. Prinz, eds.), Wiley, 2009.

[8] A. Virkar, J. Chen, C. Tanner, and J.-W. Kim, "The role of electrode microstructure on acivation and concentration polarizatons in solid oxide fuel cells," *Solid State Ionics*, vol. 131, pp. 189–198, 2000.

[9] N. Nakagawa, H. Sakurai, K. Kondo, T. Morimoto, K. Hatanaka, and K. Kato, "Evaluation of the effective reaction zone at Ni(NiO)/Zirconia anode by using an electrode with a novel structure," *J. Electrochem. Soc.*, vol. 142, no. 10, pp. 3474–3479, 1995.

[10] M. Ni, M. Leung, and D. Leung, "Mathematical modelling of proton-conducting solid oxide fuel cells and comparison with oxygen-ion-conducting counterpart," *Fuel Cells*, vol. 07, no. 4, pp. 269–278, 2007.

[11] K. Howe, G. Thompson, and K. Kendall, "Micro-tubular solid oxide fuel cells and stacks," *J. Power Sources*, vol. 196, pp. 1677–1686, 2011.

[12] Y. Patcharavorachot, A. Arpornwichanop, and A. Chuachuensuk, "Electrochemical study of planar solid oxide fuel cell: role of support structures," *J. Power Sources*, vol. 177, pp. 254–261, 2008.

[13] O. Yamamoto, "Solid oxide fuel cells: Fundamental aspects and prospects," *Electochim. Acta*, vol. 45, pp. 2423–2435, 2000.

[14] K. Kendall, "Progress in microtubular solid oxide fuel cells," *Int. J. Appl. Ceram. Technol.*, vol. 7, no. 1, pp. 1–9, 2010.

[15] D.-W. Kim, U.-J. Yun, J.-W. Lee, T.-H. Lim, S.-B. Lee, S.-J. Park, R.-H. Song, and G. Kim, "Fabrication and operating characteristics of a flat tubular segmented-in-series solid oxide fuel cell unit bundle," *Energy*, vol. 72, pp. 215–221, 2014.

[16] F. Nagel, T. Schildhauer, S. Biollaz, and A. Wokaun, "Performance comparison of planar, tubular and delta8 solid oxide fuel cells using a generalized finite volume model," *J. Power Sources*, vol. 184, pp. 143–164, 2008.

[17] M. Suzuki, N. Shikazono, K. Fukagata, and N. Kasagi, "Numerical analysis of coupled transport and reaction phenomena in an anode-supported flat-tube solid oxide fuel cell," *J. Power Sources*, vol. 180, pp. 29–40, 2008.

[18] S. Singhal, "Advances in solid oxide fuel cell technology," *Solid State Ionics*, vol. 135, pp. 305–313, 2000.

[19] S. Kotake, H. Nakajima, and T. Kitahara, "Mass transfer in an anode-supported honeycomb solid oxide fuel cell," *ECS Trans.*, vol. 64, no. 45, pp. 135–142, 2015.

[20] H. Zhong, H. Toriyama, and T. Ishihara, "Honeycomb-type solid oxide fuel cell using La0.9Sr0.1Ga0.8Mg0.2O3 electrolye for high volumetric power density," *J. Electrochem. Soc.*, vol. 156, no. 1, pp. B74–B79, 2009.

[21] J. Ding and J. Liu, "A novel design and performance of cone-shaped tubular anode-supported segmented-in-series solid oxide fuel cell stack," *J. Power Sources*, vol. 193, pp. 769–773, 2009.

[22] Y. Liu, Y. Tang, J. Ding, and J. Liu, "Electrochemical performance of cone-shaped anode-supported segmented-in-series sofcs fabricated by gel-casting technique," *Int. J. Hydrogen Energy*, vol. 37, pp. 921–925, 2012.

[23] Y. Bai, J. Liu, and C. Wang, "Performance of cone-shaped tubular anode-supported segmented-in-series solid oxide fuel cell stack fabricated by dip coating technique," *Int. J. Hydrogen Energy*, vol. 34, pp. 7311–7315, 2009.

[24] T. Suzuki, T. Yamaguchi, M. H. Zahir, Y. Fujishiro, M. Awano, and Y. Funahashi, "Development of high performance micro tubular SOFCs and modules," *Eleventh Grove Fuel Cell Symposium*, London, UK, September 22-24, 2009.

[25] P. Aguiar, C. Adjiman, and N. Brandon, "Anode-supported intermediate temperature direct internal reforming solid oxide fuel cell. i: model-based steady-state performance," *J. Power Sources*, vol. 138, pp. 120–136, 2004.

[26] J.-W. Kim, A. Virkar, K.-Z. Fung, K. Mehta, and S. Singhal, "Polarization effects in intermediate temperature, anode-supported solid oxide fuel cells," *J. Electrochem. Soc.*, vol. 146, no. 1, pp. 69–78, 1999.

[27] S. Chan, K. Khor, and Z. Xia, "A complete polarization model of a solid oxide fuel cell and its sensitivity to the change of cell component thickness," *J. Power Sources*, vol. 93, pp. 130–140, 2001.

[28] K. Hemmes, "Fuel cells," in *Modern Aspects of Electrochemistry* (R. E. White, B. E. Conway, C. G. Vayenas, and M. E. Gamboa-Adelco, eds.), vol. 37, New York: Kluwer Academic Publishers, 2004.

[29] H. Morita, M. Komoda, Y. Mugikura, Y. Izaki, T. Watanabe, Y. Masuda, and T. Matsuyama, "Performance analysis of molten carbonate fuel cell using a Li/Na electrolyte," *J. Power Sources*, vol. 112, pp. 509–518, 2002.

[30] M. Keane, M. K. Mahapatra, A. Verma, and P. Singh, "LSM-YSZ interactions and anode delamination in solid oxide electrolylsis cells," *Int. J. Hydrogen Energy*, vol. 37, p. 16776, 2012.

[31] E. Achenbach and E. Riensche, "Methane/steam reforming kinetics for solid oxide fuel cells," *J. Power Sources*, vol. 52, pp. 283–288, 1994.

[32] K. Fischer and J. Seume, "Impact of the temperature profile on thermal stress in a tubular solid oxide fuel cell," *J. Fuel Cell Sci. Technol.*, vol. 6, no. 011017, pp. 1–9, 2009.

[33] O. Razbani, I. Waernhaus, and M. Assadi, "Experimental investigation of temperature distribution over a planar solid oxide fuel cell," *Applied Energy*, vol. 105, pp. 155–160, 2013.

[34] M. Hanasaki, C. Uryu, T. Daio, T. Kawabata, Y. Tachikawa, S. Lyth, Y. Shiratori, S. Taniguchi, and K. Sasaki, "SOFC durability against standby and shutdown cycling," *J. Electrochem. Soc.*, vol. 161, no. 9, pp. F850–F860, 2014.

[35] H. Yakabe, T. Ogiwara, M. Hishinuma, and I. Yasuda, "3-D model calculation for planar SOFC," *J. Power Sources*, vol. 102, pp. 144–154, 2001.

[36] C.-K. Lin, T.-T. Chen, Y.-P. Chyou, and L.-K. Chiang, "Thermal stress analysis of a planar SOFC stack," *J. Power Sources*, vol. 164, pp. 238–251, 2007.

[37] A. Nakajo, C. Stiller, G. Härkegård, and O. Bolland, "Modelling of thermal stresses and probability of survival of tubular SOFC," *J. Power Sources*, vol. 158, pp. 287–294, 2006.

[38] L.-K. Chiang, H.-C. Liu, Y.-H. Shiu, C.-H. Lee, and R.-Y. Lee, "Thermo-electrochemical and thermal stress analysis for an anode-supported SOFC cell," *Renewable Energy*, vol. 33, pp. 2580–2588, 2008.

[39] A. Faes, A. Hessler-Wyser, A. Zryd, and J. Van Herle, "A review of redox cycling of solid oxide fuel cells anode," *Membranes*, vol. 2, pp. 585–664, 2012.

[40] M. Cassidy, G. Lindsay, and K. Kendall, "The reduction of nickel-zirconia cermet anodes and the effects on supported thin electrolytes," *J. Power Sources*, vol. 61, pp. 189–192, 1996.

[41] D. Mogensen, J. Grunwaldt, P. Hendriksen, K. Dam-Johansen, and J. Nielsen, "Internal steam reforming in solid oxide fuel cells: status and opportunities of kinetic studies and their impact on modeling," *J. Power Sources*, vol. 196, pp. 25–38, 2001.

[42] S. Freunberger, M. Reum, A. Wokaun, and F. Büchi, "Expanding current distribution measurement in PEFCs to sub-milimeter resolution," *Electrochem. Commun.*, vol. 8, pp. 1435–1438, 2006.

[43] A. Hakenjos, H. Muenter, U. Wittstadt, and C. Hebling, "A PEM fuel cell for combined measurement of current and temperature distribution, and flow field flooding," *J. Power Sources*, vol. 131, pp. 213–216, 2004.

[44] D. Brett, S. Atkins, N. Brandon, V. Vesovic, N. Vasileiadis, and A. Kucernak, "Measurement of the current distribution along a single flow channel of a solid polymer fuel cell," *Electrochem. Commun.*, vol. 3, pp. 628–632, 2001.

[45] M. Noponen, T. Mennola, M. Mikkola, T. Hottinen, and P. Lund, "Measurement of current distribution in a free-breathing PEMFC," *J. Power Sources*, vol. 106, pp. 304–312, 2002.

[46] N. Rajalakshmi, M. Raja, and K. Dhathathreyan, "Evaluation of current distribution in a proton exchange membrane fuel cell by segmented cell approach," *J. Power Sources*, vol. 112, pp. 331–336, 2002.

[47] H. Sun, G. Zhang, L.-J. Guo, and H. Liu, "A novel technique for measuring current distributions in PEM fuel cells," *J. Power Sources*, vol. 158, pp. 326–332, 2006.

[48] J. Stumper, S. Campbell, D. Wilkinson, M. Johnson, and M. Davis, "In-situ methods for the determination of current distributions in PEM fuel cells," *Electrochim. Acta*, vol. 43, no. 24, pp. 3773–3783, 1998.

[49] U. Shrivastava and K. Tajiri, "In-plane distribution analysis in the land-channel direction of a proton exchange membrane fuel cell (PEMFC)," *J. Electrochem. Soc.*, vol. 162, no. 7, pp. F722–F727, 2015.

[50] P. Metzger, K.-A. Friedrich, H. Müller-Steinhagen, and G. Schiller, "SOFC characteristics along the flow path," *Solid State Ionics*, vol. 177, pp. 2045–2051, 2006.

[51] P. Metzger, K.-A. Friedrich, G. Schiller, and C. Willich, "Spatially resolved measuring technique for solid oxide fuel cells," *J. Fuel Cell Sci. and Technol.*, vol. 6, pp. 021304–(1–4), 2009.

[52] A. Shimizu, H. Nakajima, and T. Kitahara, "Current distribution measurement of a microtubular solid oxide fuel cell," *ECS Trans.*, vol. 57, no. 1, pp. 727–732, 2013.

[53] J. Saunders and M. Davy, "In-situ studies of gas phase composition and anode surface temperature through a model DIR-SOFC steam-methane reformer at 973.15 K," *Int. J. Hydrogen Energy*, vol. 38, pp. 13762–13773, 2013.

[54] J. Robinson, L. Brown, R. Jervis, O. Taiwo, T. Heenan, J. Millichamp, T. Mason, T. Neville, R. Clague, D. Eastwood, C. Reinhard, P. Lee, D. Brett, and P. Shearing, "Investigating the effect of thermal gradients on stress in solid oxide fuel cell anodes using combined synchrotron radiation and thermal imaging," *J. Power Sources*, vol. 288, pp. 473–481, 2015.

[55] Y. Shiratori, T. Ogura, H. Nakajima, M. Sakamoto, Y. Takahashi, Y. Wakita, T. Kitaoka, and K. Sasaki, "Study on paper-structured catalyst for direct internal reforming SOFC fueled by the mixture of CH4 and CO2," *Int. J. Hydrogen Energy*, vol. 38, pp. 10542–10551, 2013.

[56] http://www.maximintegrated.com/en/app-notes/index.mvp/id/5032, Last accessed in August, 2015.

[57] http://www.omega.com/temperature/z/pdf/z019-020.pdf, Last accessed in August, 2015.

[58] H. Nakajima, "Electrochemical impedance spectroscopy study of mass transfer in an anode-supported microtubular solid oxide fuel cell," in *Mass Transfer-Advanced Aspects* (H. Nakajima, ed.), InTech, 2011.

[59] P. Costamagna and K. Honegger, "Modeling of solid oxide heat exchanger integrated stacks and simulation at high fuel utilization," *J. Electrochem. Soc.*, vol. 145, pp. 3995–4007, 1998.

[60] S. Campanari and P. Iora, "Definition and sensitivity analysis of a finite volume SOFC model for a tubular cell geometry," *J. Power Sources*, vol. 132, pp. 113–126, 2004.

[61] T. Nishino, H. Iwai, and K. Suzuki, "Comprehensive numerical modeling and analysis of a cell-based indirect-internal reforming tubular SOFC," *J. Fuel Cell Sci. and Technol.*, vol. 3, pp. 33–44, 2006.

[62] M. Andersson, H. Paradis, J. Yuan, and B. Sundén, "Three dimensional modeling of an solid oxide fuel cell coupling charge transfer phenomena with transport processes and heat generation," *Electrochim. Acta*, vol. 109, pp. 881–893, 2013.

[63] K. Kanamura, S. Yoshioka, and Z. Takehara, "Temperature distribution in tubular solid oxide fuel cell," *Chem. Soc. Jpn.*, vol. 64, pp. 1828–1834, 1991.

[64] M. Lockett, M. Simmons, and K. Kendall, "CFD to predict temperature profile for scale up micro-tubular SOFC stacks," *J. Power Sources*, vol. 131, pp. 243–246, 2004.

[65] H. Nakajima, T. Konomi, and T. Kitahara, "Thermal analysis of a microtubular solid oxide fuel cell using electrochemical impedance spectroscopy," *ECS Trans.*, vol. 25, no. 2, pp. 359–368, 2009.

[66] B. Morel, R. Roberge, S. Savoie, T. Napporn, and M. Meunier, "An experimental evaluation of the temperature gradient in solid oxide fuel cells," *Electrochem. Solid-State Lett.*, vol. 10, no. 2, pp. B31–B33, 2007.

[67] A. Kulikovsky, "Temperature and current distribution along the air channel in planar SOFC stack: model and asymptotic solution," *J. Fuel Cell Sci. Technol.*, vol. 7, no. 011015, pp. 1–6, 2010.

[68] Ö. Aydın, H. Nakajima, and T. Kitahara, "In-situ diagnosis and assessment of longitudinal current variation by electrode-segmentation method in anode-supported microtubular solid oxide fuel cells," *J. Power Sources*, vol. 279, pp. 218–223, 2015.

[69] Ö. Aydın, H. Nakajima, and T. Kitahara, "Current and temperature distributions in-situ acquired by electrode-segmentation along a microtubular solid oxide fuel cell operating with syngas," *J. Power Sources*, vol. 293, pp. 1053–1061, 2015.

[70] Ö. Aydın, H. Nakajima, and T. Kitahara, "Influence of convective heat transfer by air flow on local current/temperatures along microtubular solid oxide fuel cells in-situ identified by electrode-segmentation method for co- and counter-flow configurations," *ECS Trans.*, no. 1, p. 2141, 2015.

[71] M. Andersson, J. Yuan, and B. Sundén, "SOFC modelling considering electrochemical reactions at the active three phase boundaries," *J. Heat Mass Transfer*, vol. 55, pp. 773–788, 2012.

[72] K. Recknagle, R. Williford, L. Chick, D. Rector, and M. Khaleel, "Three-dimensional thermo-fluid electrochemical modelling of planar SOFC stacks," *J. Power Sources*, vol. 113, pp. 109–114, 2003.

[73] M. Santarelli, P. Leone, M. Cali, and G. Orsello, "Experimental analysis of the voltage and temperature behaviour of a solid oxide fuel cell generator," *J. Fuel Cell Sci. Technol.*, vol. 4, pp. 143–153, 2007.

[74] Y. Cengel, "Internal forced convection," in *Heat Transfer, A Practical Approach* (Y. Cengel, ed.), p. 424, McGraw-Hill, 2 ed., 2002.

[75] V. Janardhanan and O. Deutschman, "Numerical study of mass and heat transport in solid oxide fuel cells runing on humidified methane," *Chem. Eng. Sci.*, vol. 62, pp. 5473–5486, 2007.

[76] W. M. Kays and H. C. Perkins in *Handbook of Heat Transfer* (W. M. Rohsenow, J. P. Hartnett, and E. N. Ganić, eds.), McGraw-Hill, 1985.

[77] S. Jensen, A. Hauch, P. Hendriksen, M. Mogensen, N. Bonanos, and T. Jacobsen, "A method to separate process contributions in impedance spectra by variation of test conditions," *J. Electrochem. Soc.*, vol. 154, no. 12, pp. B1325–B1330, 2007.

[78] Y.-P. Chyou, T.-D. Chung, J.-S. Chen, and R.-F. Shie, "Integrated themal engineering analyses with heat transfer at periphery o f planar solid oxide fuel cell," *J. Power Sources*, vol. 139, pp. 126–140, 2005.

[79] Y. Wang, F. Yoshiba, T. Watanabe, and S. Weng, "Numerical analysis of electrochemical characteristics and heat/species transport for planar porous-electrode-supported SOFC," *J. Power Sources*, vol. 170, pp. 101–110, 2007.

[80] Y. Lu, L. Schaefer, and P. Li, "Numerical study of a at-tube high power density solid oxide fuel cell Part i. Heat/mass transfer and uid ow," *J. Power Sources*, vol. 140, pp. 331–339, 2005.

[81] S. Bedogni, S. Campanari, P. Iora, L. Montelatici, and P. Silva, "Experimental analysis and modeling for a circular planar type IT-SOFC," *J. Power Sources*, vol. 171, pp. 617–625, 2007.

[82] R. Bove and S. Ubertini, "Modeling solid oxide fuel cell operation: Approaches, techniques and results," *J. Electrochem. Soc.*, vol. 159, pp. 543–559, 2006.

[83] P. Costamagna and K. Honegger, "Modeling of solid oxide heat exchanger integrated stacks and simulation at high fuel utilization," *J. Electrochem. Soc.*, vol. 145, pp. 3995–4007, 1998.

[84] C. Boigues-Muñoz, G. Santori, S. McPhail, and F. Polonara, "Thermochemical model and experimental validation of a tubular sofc cell comprised in a 1kWel stack designed for μCHP applications," *Int. J. Hydrogen Energy*, vol. 39, pp. 21714–21723, 2014.

[85] S. Kakac, A. Pramuanjaroenkij, and X. Zhou, "A review of numerical modeling of solid oxide fuel cells," *Int. J. Hydrogen Energy*, vol. 32, pp. 761–786, 2007.

[86] L. Andreassi, G. Rubeo, S. Ubertini, P. Lunghi, and R. Bove, "Experimental and numerical analysis of a radial flow solid oxide fuel cell," *Int. J. Hydrogen Energy*, vol. 32, pp. 4559–4574, 2007.

[87] Z. Qu, P. Aravind, S. Boksteen, N. Dekker, A. Janssen, N. Woudstra, and A. Verkooijen, "Three-dimensional computational fluid dynamics modeling of anode-supported planar SOFC," *Int. J. Hydrogen Energy*, vol. 36, pp. 10209–10220, 2011.

[88] M. Nerat and D. Juričić, "A comprehensive 3-D modeling of a single planar solid oxide fuel cell," *Int. J. Hydrogen Energy*, vol. 41, pp. 3613–3627, 2016.

[89] G. Wang, Y. Yang, H. Zhang, and W. Xia, "3-D model of thermo-uid and electrochemical for planar SOFC," *J. Power Sources*, vol. 167, pp. 398–405, 2007.

[90] T. Ho, P. Kosinski, A. C. Hoffmann, and A. Vik, "Numerical analysis of a planar anode-supported SOFC with composite electrodes," *Int. J. Hydrogen Energy*, vol. 34, pp. 3488–3499, 2009.

[91] M. Iwata, T. Hikosaka, M. Morita, K. Iwanari, T. Ito, K. Onda, Y. Esaki, Y. Sasaki, and S. Nagata, "Performance analysis of planar-type unit SOFC considering current and temperature distributions," *Solid State Ionics*, vol. 132, pp. 297–308, 2000.

[92] M. Andersson, J. Yuan, and B. Sundén, "SOFC modeling considering hydrogen and carbon monoxide as electrochemical reactants," *J. Power Sources*, vol. 232, pp. 42–54, 2013.

[93] O. Razbani, M. Assadi, and M. Andersson, "Three dimensional CFD modeling and experimental validation of an electrolyte supported solid oxide fuel cell fed with methane-free biogas," *Int. J. Hydrogen Energy*, vol. 38, pp. 10068–10080, 2013.

[94] M. Serincan, U. Pasaogullari, and N. Sammes, "Computational thermal-fluid analysis of a microtubular solid oxide fuel cell," *J. Electrochem. Soc.*, vol. 155, no. 11, pp. B1117–B1127, 2008.

[95] M. Suzuki, N. Shikazono, K. Fukagata, and N. Kasagi, "Numerical analysis of coupled transport and reaction phenomena in an anode-supported flat-tube solid oxide fuel cell," *J. Power Sources*, vol. 180, pp. 29–40, 2008.

[96] D. Larrain, J. Van herle, F. Maréchal, and D. Favrat, "Generalized model of planar SOFC repeat element for design optimization," *J. Power Sources*, vol. 131, pp. 304–312, 2004.

[97] P.-W. Li and K. Suzuki, "Numerical modeling and performance study of a tubular SOFC," *J. Electrochem. Soc.*, vol. 151, no. 4, pp. A548–A557, 2004.

[98] C. Haynes and W. Wepfer, "Characterizing heat transfer within a commercial-grade tubular solid oxide fuel cell for enhanced thermal management," *Int. J. Hydrogen Energy*, vol. 26, pp. 369–379, 2001.

[99] E. N. Fuller, P. D. Schettler, and J. C. Giddings, "A new method for prediction of binary gas-phase diffusion coefficients," *Ind. Eng. Chem.*, vol. 58, pp. 18–27, 1966.

[100] M. Mench, "Transport in fuel cell systems," in *Fuel Cell Engines* (M. Mench, ed.), Hoboken, New Jersey: John Wiley and Sons, Inc., 2008.

[101] D. Simwonis, H. Thülen, F. J. Dias, A. Naoumidis, and D. Stöver, "Properties of Ni/YSZ porous cermets for SOFC anode substrates prepared by tape casting and coat-mix process," *J. Mater. Process. Technol.*, vol. 92-93, pp. 107–111, 1999.

[102] http://www.design1st.com/Design-Resource-Library/engineering_data/ThermalEmissivityValues.pdf, Last accessed in March, 2016.

[103] Ö. Aydın, H. Nakajima, and T. Kitahara, "Processes involving in the temperature variations in solid oxid fuel cells in-situ analyzed through electrode-segmentation method," *J. Electrochem. Soc.*, vol. 163, pp. F216–F224, 2016.

[104] M. Andersson, J. Yuan, B. Sundén, and W.-G. Wang, "LTNE approach and simulation for anode-supported SOFCs," *Proceedings of FuelCell2009*, pp. 539–549, doi:10.1115/FuelCell2009–85054, June 8-10, 2009.

[105] A. L. Dicks, K. Pointon, and A. Siddle, "Intrinsic reaction kinetics of methane steam reforming on a nickel/zirconia anode," *J. Power Sources*, vol. 86, pp. 523–530, 2000.

[106] C. Finnerty and R. Ormerod, "Internal reforming over nickel/zirconia anodes in SOFCs operating on methane: influence of anode formulation, pre-treatment and operating conditions," *J. Power Sources*, vol. 86, pp. 390–394, 2000.

[107] W. Lehnert, J. Meusinger, and F. Thom, "Modeling of gas transport phenomena in SOFC anodes," *J. Power Sources*, vol. 87, pp. 57–63, 2000.

[108] P. Vernoux, J. Guindet, and M. Kleitz, "Gradual internal methane reforming in intermediate-temperature solid oxide fuel cells," *J. Electrochem. Soc.*, vol. 145, pp. 3487–3492, 1998.

[109] E. Hecht, G. Gupta, H. Zhu, A. Dean, R. Kee, L. Maier, and O. Deutschmann, "Methane reforming kinetics within a Ni/YSZ SOFC andoe support," *Appl. Catal., A: Gen.*, vol. 295, pp. 40–51, 2005.

[110] K. Ahmed and K. Foger, "Kinetics of internal steam reforming of methane on Ni/YSZ based anodes for solid oxide fuel cells," *Catal. Today*, vol. 63, pp. 479–487, 2000.

[111] R. Peters, R. Dahl, U. Klüttgen, C. Palm, and D. Stolten, "Internal reforming of methane in solid oxide fuel cell systems," *J. Power Sources*, vol. 106, pp. 238–244, 2002.

[112] J. Meusinger, E. Riensche, and U. Stimming, "Reforming of natural gas in solid oxide fuel cell systems," *J. Power Sources*, vol. 71, pp. 315–320, 1998.

[113] H. Timmerman, D. Fouquet, A. Weber, E. Ivers-Tiffée, U. Hennings, and R. Reimert, "Internal reforming of methane at Ni/YSZ and Ni/CGO SOFC cermet," *Fuel Cells*, vol. 06, no. 3-4, pp. 307–313, 2006.

[114] S. Gordan and B. McBride, "Chemical equilibrium with applications." http://www.grc.nasa.gov/www/CEAWeb/.

[115] W. Bessler, J. Warnatz, and D. Goodwin, "The influence of equilibrium potential on the hydrogen oxidation kinetics of SOFC anodes," *Solid State Ionics*, vol. 177, pp. 3371–3383, 2007.

[116] H. Nakajima, T. Kitahara, and T. Konomi, "Electrochemical impedance spectroscopy analysis of an anode-supported microtubular solid oxide fuel cell," *J. Electrochem. Soc.*, vol. 157, no. 11, pp. B1686–B1692, 2010.